Development and Validation of a Pelvis Finite Element Model for Side Panel Intrusion Threats

---

A Thesis
Presented to
the faculty of the School of Engineering and Applied Science
University of Virginia

In partial fulfillment
of the requirements for the degree

Masters of Science

by

Ryan J. Neice

August 2019

ABSTRACT

Loading conditions resulting from the detonation of improvised explosive devices (IEDs) have posed a serious risk to the warfighter in modern military conflicts. Vehicle bourn IEDs result in high-rate lateral loading to the vehicle structure that can cause side panel intrusion into occupant compartment, and potentially into the body of a mounted warfighter inside. These impacts can cause severe injury throughout the body, including the pelvis. Combat-related pelvis fractures are linked to increased mortality rates and amputation risk. Biomechanical research is needed to improve the design of vehicles and protective equipment to mitigate injuries to the pelvis.

Finite element (FE) models are useful tools in evaluating the biomechanics of impact and injury. FE models can provide quick analyses over a range of loading scenarios, and can be used directly in the countermeasure design process. With this in mind, an injury-predictive FE model of the human pelvis was developed using modeling methods appropriate for evaluating the high-rate injurious loading characteristics found in military combat. The response and injury predictions of this pelvis model were assessed against experimental lateral impact testing performed on human cadaveric pelvises. Signal correlation analysis was applied to objectively rate the validity the FE pelvis force responses. Injuries predicted by the pelvis model, when using maximum principal strain failure criteria, were consistent with those occurring in the experiments.

The pelvis model was then used to perform an injury threshold analysis where impactor mass and velocity was varied. This study identified the anterior pelvis as being more vulnerable to lateral impact. Recent research has highlighted a lack of consensus on a consistent injury predictive metric for the pelvis in lateral impact. Injury risk functions were constructed based on anterior and posterior pelvis force, and the posterior force of the pelvis was identified as a more consistent injury predictive metric than anterior force. This finding has potential implications for dummy design.

Finally, the model developed in this study was part of a larger development project to create a whole human body FE model for analyses of human body exposure to military-relevant impact events. The addition of the developed and validated pelvis model will aid future vehicle development for improved safety features. Side panel safety design efforts should focus on mitigating acetabular loading in the event of a lateral impact scenario, and dummy instrumentation should include load cells located in the posterior pelvis for measuring pelvis injury risk.

TABLE OF CONTENTS

LIST OF FIGURES

LIST OF TABLES

CHAPTER 1: INTRODUCTION

1.1. Statement of Problem

Improvised explosive devices (IEDs) have been a significant threat to the United States warfighter in contemporary military operations. IEDs were responsible for around half of all U.S. military casualties in the Iraq War (Wilson 2007), and in general, blast was the cause of 75% of all US combat casualties in Operation Iraqi Freedom and Operation Enduring Freedom (FY14 Report STEP). The mortality of soldiers subjected to IEDs and other blasts was reduced when the military made improvements in combat medical services such as the “Golden Hour Policy”, where helicopter transport of injured combat casualties was mandated to take 60 minutes or less. (Kotwal et al. 2016**)**. More protective vehicles, such as the Mine Resistant Ambush Protected (MRAP), and improved personal protective equipment increased warfighter survivability, but also elevated the number of combat injuries because soldiers were surviving (Russell 2009). The unpredictable nature of combat theatres causes situations where non-fatal injuries such as bone fracture can quickly turn into a life threatening event, particularly when the effectiveness and mobility of the warfighter is hindered. In addition, after an average of 33 months of recovery time from a blast injury, over two-thirds of personnel had ongoing treatment for injured limbs and only 14% of those injured were able to return to preinjury occupations (Ramasamy 2013). Recent studies have suggested that an increase in soldiers’ risk of suicide and mental stress is associated with higher frequencies of IED attacks (Ursano et at. 2017), and it is hypothesized that perceived preparedness for such attacks improves psychological vigor such as combat readiness. The IED threat has grown in the information age because the instructions of how to manufacture such explosives are widely available online and materials to build these explosives are easily accessible.

Under body blast (UBB) events, when an IED detonates underneath a vehicle, causes short duration, high-rate upward loading of the vehicle floor and seating (Figure 1). This vertical accelerative load will potentially result in significant trauma or death to the warfighter occupant. The load path for an UBB event is through the occupant's points of contact with the vehicle, which are the lower extremity and pelvic regions, making them especially vulnerable to injury.

Lateral intrusion can cause significant injury to the human pelvis which has been observed in side impact automotive collisions (Guillemot et al. 1998). In more recent conflicts, vehicle borne improvised explosive devices (VBIEDs) have become a commonly used weapon by insurgency groups, such as ISIS, against military vehicles (Kaaman 2019**)**. The load path of a VBIED differs from an UBB event in that the blast begins at a higher vertical orientation, more in line with the carriage of the military vehicle (Figure 1). The lateral blast loading (LBL) from a VBIED leads to flank loading of the carriage; which during the tertiary blast phase can cause side panel intrusion into the seated warfighter.

Figure 1: (Left) Traditional under body blast (UBB) event, where an IED exploded beneath a military vehicle. (Right) A failed VBIED suicide attack, where the vehicle did not detonate. The load path varies significantly based on where the blast is originating from

Fracture of the pelvis is consequential to warfighter well-being. A 2008 mortality study showed 26% of service members who died in the Iraq war had sustained a pelvic fracture (Davis et al. 2012). Injury descriptions of these pelvic fractures were classified as follows: 5.5% lateral compression, 12.1% vertical shear, 25.3% combined mechanism, and 35.1% as unable to classify or penetrating (Bailey et al. 2011). Pelvis injury has also been associated with amputation risk. Cross et al. (2014) found pelvic ring fractures were associated with 22% of lower limb amputations due to IED blast (n=77). Additionally, a link between amputation severity was observed; the likelihood of a pelvis fracture with bilateral above the knee amputation was 4x more likely than with a unilateral lower limb amputation. The preceding information emphasizes the consequence of pelvic ring fracture and the variability of injury mechanism in military combat zones.

1.2. Motivation

Scientific understanding of human biomechanics in blast related events can lead to improvements in warfighter safety. Tools are needed to evaluate human response to military loading scenarios. The Warrior Injury Assessment Manikin (WIAMan) program has created an Anthropomorphic Test Dummy (ATD) that was developed specifically for conditions expected in a combat theater (Hughes and Landers 2017). Although ATDs are sophisticated tools in predicting skeletal injuries, they are expensive to produce and are unable to observe soft tissue responses. Post Mortem Human Surrogates (PMHS) are another experimental option in studying biomechanics, but they have limitations as well. Along with ethical controversies surrounding PMHS experimentations, this type of research can produce a wide spectrum of data across different specimen due to biological variances such as age, gender, bone structure, and body mass. PMHS testing requires specialized protocols for safe and ethical handling and preparation, is expensive, and is not repeatable in the same sense that an ATD is. Given the limitations in experimental testing, there is a need for an updated tool to evaluate injurious biomechanics related to military impact conditions that would have value in enabling improved design. Numerical methods and computational models are such tools that alleviate many of the limitations that exist with experimental testing, and are usually cheaper and more adaptable to evolving mission needs more quickly, while still preserving accuracy. Computational models could provide advancements in warfighter safety and additional insight into experimental test methods.

1.2.1. Human body finite element model for military loading

Finite element (FE) modeling is a computational tool that has had substantial success in the automotive safety industry for predicting occupant response during a vehicle crash. Currently, there exists a need for FE models specifically geared for military related evaluations to serve as a beneficial low-cost tool in the identification of injury mechanisms, thresholds, and analysis of mitigation efforts. When used in conjunction with experimental ATD tests, a human body FE model can provide additional biomechanical insights, such as soft tissue behavior, parametric analyses results, and quick evaluations of injury alleviation methods. Such models can predict human outcomes over a range of potential loading environments, providing recommendations for future experimental testing or safety design. This category of human body FE models can measure specific stresses, strains, and kinematics of individually modeled tissues that otherwise are immeasurable in an ATD or PMHS experiment. Computational models boast the ability to perform analysis on parameter sensitivities and evaluate their consequence to the overall biological system. Computational analyses have also contributed to the development of effective constitutive models of biological tissues.

As previously mentioned, many of the existing human body FE models have been developed and validated for use in analyses of automotive impacts (Zhao and Narwani 2005, Shin et al. 2012, Fressmann et al. 2007, Panzer et al. 2011, Chen et al. 2018, Nie et al. 2017). There is a need for a validated high-fidelity human body FE model that can predict injuries in extreme loading conditions like those conditions experienced in blast events. Such a model could be used to evaluate the energy and injury mitigation effectiveness of military boots, floor mats, and vehicles. The modeling approach required to capture the response of a specific military loading scenario is one that includes high-quality meshing, properly-suited material properties, and high-rate loading validations.

1.2.2. Reliable injury predictive metric for lateral loading

Understanding the injury tolerances of the human body, which links a loading scenario to likelihood of injury, is important in the design and evaluation of protective systems. Injury risk functions (IRFs) are a commonly used method that links a quantitative metric associated with the loading to a probability of the recipient getting an injury. In the development of IRFs, it is essential to identify dependable metrics to correctly define the mechanisms and corresponding severities of injuries. Recent efforts to define an IRF for the human pelvis subjected to lateral impact have been performed (Leport et al. 2007, Petitjean et al. 2012, Petit et al. 2015, Petital et al. 2018), with disagreements among authors regarding whether anterior pelvis force or posterior pelvis force was a better metric to predict injury. A high fidelity human body FE model could give further insight into what injury predictive metric is reliable to predict injury. This in turn could provide evidence to support an injury metric and lead to its adoption for use in future military and automotive safety related applications. Understanding lateral loading and the correlation to injury is useful to instrumentation guidance of ATDs. Furthermore, identifying thresholds based on input conditions can highlight the areas of the body most prone to injury.

1.3. Scope

The goal of this thesis is to develop an injury-predictive FE model of the human pelvis and use it to improve our understanding between lateral pelvis loading and injury. Establishing a link between force distribution and injury relating to side impact conditions of the pelvis can lead to a better understanding of injury predictive metrics. The goal of this thesis will be accomplished through the following tasks:

1) Develop a pelvis finite element model using biofidelic geometry, high-fidelity meshing schemes, suitable material models from literature, and potentially, optimization.

2) Benchmark the response of the human pelvis to post mortem human surrogate tests, corroborating injury prediction and force response.

3) Analyze the injury thresholds of the FE pelvis to assess suitability of existing injury predictive metrics.

Biofidelity of the FE model will be assessed by comparing experimental response data such as load cell forces with FE tracked data, while also visually verifying that the kinematics of the model correspond with videos of tested PMHS specimen. Injury prediction ability will be evaluated by comparing the FE predicted fractures to the injuries found in tested PMHS specimen. Photographs, X-rays, and CT scans of these cadaveric injuries can be individually compared to the injuries predicted by the model.

The work contained in this document will be presented in the following chapters. A flow chart can be viewed in Figure 2, outlining the structure of this thesis. The outcomes of this work will advance understanding in the field of biomechanics related to the human pelvis in dynamic lateral impacts. Creation of a high-fidelity pelvis model that is benchmarked for dynamic lateral impacts will be valuable to understand side panel intrusion in blast events. In the future, this pelvis model will be integrated into a more encompassing human body model to be used in evaluation of other dynamic loading conditions. A comprehensive human body model can lead to safety improvements to protect the warfighter. Furthermore, this research will address a question related to lateral impact, particularly ATD instrumentation and IRF development. What are the injury mechanisms for lateral pelvis impacts and what is a better injury prediction metric, anterior or posterior pelvic force? Identifying valid injury predictors and understanding injury mechanisms are essential for protecting the pelvis in lateral loading.

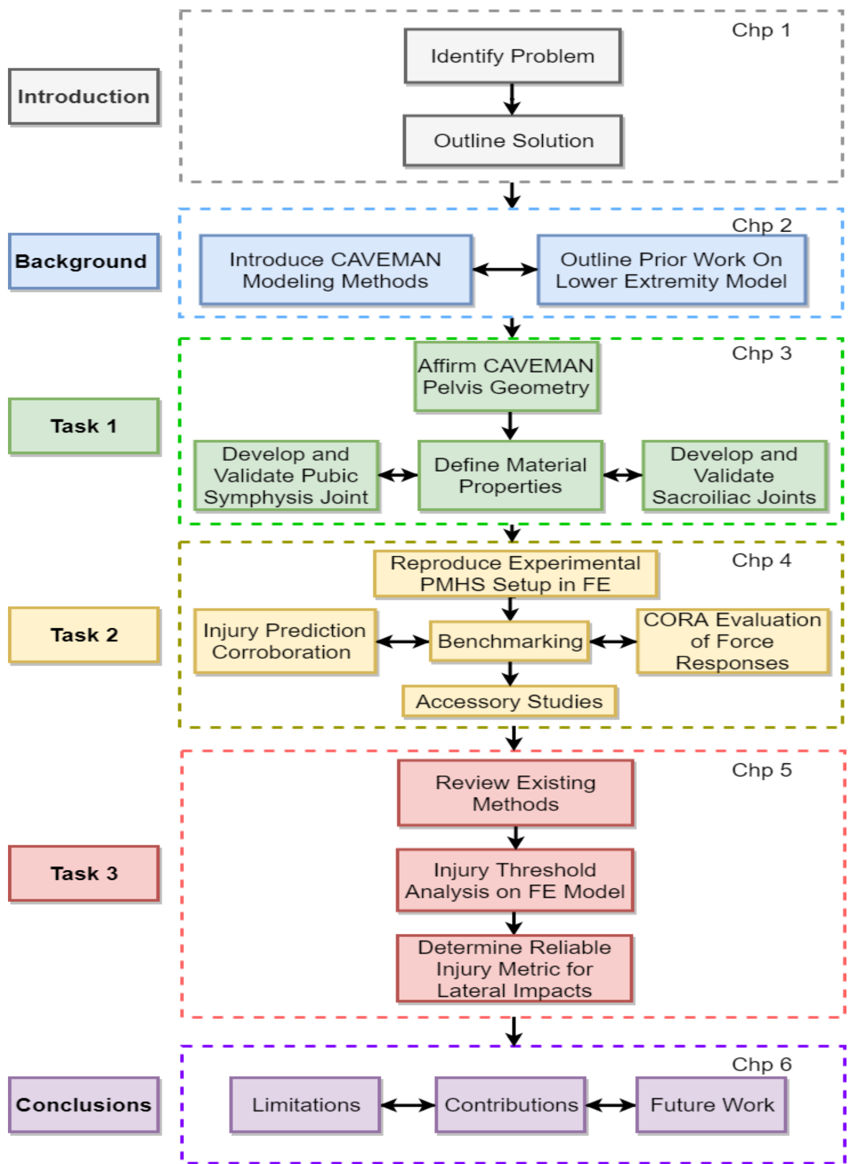

Figure 2: Flow chart outlining the structure of this graduate thesis

CHAPTER 2: BACKGROUND

This chapter outlines the approach to be followed for future model development pertaining to this thesis. Background information will be given on prior modeling efforts with an injury predictive lower extremity model which highlights the sensitivities observed, guiding future development and analysis methods.

2.1. CAVEMAN Modeling Approach

CAVEMAN is an acronym for "Computational Anthropomorphic Virtual Experiment Man" which is a high-fidelity detail oriented human body FE model developed by Corvid Technologies for use in the military environment. The CAVEMAN model represents a 50th percentile male, and aims to limit the use of assumptions in its design. The model includes representations of specific biological tissues such as bones, muscles, tendons, ligaments, cartilage, and connective tissues (Figure 3). Components of the model are meshed individually, with the vast majority of elements being hexahedron. The human body model was meshed in a standing position. Material models used are chosen to reduce as many assumptions as possible, by incorporating the mechanical characterization of biological tissues most recently reported in literature. These models incorporate viscoelastic rate effects and loading direction dependencies where applicable. Further explanation of the modeling approach that CAVEMAN utilizes follows in 2.1. Since the lower extremity model has been most refined, much of the visual aids in this

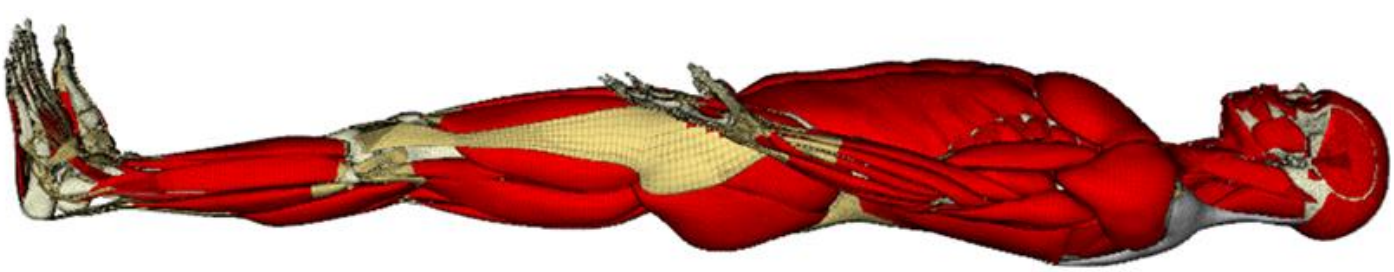

Figure 3. The CAVEMAN FE Model (rotated 90 deg. from a standing posture).

explanation will relate directly to the FE lower extremity. CAVEMAN is currently being developed to expand modeling on a variety of high intensity loading environments including occupant injury analysis of military vehicles. However, the future applications for which the model could be used are numerous: automotive crashes, ballistics, surgical simulation, and orthopedics.

2.1.1. Summarization of Corvid Technologies FE Solver: Velodyne

The CAVEMAN model runs on a custom FE solver developed by Corvid called Velodyne. Velodyne is a multi-physics, parallel nonlinear FE solver initially developed to evaluate the effectiveness of interceptor missile debris fields for the Missile Defense Agency (MDA). Velodyne's success at modeling these extreme conditions led to its expansion for analyses in combat vehicles, such as the MRAP vehicles, in order to assess survivability against underbody blasts.

Many numerical methods used in Velodyne such as hourglass controls, single integration point solid (at center) elements, and central difference time integration are similar to LS-DYNA (Hallquist, LSDYNA Theory Manual 2006). Some other interesting features built into Velodyne are: implementation of smooth particle hydrodynamics (SPH), parallel performance optimization, coupled fluid-structure interaction, multi-phase equations of state (EOS). Perhaps the most defining feature of Velodyne is the propriety auto-contact algorithms it utilizes. This algorithm is more computationally costly than standard penalty contact methods used in other solvers which allow small penetrations, but the algorithm is especially effective for high rate impact problems. Using the global contact scheme, there is no need to predetermine where contact will take place, which can save time in complex simulations that involve fast moving and uncertain events. Defined contacts in Velodyne can also use a slave-master formulation for node-segment contacts.

Velodyne is continuously being improved and thus frequently updated with new versions. Velodyne versions 3.008.03 and 3.103 were used in this study.

2.1.2. CAVEMAN geometric modeling methods

The CAVEMAN human body model geometry was developed by Zygote Media Group, based on CT and MRI scans of a 50th percentile male human body in a standing posture and takes into consideration anatomy atlas data. Anatomy provided includes: bones (distinguished between exterior cortical and interior cancellous), muscles, ligaments, skin, cartilage, and organs. For the CAVEMAN geometry, 135 body anatomical measurements were compared to those reported in the military studies (ANSUR I Gordon, Churchill, et al. 1998, ANSUR II Gordon, Blackwell, et al. 2014, Handbook Military, 1991). These military studies span from 1946-2012 and include several hundred human body measurements, which are related to specific percentile groups for both males and females. The average measurement error between CAVEMAN and reported 50th percentile male geometry was 4.5%. Table 1 provides a lower extremity example comparison of anthropometric measurements between CAVEMAN and the literature (Butz et al. 2017). The geometry provided by Zygote includes all skeletal and soft tissues included in the model, but in order to expand fidelity a “void fill” geometry was created in order to fill the gaps between tissues that do not necessarily have significant mechanical function.

Table 1. Example CAVEMAN lower extremity anatomical measurements compared to U.S. military data anthropometric studies. (Butz et al 2017)

Measurement Number	Measurement Description	Survey: 50th % Value (cm)	Survey: Standard Deviation (cm)	CAVEMAN Value (cm)	Error (%)	Error (cm)	Reference
19	Bimalleolar Breadth	7.33	0.39	6.9	5.9%	0.4	ANSUR II
67	Foot Breadth	10.12	0.53	9.6	5.1%	0.5	ANSUR II
68	Foot Length	27.10	1.28	26.4	2.6%	0.7	ANSUR II
99	Instep Length	20.03	1.01	19.8	1.1%	0.2	ANSUR II
108	Knee Height, Midpatella	49.53	2.79	49.9	0.7%	0.4	ANSUR II
110	Kneecap (Patella) Height	51.20	2.71	51.7	1.0%	0.5	DOD-HDBK-743A
113	Lateral Malleolus Height	6.94	0.70	7.3	5.2%	0.4	ANSUR II
119	Medial Malleolus Height	8.60	0.57	8.9	3.5%	0.3	DOD-HDBK-743A
162	Sphyrion Height	6.60	0.63	6.5	1.5%	0.1	DOD-HDBK-743A
176	Tibiale Height	47.83	2.60	46	3.8%	1.8	ANSUR II

2.1.3. CAVEMAN meshing methods

The majority of components in the CAVEMAN model were meshed with solid single point integration hexahedral elements except, for example, the fascia and skin which were meshed with four node shell elements. The CAVEMAN human body FE model was meshed using three different meshing software: CUBIT (Version 14.1), TrueGrid (Version 3.1.0), and Bolt (Version 1.2). The software tool used was determined by the geometry of the component being meshed. Regular shaped components were meshed using CUBIT with pave meshing schemes extruded through the solid body; this method produced the highest quality elements in the model. Note that for soft tissues such as ligaments and muscles, the axis of mesh extrusion was aligned so that it would match the anatomical fiber direction. This type of meshing scheme for soft tissues with strongly oriented fiber directions allows for proper use of anisotropic material models which include loading direction dependency (Section 2.1.4). For soft tissues where there exist large transitions in cross sectional thickness, TrueGrid was used. TrueGrid allows for mesh density to vary though out the width and thickness of a component while allowing for a 2:4 or 1:3 ratio split to create a transition region while preserving node connectivity. Bolt is an automatic hexahedral mesh generator that works well for components with smooth edges. Bolt meshes are used primarily for irregular shaped bones in the CAVEMAN model. Being that Bolt is an automated meshing software, it is extremely quick in generating meshes compared to the other methods. As mentioned,

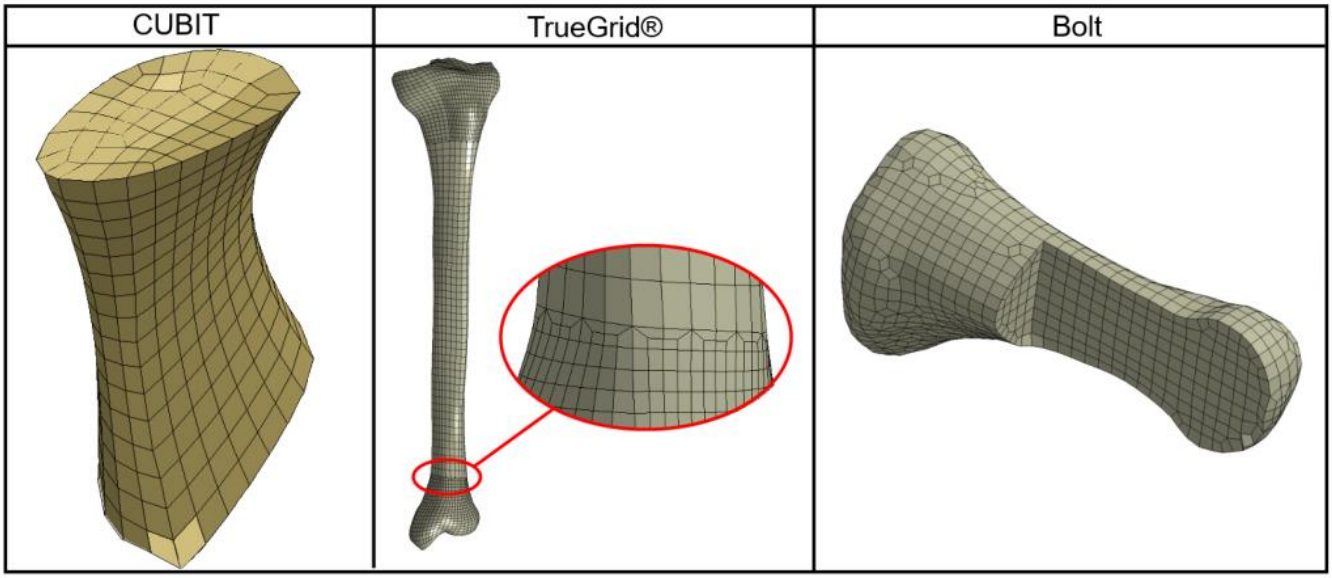

Figure 4: Comparison of the three different types meshes created by CUBIT (left), TrueGrid (center), and Bolt (right) for the CAVEMAN human body FE model (Butz et al. 2017).

the gaps between the tissue geometries provided by Zygote were filled with a solid hexahedral mesh, this void fill mesh was also meshed with Bolt to ensure proper load carrying through the intermediate spaces between the primary biological components. These Bolt meshes have a uniform base mesh for interior elements and a pillow layer on outer surfaces. A comparison between meshes created from all three software can be viewed in Figure 4. The irregularities of the surface level pillow layer in the Bolt automatically generated mesh can be observed as well as the properly oriented interior mesh. Although the surface mesh is irregular the cross-sectional view in Figure 4 illustrates the good quality of the interior generated elements.

Element quality is an issue that can arise with FE models, thus it was kept in mind during the meshing process. Time step for a Velodyne simulation is defined by element size and material definitions. A target time step of 0.1 μs was set so that the characteristic length of elements was acceptable for each type of tissue. This target time step was chosen since it is the criteria used in military vehicle simulations done at Corvid. The average characteristic length across the lower leg model is 0.26mm and ranges from 37 μm to 1.4 mm. Target scaled Jacobian criteria was set to greater than 0.4 and an aspect ratio of under 10. Scaled Jacobian is an element quality metric that measures the normal of the element faces compared to each other. A Scaled Jacobian of one is a perfect cube. As an example, 94% of elements in the lower extremity model meet the scaled Jacobian criteria and 99% meet this aspect ratio limit. Elements that do not meet the cutoff criteria are normally located at edges of soft tissues where small curvatures exist. No noticeable stability problems have arisen from the limited poorer quality elements.

Since components of CAVMEN are meshed individually, they are assembled together using tied node sets at anatomically described insertion points. Tied node sets are good for modeling tied contact by creating a connection between a set of both a slave and master node set. In these tied node sets, the master segment sets have been defined as the skeletal surfaces while the slave node sets are on the ends of soft tissues. These tied contacts do not permit any relative motion between the slave nodes and their location on the master segment set, while permitting bending and deformation of elements adjacent to the master segments. The utilization of tied sets allows for a biofidelic representation of load transmission through the bone-ligament-tendon structures, one where relative motion is dictated by the anatomical connections of the model. The method reduces the assumption and uncertainty that is introduced in models which utilize idealized joint structures. An example of tied set interfaces can be viewed in Figure 5.

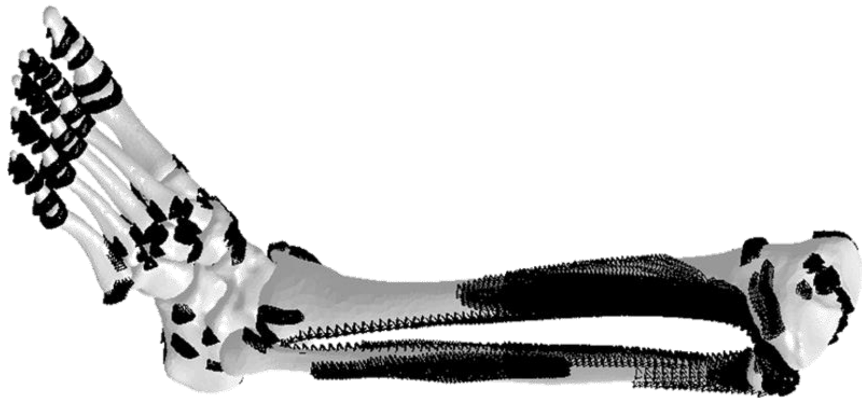

Figure 5: Lower extremity tendon and ligament tied set insertion sites (highlighted in black) connecting to bone, for the CAVEMAN lower extremity.

2.1.4. CAVEMAN material modeling

There are a number of reported constitutive models related to the human body, which reflects the functional and mechanical variance of biological tissues. The CAVEMAN model uses existing material models selected from literature that best model tissue responses in high rate loading conditions. The FE response of these models such as stress-strain curves are compared to those in literature derived from experimental testing. These models can become quite complex, sometimes accounting for directional loading variability and viscoelastic strain rate sensitivity.

The material models of the CAVEMAN FE model, which have been properly developed as of 2019 will be described. A more complete description for the material models and applicable constitutive equations used for the lower extremity and pelvis can be viewed in Appendix A and Table 3, respectively. Bones, modeled with a split bone elastic-plastic (E-P) material model are crucial due to their importance in force transmission and injury potential. The outer regions of bone were assigned as stiff cortical bone and the interior of the bone was assigned as cancellous bone. Both cortical and cancellous bones were assigned a yield strength and tangent modulus. Deletion of cortical bone elements to model fracture were dictated by an ultimate principle strain value. This is a technique used in other FE modeling studies (Bailey 2016, Untaroiu et al. 2008) and is useable in the CAVEMAN model since the generated mesh refined.   As elements hit this strain threshold they are deleted from the simulation. This is where having a high-fidelity mesh is useful, since a fine mesh can better capture fracture propagation. Models with coarser meshes would have problems modeling fracture with element deletion since large amounts of material are being removed quickly.

Ligaments in the CAVEMAN model that were subject to large deformation or considered important to force transmission were modeled with a transverse isotropic hyperelastic material model, with collagen fiber direction being assigned consistently with anatomical descriptions. Ligament fiber direction is most commonly described anatomically as having the orientation of the collagen fibers in the tissue being directed parallel to one other and directly connecting bone. This gives the ligament increased stiffness in tension comparatively less stiffness in bending or compressive loading. Fiber direction was assigned on a per-element basis, where a vector was defined by each element's nodes. The ligament material model used in CAVEMAN is similar to that reported by Quapp and Weiss (1998) on the medial collateral ligament. Muscles are described by an Ogden viscoelastic constitutive model for strain rates ranging from 0.007/s to 3700/s. This material model was created by using an optimized fitting procedure reported in Song et al. (2007). This method fit the response of the muscle in the cross fiber direction for different loading rates, with viscoelastic terms chosen to fit the rate dependent response. This optimization locks down hyperelastic (non-linear stress response increasing with strain) material parameters at a low strain rate, before determining the viscoelastic constants. Tendons connecting the muscles to bone were also modeled with a transverse isotropic hyperelastic material model. Tendons were assigned the same material model as the ligaments, however the magnitude of their material stiffness parameters were increased making them stiffer in both compression and tension. Muscles and tendons have directionally dependence similar to the ligamentous structures, thus fiber directions were assigned. Cartilage was modeled as isotropic neo-Hookean, while skin and fascia was defined with a linear elastic material model. Future developments and updates will be dictated by available mechanical characterization studies of tissues, particularly as other body regions are modeled further such as the brain and other organs. Having an encompassing data base of biological tissue characterization is valuable to the field of biomechanics as a whole.

2.2. Prior Modeling Efforts: CAVEMAN Lower Extremity

IED blast loading strongly effects the body regions of the soldier that are in contact with the vehicle: the lower extremity and pelvis. Thus initial modeling and validation efforts for the CAVEMAN lower extremity modeled were centered around the lower extremity and later the pelvis. Prior to working on the pelvis, analysis of the existing lower extremity was performed for this graduate thesis to better understand the CAVEMAN model performance in injurious loading conditions. This work proved valuable as it elucidated which tissue components were driving the response and also injury predictions of the model.

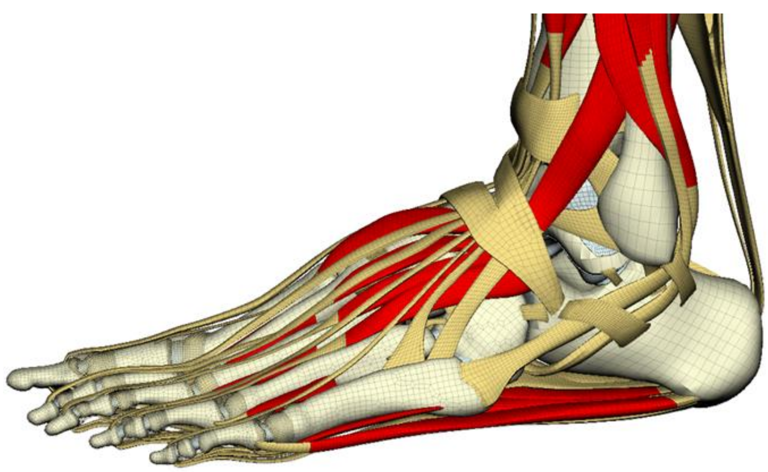

Figure 6: Sub-assembly of the CAVEMAN lower extremity showcasing bones, muscles, and ligaments of the foot.

2.2.1. Lower extremity model

The CAVEMAN lower extremity FE model consists of 28 bones, 26 muscles, 40 ligaments, cartilage, fascia, skin, and a void fill. The geometry of the lower extremity model was compared to military anatomical measurements and was found to have just a 3.0% error from those reported for the 50th percentile male. The lower extremity model consists of: 1,014,387 solid elements (hexahedral), 18,851 shells, and 267 tie sets. Pertaining to element quality, 94% of the solid elements have a scaled Jacobian greater than 0.4 and 99% have an aspect ratio under 10. Material models used in the lower extremity are consistent with those described in the previous section. Parameters were determined from either literature or parameter optimization. The heel pad and fat of the foot is modeled with an Ogden viscoelastic model. The model used is from dynamic compression testing done at the University of Virginia (Gabler, Panzer, and Salzar 2014). A full constitutive model and parameter description of the CAVEMAN lower extremity can be viewed in Appendix A. Figure 6 illustrates with detail how the bones, muscles, tendons, and ligaments of the foot model.

The CAVEMAN lower extremity model has been benchmarked to numerous sub-injurious and injurious PMHS tests. A prior study (Butz et al. 2017) performed a deeper analysis into the lower extremity models behavior in sub-injurious loading conditions. A similar model response study was thus performed in a controlled injurious loading environment, to see the effect that model parameter variation has on injury.

2.2.2. UVA axial impact tests of PMHS lower extremities

In order to perform a parameter study on the CAVEMAN lower extremity, injurious experimental impact conditions were validated. Twenty-four lower extremities from 12 donors were tested with a pneumatic linear impactor at The University of Virginia Center for Applied

Biomechanics. Anatomical details of the twelve male donors include: an average age of 58 years old, average length of 476 mm, and an average body mass 86.76 kg. The loading environment of these PMHS tests was designed to replicate vertical floor intrusion during an UBB event impacting the bottom of the foot. The test setup consisted of medium severity and high severity loading scenarios. A complete comprehensive description of this test series was obtained from the PhD dissertation of Dr. Ann Marie Bailey (Bailey 2011).

The UVA-Bailey testing apparatus was recreated and meshed in order to try to replicate the experimental setup. The lower extremity model was repositioned to match average anatomical positioning angles observed in X-ray scans of the PMHS specimens. The model was “settled” to replicate preload applied to the lower extremity during the cadaveric test. This consisted of applying a 126 N load on the impact plate pushing into the foot for a duration of 150ms. Velocity curves derived from experimentally tracked acceleration traces were applied as input to the impactor plate. Peak velocity for the two conditions measured as 2.4 m/s for the “medium” impact condition and 4.5 m/s for the “high” impact condition. Opposite to the input, the tibia of the leg was potted and rigidly constrained. Simulations were run out to 30ms for the medium case and approximately 20ms for the high case. Due to the severity of the high impact condition and extensive deformation to soft tissues, computational stability became an issue with anything run past 20ms.

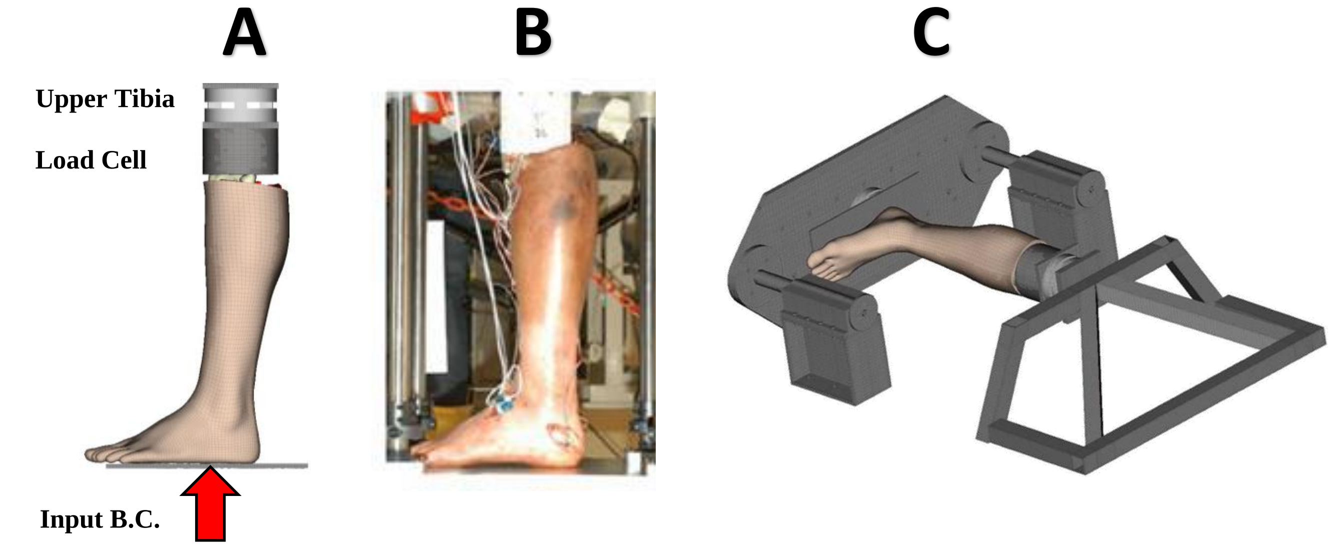

Figure 7: (A) Description of input and load cell for FE analysis. (B) Cadaveric illustration of the leg before impact. (C) FE recreated experimental apparatus.

2.2.3. CAVEMAN lower extremity force response and injury prediction

The CAVEMAN lower extremity model was compared to the PMHS data in its prediction of injury and matching of force response. Figure 8 compares force-time histories of the upper tibia load cell for both medium and high impacts. For the medium impact the CAVEMAN force trace lies in between the upper and lower experimental corridors for the 30ms duration of the simulation. The force at fracture was 6.83 kN compared to an experimental average of 8.29 kN (0.670). For the high impact condition, the CAVEMAN force peak was slightly out of phase from the experimental corridors, but the shape of the trace compared favorably. The force at fracture was 8.95 kN compared to an experimental average of 9.98 kN (0.620). Overall, based on the two impact conditions, it appears the CAVEMAN lower extremity under predicts fracture force in both loading scenarios. The shape of these data traces compare favorably with the PMHS corridors.

Based on this corridor, the force transmission of the lower extremity was understood and evaluation of the element deletion related injuries were examined.

Figure 8. Upper tibia force-time history of the CAVEMAN lower extremity model compared to the experimental corridors for the medium and high impact condition.

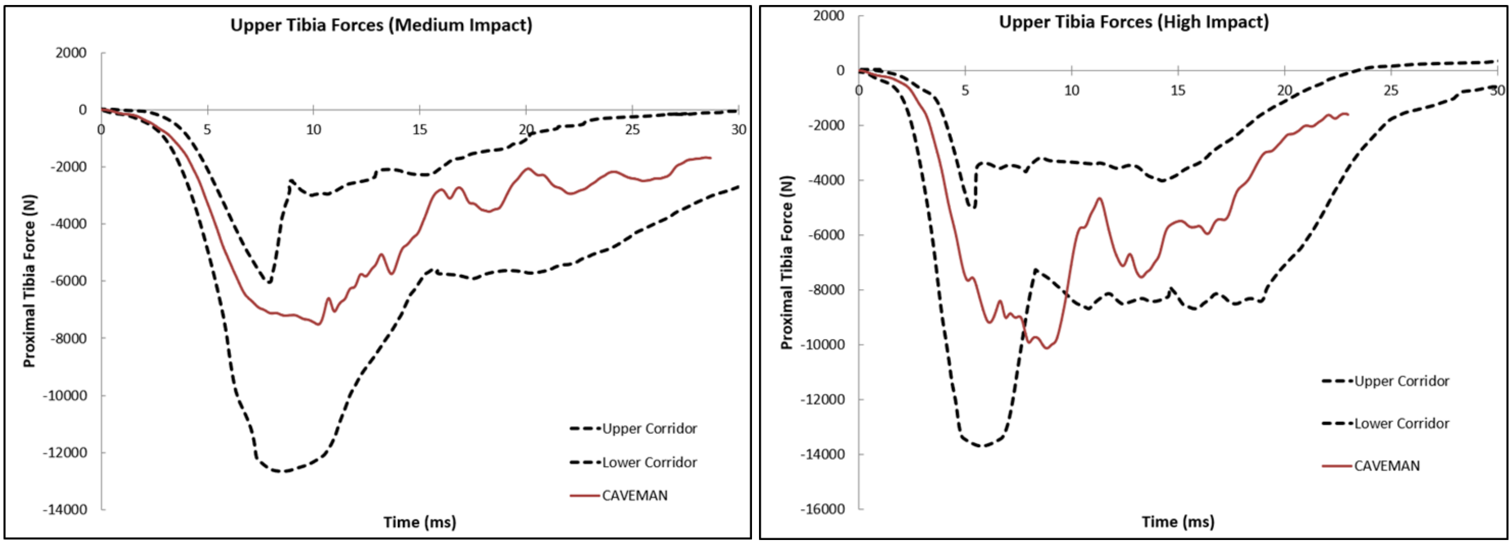

Injuries observed in the lower extremity model are comparable to those observed in the cadaveric data set (Figure 9). Fractures to the calcaneus were observed in both the medium and high impact conditions. In Bailey's experimental scenarios where the calcaneus did not break, fractures of the distal tibia were more likely to occur. Importantly, predicted severity of injury was clearly distinguishable between the two impacts. In the medium impact, deletion of the calcaneus was observed, however, the structurally integrity of the bone was not completely compromised. In the high impact, the calcaneus experienced a comminuted fracture which resulted in the bone breaking into multiple fragments. Although simulating fracture by element deletion is a simplification, the fine mesh used in the CAVEMAN model reproduces injury characterization favorably, even for the less severe fracture occurrence.

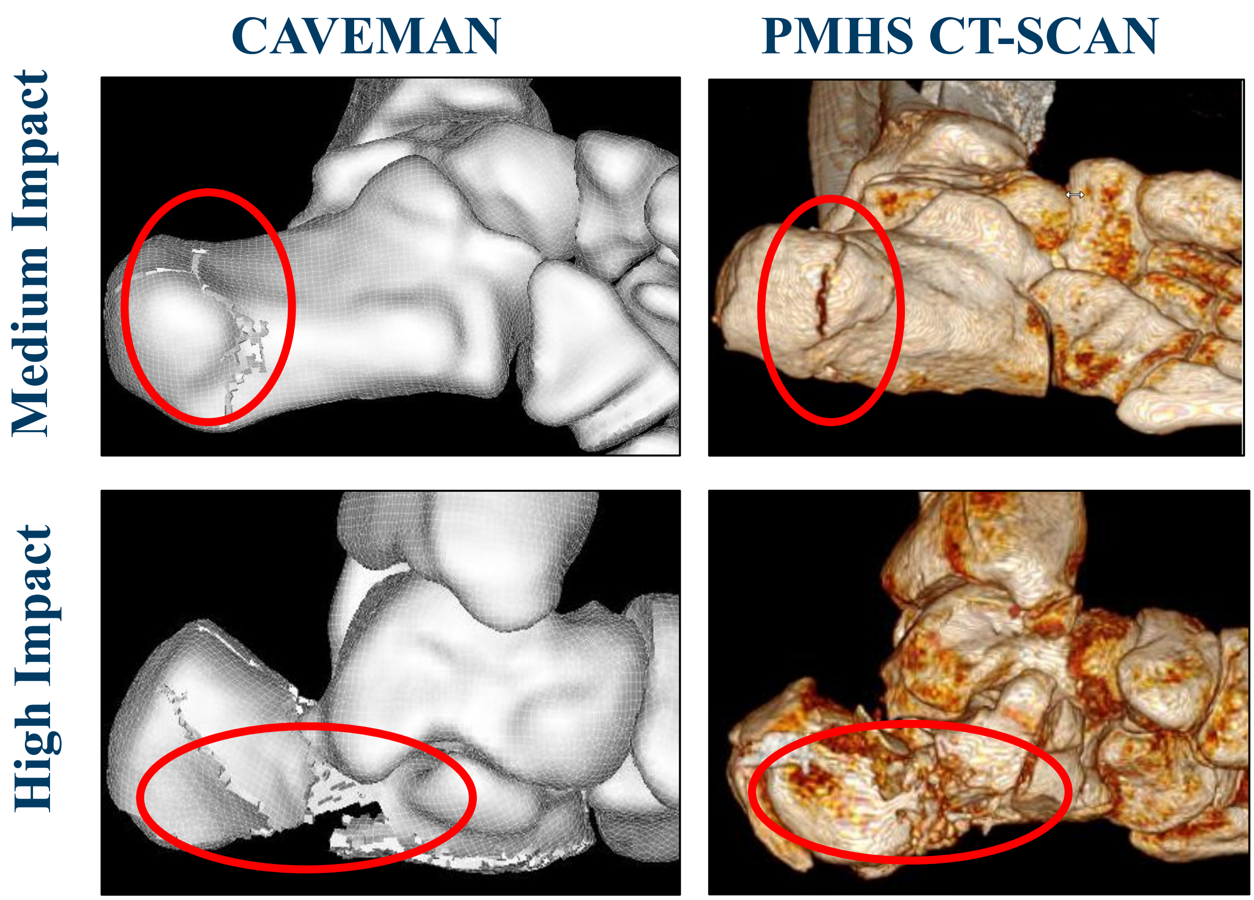

Figure 9: CAVEMAN fracture predictions according to the "medium" and "high" impact condition compared to CT reconstructions of PMHS lower extremity post-test.

2.2.4. Lower extremity sensitivity study in UVA impact conditions

A sensitivity study was performed on the CAVEMAN lower leg extremity in the UVA testing configuration. This comprised of applying variations to positioning angles, anatomical geometry, and material stiffness parameters. These simulations were run without pre-impact settling in the interest of saving computational time. The goal of this study was to gain further insight into what was driving the response and predictions of the model and identify potential improvements.

For the medium and high baseline impacts, the CAVEMAN leg was positioned to match pre-impact X-ray scan averages of PMHS specimens. The difference in ankle-flexion angle between the medium and high tests was 4.6 degrees. It was decided to run a medium impact in the high configuration (90.6 degrees) and a high impact in the medium configuration (86.0 degrees) in order to see how this variation effected force response and injury prediction of the CAVEMAN leg. The CAVEMAN leg did not show significant peak force sensitivity to the ankle-flexion angle, in the ranges (86 – 90.4 degrees) that were studied. What is of interest is the role positioning angles had in the initial loading rate. The reduced angle run for both the medium and high impacts loaded at a faster rate, and led to fracture happening slightly earlier. It appears that slight variation in the range of ankle-flexion angle found in a PMHS data series does not significantly affect the CAVEMAN force response or injury prediction. It is hypothesized that varying ankle position angles by a greater degree, as done in other studies (Portier et al. 1997, Kura et al. 1998) would have a more apparent effect.

Thickness of the cortical bone layer in the calcaneus is known to vary by individual (Sabry et al. 2000, Kumar et al. 1991). It is postulated that this variation will have an impact on the susceptibility of the calcaneus to fracture. The thickness of the calcaneus was adjusted by reassigning interior elements to either cortical or trabecular bone. To go from baseline to “thinner”, the interior elements of the isolated cortical bone part were reassigned. For areas where the cortical bone was only one element thick, no changes were made. For the “thicker” model the first layer of interior cortical bone elements was reassigned. Figure 10 provides a visual aide to illustrate that the percent volume of cortical bone plays a significant role in the response of the entire lower extremity. This details that in future modeling efforts accurate measurements of the cortical bone thickness are needed to establish a consistent injury prediction.

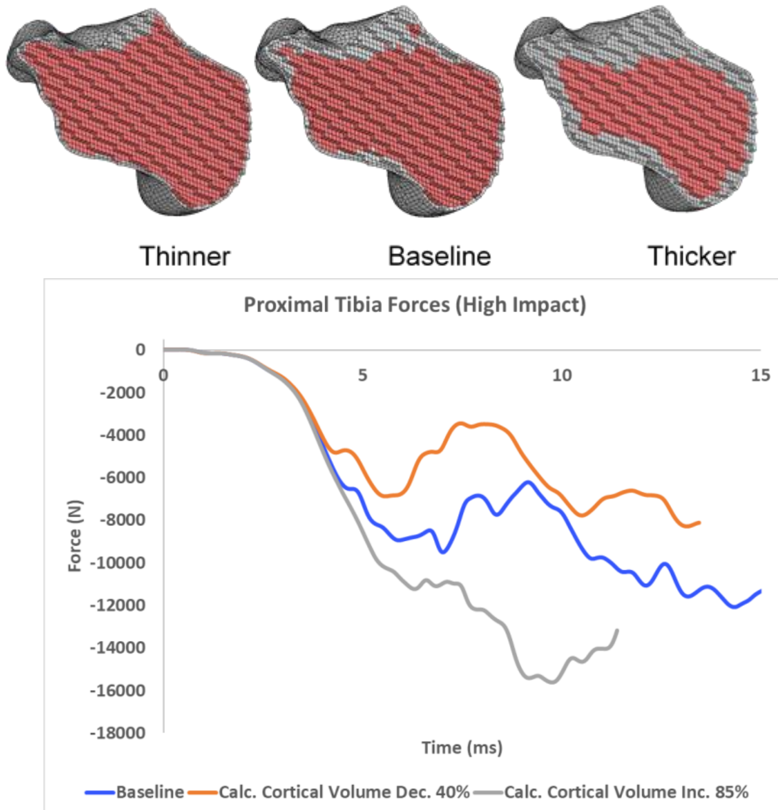

Figure 10. Force sensitivity of CAVEMAN lower extremity to changes in the cortical bone thickness. Since it was done on a per layer basis, the change in cortical bone will be reported in % volume change.

The CAVEMAN lower extremity consists of components defined by different material types. Groups of these components present in the CAVEMAN model include: muscles, tendons, ligaments, skin, fascia, cartilage, as well as cancellous and cortical bone. Sensitivity studies performed in the past found varying levels of sensitivity to material properties (Akrami et al. 2017, Cheung et al. 2005). The Corvid Technologies team previously performed a material stiffness sensitivity study on the lower extremity model (Butz et al. 2017), but this study was done using sub-injurious loading conditions. In this prior study, the model response was strongly sensitive to changes in the ligament material stiffness definition. It can be expected that the model will show a similar force response dependence on ligament stiffness as it did before. What this study will contribute is knowledge on the effect these variations will have on injurious impact, in which elements are being deleted to model skeletal fracture. The study performed in Butz et al. 2017 was replicated. The stiffness of muscles, tendons, heel pad, cortical bone, cancellous bone, and ligaments ranged from baseline to the extreme ends of the stiffness reported in the literature.

The results of the material sensitivity study showed a significant force response sensitivity to ligament material properties as was found in Butz et al. 2017. Other variations were not strongly sensitive. Figure 11 compares data traces from the baseline and two variant medium impact runs. The less stiff (0.1x) ligament lower extremity reached peak forces that were less than one-third that of the baseline model. The stiffer (10x) model hit peak forces slightly more than the baseline, but the drop off in ability to transmit force becomes especially apparent around 10ms where there is an unloading of the lower leg. This is due to the increased severity of fracture modeling occurring in the stiffer model where the calcaneus comminutes. These types of sensitivities were not observed to this extent in other parameter changes.

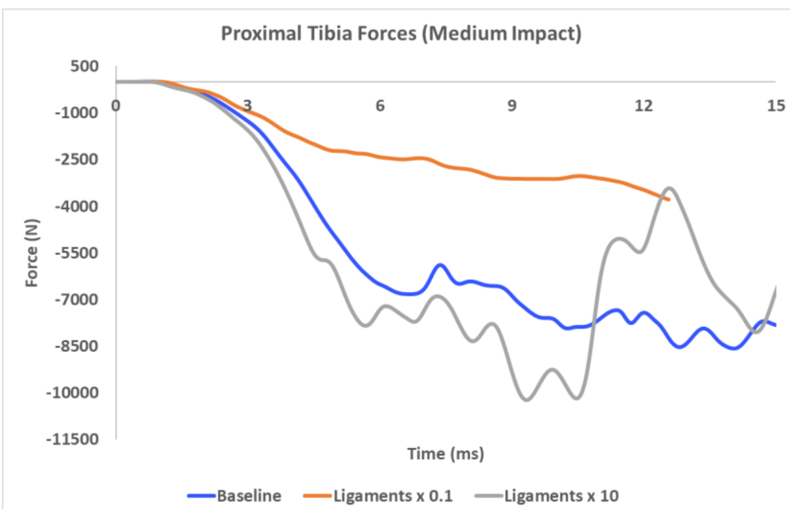

Figure 11. Force sensitivity of CAVEMAN leg to changes in ligament stiffness. Significantly less force transmission occurs in the lower stiffness model. Forces in the higher stiffness model are marginally higher than the baseline, but the unloading phase is more abrupt.

The influence of ligament material stiffness had a profound influence on the kinematics of foot bones as seen in Figure 12. Softening of the connective tissues led to a gap developing between the calcaneus and cuboid. In turn this allowed force to be dissipated and no injury or element deletion to occur, since the forces that would result in fracture in the hindfoot are distributed toward the forefoot. In the opposite scenario, stiffening of the ligaments kept the cuboid and calcaneus bound tight, with more severe fracture occurring. Additionally, element deletion was observed at the ligament bone interface modeling similar to an evulsion type fracture. The current ligament constitutive models do not support viscoelastic characterization, thus due to the observed sensitivity to stiffness, including strain rate effects could be beneficial to future modeling of soft tissues in the CAVEMAN model, as this experimental data becomes available.

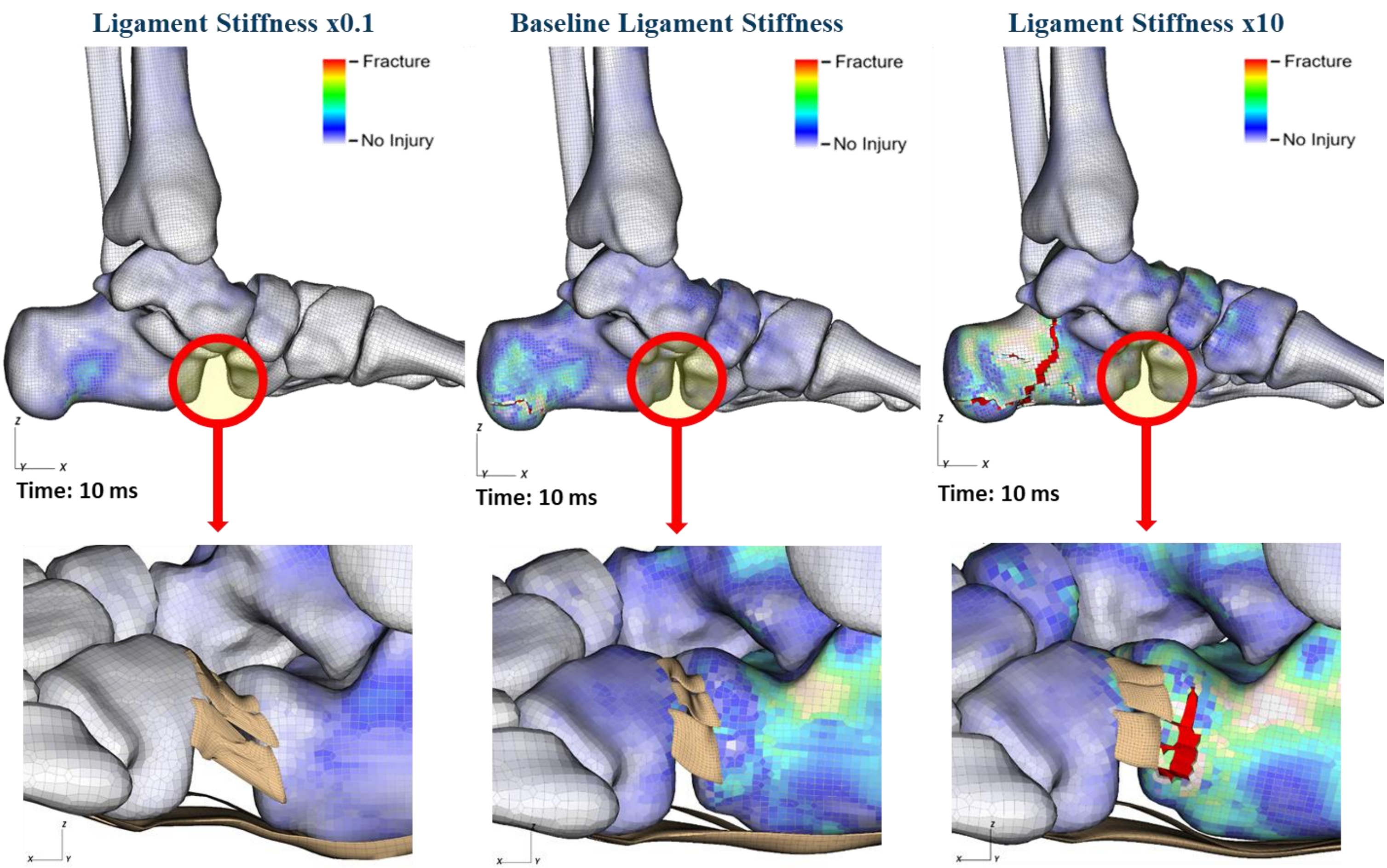

Figure 12. . The parameter sensitivity of ligament stiffness during a "medium" impact in the UVA rig. The less stiff ligament foot spreads apart more easily, preventing force transmission. The higher stiffness model has less calcaneo-cuboid spacing, leading to greater force transmission and more significant fracture. Notice the evulsion fracture at bone-ligament interface.

2.3. Summary

The CAVEMAN human body FE model is being developed to assess high rate loading conditions, particularly those found in military blast related loading scenarios. The model runs on Corvid's in house FE solver Velodyne, which is differentiated from other explicit solvers such as LS-Dyna by its propriety contact algorithms. CAVEMAN geometry was obtained through Zygote Media Group's scan derived geometry from a 50th percentile male. Geometry has been compared to military anthropometric studies to validate the 50th percentile male definition. Three different tools have been used to generate FE meshes: Cubit, TrueGrid, and Bolt. The majority of elements in CAVEMAN are single point integration hexahedral elements and the mesh has a higher resolution when compared to existing human body models. Tied sets are used to attach the node sets of connective tissues directly to bones. Material models are chosen so that the mechanical response of the tissues can be accurately represented. For the lower extremity, there are seven different constitutive models used to model: bone, ligament, skin, cartilage, heel pad and fat, muscle, and tendon. As the mechanical properties of these tissues become better understood from experimental testing, the CAVEMAN model will be updated accordingly.

The main conclusion from the lower extremity study was that ligamentous connective tissues played a significant role in the response and injury prediction of a human body FE model developed according to the CAVEMAN modeling process. The alterations to the material properties of the muscles, tendons, and heel pad did not particularly effect the response of the FE model or its injury prediction. The use of tied sets allows for the connective tissue to dictate the bone kinematics and force transmission, leading to a clear dependency on ligament material description. This provides evidence that future development of other body regions must take into strong account connective tissue modeling, particularly at joint regions.

CHAPTER 3: DEVELOPMENT OF CAVEMAN PELVIS MODEL

This chapter addresses the development of the CAVEMAN pelvis model to evaluate lateral impact conditions representing side panel intrusion during military blast. This development process builds off the previous chapter's modeling efforts related to the lower extremity. Since the lower extremities and pelvis are the points of contact of a warfighter seated in a vehicle, the pelvis was the next logical modeling task. If this pelvis model can be developed and later benchmarked to experimental tests, it can be used in a FE study to provide insight into the biomechanics of lateral pelvis loading. Integration of this model into an encompassing human body FE model is an eventual goal, to evaluate complex loading scenarios related to the occupants of military vehicles.

3.1. Development of the Defleshed Pelvis

The creation of this model was to follow the Corvid development processes that were outlined in Chapter 2. Subsystem validation of connective regions will be performed later before the full pelvis model is analyzed together, as well as unit cube material validations of bone materials. Attention will be paid both to the cortical bone thickness descriptions and connective tissues since they were shown to dictate the response of the lower extremity.

3.1.1. CAVEMAN pelvis geometry and mesh

The geometries of the CAVEMAN pelvis have been validated in the previous military data comparison as described in the background model development-geometry section. This geometry provided by Zygote has been shown to compare favorably to the military's description of a 50th percentile male. To further confirm accuracy, the CAVEMAN pelvis was compared to measurements of defleshed pelvis that were recorded in Salzar et al. 2011's data set where it was within a few millimeters of each measurement (Figure 13). Dimensional accuracy is critical, since improper geometry can lead to incorrect computational results. Geometry related variation is understood to largely effect FE results, as has been shown in mesh morphing studies (Zhang et al. 2017, Jastrzebski, Poulard, Panzer 2017).

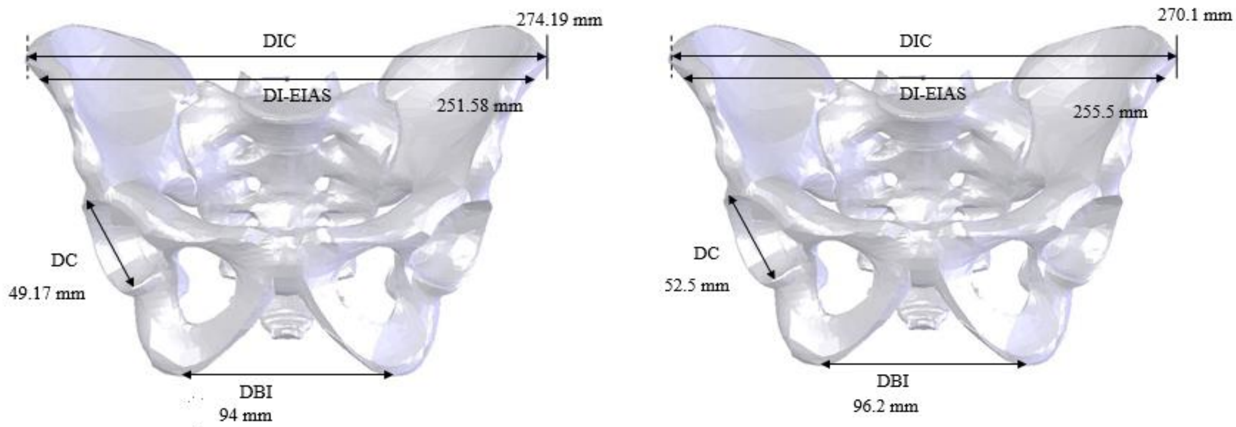

Figure 13. (left) Average geometric measurements from pelvis PMHS specimens (n=16) from Salzar et al. 2011 compared to the CAVEMAN pelvis (right).

Pelvic cortical thickness was compared to literature sources. Due to the sensitivity that was observed in cortical thickness in the lower extremity studies, it was deemed important to have thicknesses that were within range of those reported in literature. Richards et al. 2011 used quantitative computed tomography to measure cancellous density and cortical thickness at different locations of adult sacra (Figure 14). Thicknesses compared favorably within 0.5 mm of those reported in Richards. Anderson et al. 2005 created an FE model of the pelvis using subject-specific predictions of pelvis geometry. The cortical thicknesses of the coxal bone were compared to a cortical thickness plot presented in Anderson’s publication. This comparison suggests that the thickness of the CAVEMAN coxal bone is too thick in certain regions, but the minimum thickness values are consistent with those reported in Anderson (Appendix C).

Mesh generation of the bony pelvis model was done through Bolt. For the pubic joint, Cubit was used and tied sets were defined on either side of the joint to connect it to the anterior pelvic bones. Originally, the sacroiliac joints were represented by a shell element mesh wrapping around the coxal and sacrum bones. The sacroiliac joint soft tissue joint structure was later completely overhauled and will be described later in this chapter. Regarding the prior stated scaled Jacobian criteria of 0.4, 93% of elements in the pelvis model met this target. Over 99% of elements met the aspect ratio less than 10 target.

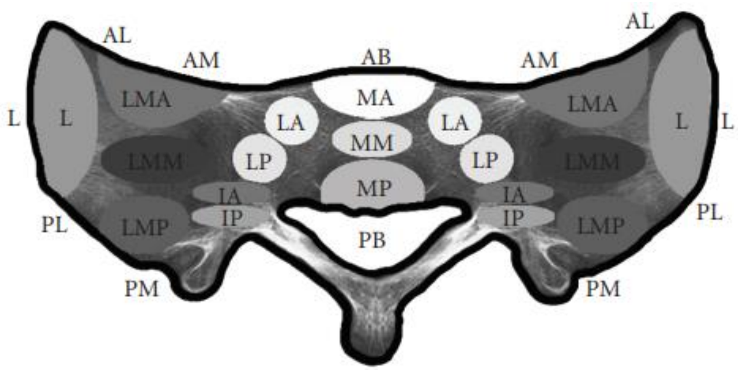

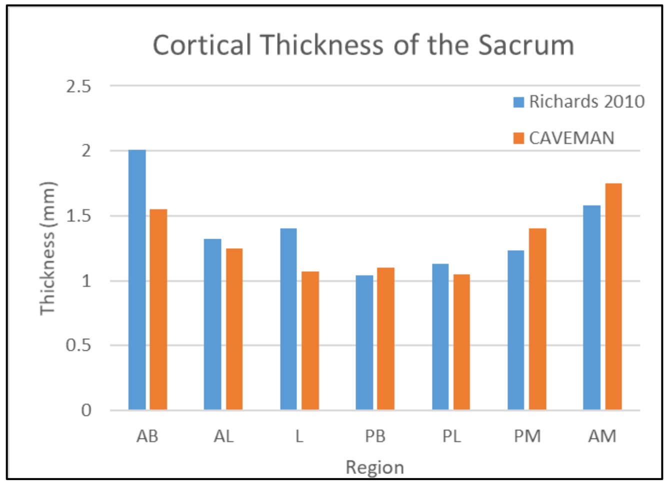

Figure 14. Comparison between the cortical thicknesses of the sacrum reported in Richards et al. 2010 and the CAVEMAN model. Regional location specified in diagram.

The finalized defleshed pelvis model mesh can be viewed in Figure 15. This model will be used for lateral impact analysis and should be considered a sub-assembly of the greater CAVEMAN model. This FE model consists of 127,705 elements of which 22,886 are soft tissues, 47,392 are trabecular bone and 57,427 are cortical bone. Sixteen node sets encompass the connections between soft tissue and pelvic bone.

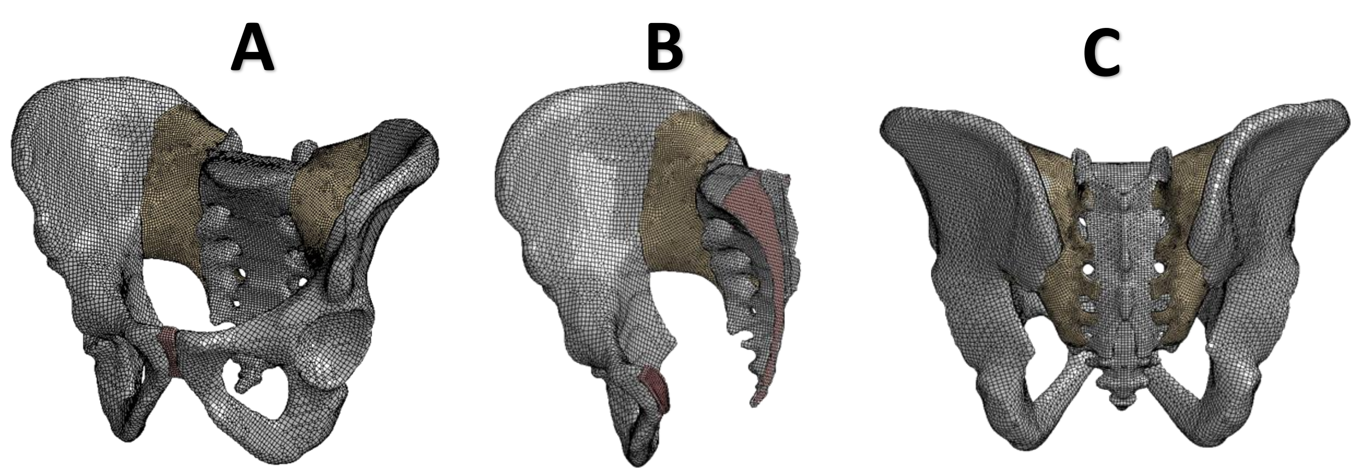

Figure 15. Generated mesh using Bolt and Cubit creating CAVEMAN pelvis model. (A) Anterior-side isometric view. (B) Cross sectional anterior-side view, cut made center of sacrum and pubic joint. (C) Posterior view.

3.1.2. Bony pelvis material properties

A review of published material properties of the bony pelvis was performed to create a proper pelvis FE model. The pelvic bone structure includes the sacrum as well as the left and right ilium. The exterior cortical and interior cancellous bone of the pelvic bone structure were defined with an elastic-plastic material model. This is deemed an appropriate constitutive model for bone, since it captures both the elastic stiffness and weaker plastic stiffness upon reaching a certain yield stress. Similar elastic-plastic material models have been used to describe bone in existing pelvis finite element models (Untaroiu et al. 2008, Li et al. 2013, Mo et al. 2018) as well as in the CAVEMAN lower extremity.

A previous study done in conjunction between Virginia Tech and Wake Forest (Kemper 2008**)** investigated the dynamic material properties of pelvic cortical bone. In this study coupons of pelvic cortical bone were harvested from 4 male cadavers with an average age of 54 years. Coupons were taken from the anterior and posterior sides of the iliac wing, both vertically aligned and horizontally aligned to test for anisotropy due to osteon orientation, as well as from the pubic ramus and ischium (Figure 16**)**.

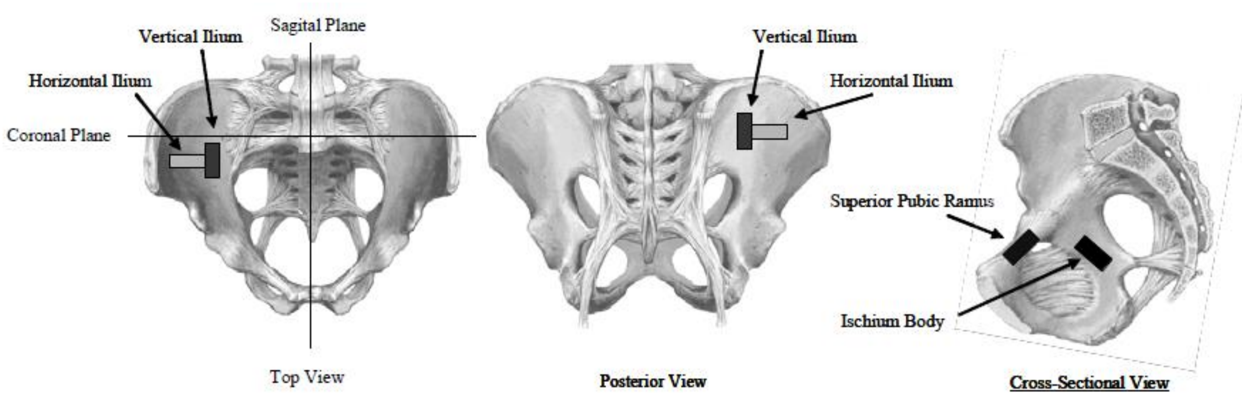

Figure 16. Coupon extraction locations as described in Kemper 2008. Specimen taken at horizontal and vertical orientations.

These coupons were tested in tension at a target strain rate of 0.5 strain/s, with dimensional features being reported (Kemper 2005). Coupons harvested from the anterior ilium suggested anisotropy with increased stiffness in the horizontal orientation, while no discernable anisotropy was observed on the posterior side. Although no directional sensitivity was found in the posterior coupons, it is possible that osteon direction was oriented 45º from vertical and horizontal orientations. It was decided that directional sensitivity would be disregarded and the encompassing material property data would be used to make the material model. Thus, cortical bone was assigned an elastic modulus of 12.0 GPa, yield stress of 90 MPa, tangent modulus of 2 GPa, and cortical bone element deletion dictated by a 1.50% maximum principal strain. The density of cortical bone was determined from literature and set at 2.0 g/cm^3. Cortical bone material parameters were confirmed with Velodyne simulations to justify their use in the pelvis FE model (Figure 17).

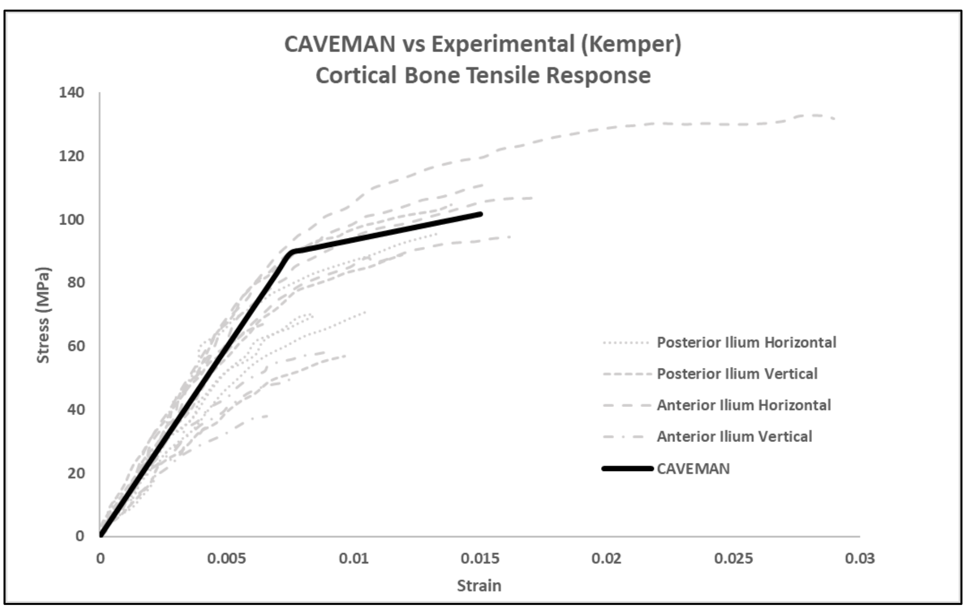

Figure 17. Comparison of the CAVEMAN cortical bone tensile response to the experimental data traces reported in Kemper 2005.

Pelvic cancellous bone is not as well characterized in the literature as cortical bone. Experimentally described material stiffness definitions for pelvic cancellous bone range from 30 MPa (Dalstra et al. 1993) to 375 MPa (Untaroiu et al. 2008). Anderson et al. 2005 reported an empirical equation in which the apparent density of pelvic cancellous bone can be used to estimate an elastic modulus (Equation 3.1.1).

$$E = 2017.3(Papp)^{2.46}$$ ***Equation 3.1.1***

Dalstra et al. 1993 performed compressive non-destructive mechanical testing along with dual-energy quantitative computer tomography in order to obtain the elastic Young's moduli and Poisson's ratios for specimen of pelvic cancellous bone. In this literature the apparent density of pelvic trabecular bone samples was reported as 0.345 g/cm^3 (standard deviation 0.219 g/cm^3). Young's Modulus reported in Dalstra's study ranged from 30-65 MPa. Experimental failure strains were not reported in these experimental tests, however in prior FE modeling papers of the pelvis failure strains for trabecular bone were around 25% (Untaroui et al. 2008 and Kikuchi et al. 2006), while other models did not fail the bone, but simply allowed it to yield (Song et al. 2005).

It was decided based on the literature to assign an elastic modulus of 200 MPa, yield stress of 9.0 MPa, a tangent modulus of 20 MPa, and cancellous bone element deletion activated at 25.0% maximum principal strain. This Young's modulus was determined using Equation 1 with a density of 0.4 g/cm^3. Later as explained in section 3.4.2, the model response was found to be especially sensitive to cancellous bone stiffness. Using inverse-FE analysis the cancellous bone was later adjusted to an elastic modulus of 55 MPa and tangent modulus of 10 MPa, with the other material parameters staying the same. The values of these parameters are more in line with those reported in Dalstra et al. 1993. The finalized cortical and trabecular bone material properties can be viewed in Table 3 at section 3.3.

3.2. Pelvis Connective Regions

Special attention was given to the creation and validation of the connective regions of the pelvis, both the pubic symphysis and sacroiliac joints. Based on the results of the lower extremity sensitivity study it was theorized that the pelvic joints would largely dictate the response and injury predictions of the pelvis model. Subsystem validation cases were used to provide further benchmarking for the response of these joints.

3.2.1. Development and validation of the CAVEMAN pubic symphysis joint

The pubic symphysis is a distinctive joint that connects the anterior portion of the pelvis, joining the left and right hip bones. The joint is comprised of a fibrocartilage disk surrounded by strong ligaments on the anterior, posterior, superior, and inferior sides (Becker 2010). Normal range of motions of the joint total less than 2mm translation and 1 degree of rotation. Biomechanically the joint plays an important role in everyday activities, where it must support compressive (such as when sitting or standing) and tensile (such as in a one leg stance) loading. Differences in the anatomy of male and female joints are well described, especially regarding pregnancy related changes. For the work contained in this thesis the male pubic symphysis will be evaluated. Pubic symphysis joint material properties and corresponding constitutive models have been well defined in the literature.

Prior cadaveric studies have been performed on isolated pubic symphysis in dynamic loading conditions (Dakin 2001). Dakin's experimental data set consisted of 20 specimens, 13 males and 7 females, with an average age of 66 years old. Specimen were separated by sex, and then subjected to a variety of experiments including: preconditioning, tension and compression creep tests, bending tests, and then loaded to failure in both low (0.01 mm/s) and high (100 mm/s) tension tests. Dakin's experiments define both the elastic and viscoelastic mechanical response of the human pubic symphysis joint. In these experiments a clear difference between the response of male and female joints was observed.

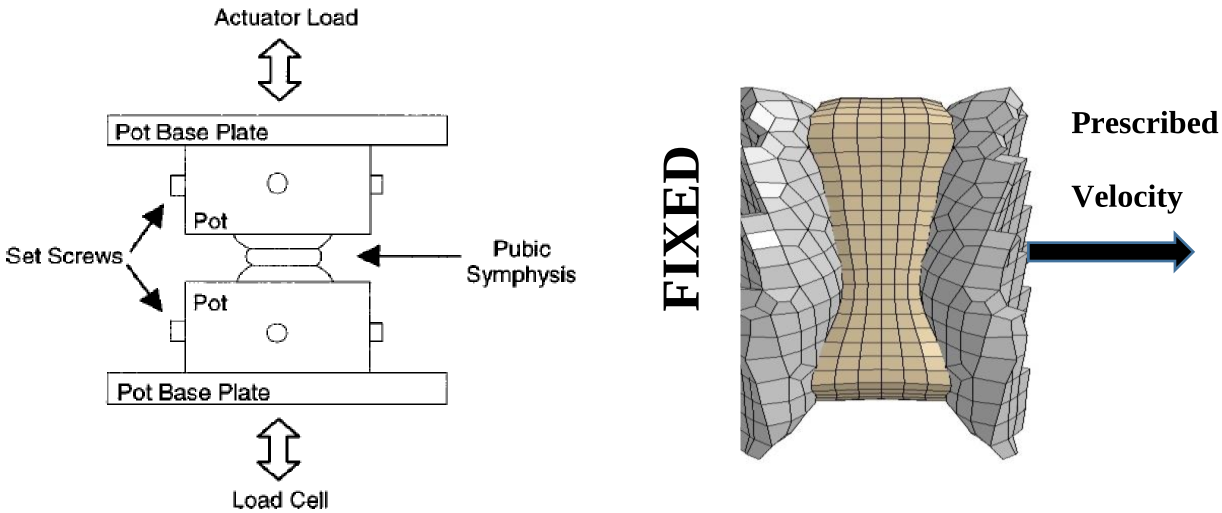

Figure 18. Visual comparison between the experimental setup described in Dakin 2001 and the finite element replication of those tests done in Velodyne on the CAVEMAN pubic symphysis joint (example shown for tension test).

Further work with Dakin's experimental data (Li 2007) formulates constitutive parameters for the application of a three dimensional pubic symphysis finite element model. The CAVEMAN pubic symphysis was validated against the experimental results of Dakin's tests in a similar manner as was done in Li's computational study (Figure 18). The pubic symphysis fibrocartilage disk was modeled as a viscoelastic Mooney-Rivlin material and a two-term Prony series was used to describe the rate dependent nature of the material. For the pubic ligaments a transverse isotropic hyperelastic material model was utilized. Initially the same material properties were used in the CAVEMAN pubic disk and ligaments, but these were optimized slightly from Li's reported FE values to better fit the experimental tests done in Dakin 2001. The constitutive equations and parameters used in the CAVEMAN pubic joint can be viewed in Table 3. One limitation related to Velodyne is that viscoelastic parameters are not currently supported for material type 44, which is the transverse isotropic hyperelastic material model used for the pubic ligaments. However, with slight optimization the force-displacement response of the pubic joint compared favorably to the experimental data corridors for both the high rate (Figure 19) and the quasi-static tension and compression tests (Figure 20).

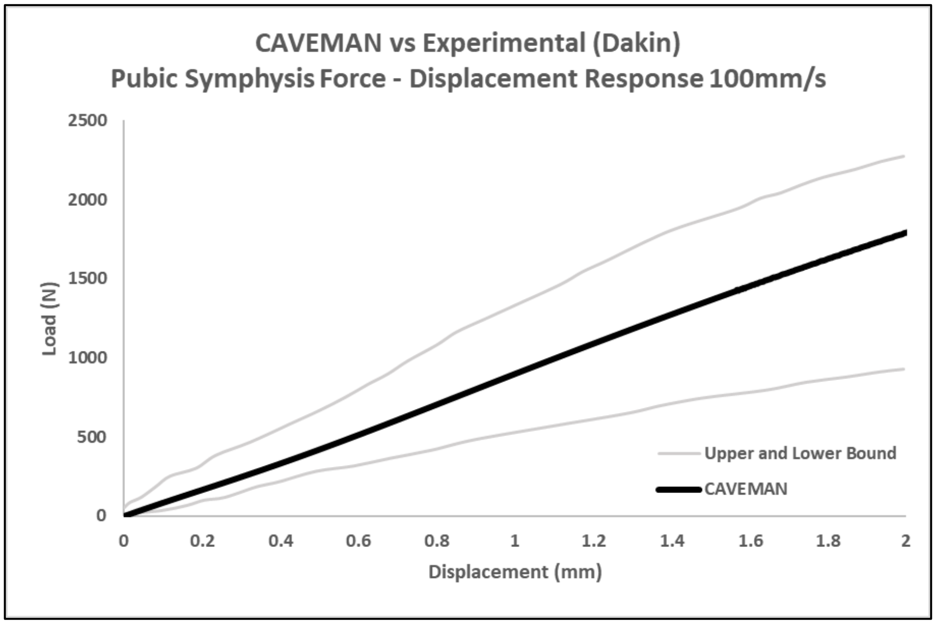

Figure 19. The dynamic load-displacement response of the CAVEMAN isolated pubic symphysis compared to the male experimental corridors reported in Li 2007, experiments from Dakin 2001

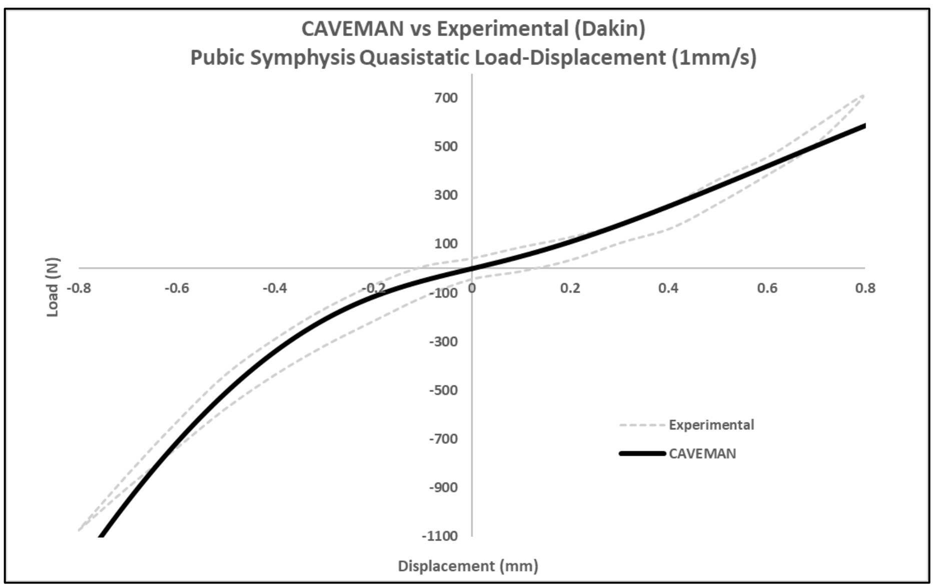

Figure 20. Quasi-static tension and compression load-displacement response of the CAVEMAN isolated pubic symphysis compared to male experimental hysteresis loops from Li 2007, experiments from Dakin 2001. Although the full hysteresis response is not captured in the quasi-static loading, this isn't a concern since our model is being developed for high loading rates.

3.2.2. Development and validation of the CAVEMAN sacroiliac joints

The human sacroiliac joint (SIJ) is a complex joint that connects the coxal bones of the pelvis to the sacrum (Figure 21). Primary functions of these joints are to transmit load from the lower body regions to the spine, with the rest of the pelvis. The SIJ permits relatively little motion around the articular surface. Evaluations of the movement of the SIJ has shown that there are no more than 2-3 degrees of rotation and 2mm of translation of the joint space for in vivo movements (Joukar 2017), while the joint space itself is described as less than 2mm in width. The mobility or lack thereof is dictated by both the tightness of the connective tissues as well as the geometries of the articular surfaces of the joint interface (Vleeming et al. 2012).

An encompassing ligamentous anatomical description as described in Obregt 2013 can be viewed in Figure 21. Hammer et al. 2018 did a computational study looking at the effects of removing the sacrospinous and sacrotuberous ligaments and how this related to joint stabilization, where it was found that these two ligaments being disrupted increased the pelvis motion by up to 70%. However, for the purpose of this study, due to the tissues present in the FE validation case for lateral impact and isolated sacroiliac joint test, only the following ligaments were included in the model: anterior sacroiliac, posterior sacroiliac, and interosseous ligament. These ligaments are the primary connective tissues enclosing the articular joint space between the ilium and sacrum. The posterior and interosseous ligaments are commonly described as being stronger than the thinner anterior SIJ ligaments and contribute the most to the stability of the SIJ (Hammer 2013). The cartilaginous and articular surfaces of the SIJ are described as having more of a hyaline cartilage on the coxal side and fibrocartilage description on the sacral side. A diagram and cadaver view of the joint interfaces can be viewed in Figure 22.

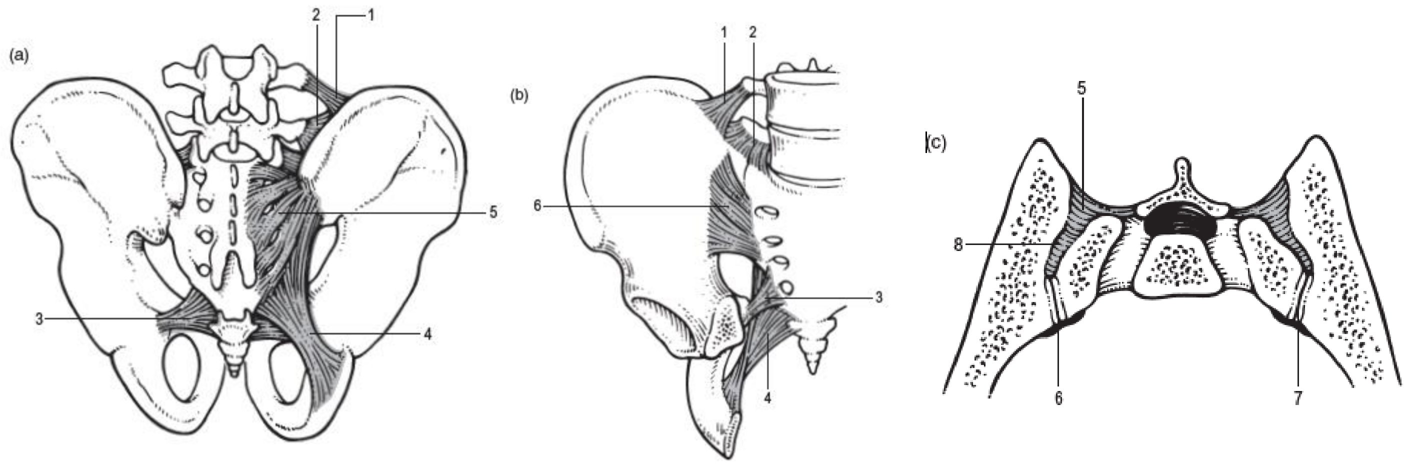

Figure 21. Anatomical descriptions of the human sacroiliac joint ligaments from Ombregt 2013. (a and b and c) 1,2 iliolumbar ligaments; 3, sacrospinous ligament; 4, sacrotuberous ligaments; 5, posterior sacroiliac ligaments; 6, anterior sacroiliac ligaments;(c) 7, articular surface; 8, interosseous ligament.

The sacroiliac joints are described as being one of the most common chronic pain generators in those involving the lower back (Tilvawala et al. 2018). SIJ injuries lead to an unstable pelvis and improper joint mechanics. The majority of research involving these joints is thus related to orthopedics and clinical patient related treatments. Hammer and Kilma (2019) have published a recent review article highlighting the work done in the field of pelvic computational models with a particular focus on sacroiliac joint research. These pelvis FE models are suited toward a variety of purposes including evaluation of surgical SIJ fixations, the influence of soft tissues in pelvic motion, and non-surgical diagnostic treatments of the joint.

Many of the published pelvis FE models use linear elastic or significantly simplified material properties as well as simplified geometries. Very few of the reviewed FE models involve any parametric analysis and even fewer consider injurious biomechanics related FE simulations. Hammer and Kilma identified just seven publications that performed parametric analysis on their pelvic models and sacroiliac joints, thus it is important to include a parametric study on the SIJ in this study in order to gain insight into the SIJ structure’s role in side impact.

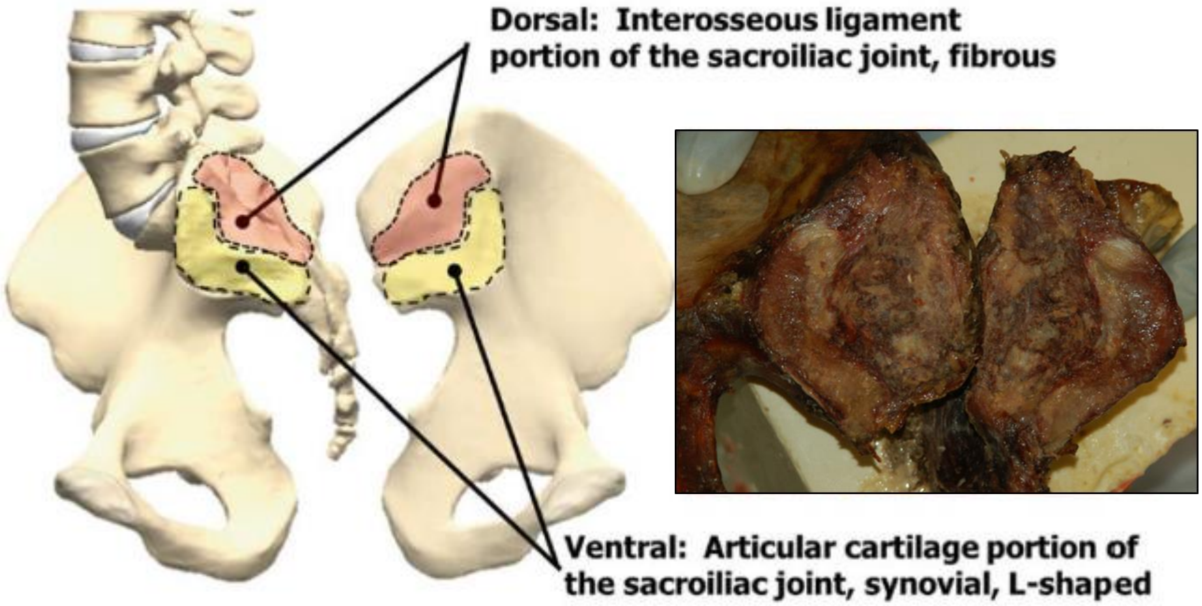

Figure 22. Open book view of the articular surfaces of the SIJ on both the ilium and sacrum. Diagram from Dall et al. 2015, PMHS image from UVA CAB Salzar lateral impact test series.

Another issue highlighted in Hammer and Kilma's review article is that the majority of computational studies of the human pelvis are validating themselves based solely on literature of prior published models. Other pelvic FE models validate their sacroiliac joints with one of the two cadaveric studies (Miller at al. 1987; Simonian et al. 1993) that make an effort to define the quasi-static load-displacement behavior of the sacroiliac joints. Thus it is desirable to evaluate the performance of the SIJ in a different loading condition as will be done in the following chapter. None of these prior pelvic FE model have evaluated their sacroiliac joint representations with injurious, higher rate loading conditions. Many of the prior models (Eichenseer et al. 2011, Lindsay et al. 2015) use 1-D elements to represent the ligamentous structures of the SIJ. To go along with the modeling methods of the CAVEMAN human body model, it is important to represent these connective tissues in an accurate 3-D manner, particularly the extensive interosseous ligament. This allows more biofidelic response for future soft tissue failure characterizations.

Steinke et al. (2010) provided insight into the three dimensional geometry of the sacroiliac joint ligaments. The average ligament geometric measurements and their standard deviations from 13 male pelvic cadavers were recorded. This was achieved by cutting the SIJ horizontally into 5 mm slices, for each joint 14-23 slices were extracted. Steinke's paper did not consider the other ligamentous structures commonly lumped into descriptions of the SIJ, only considering anterior, posterior, and interosseous ligaments. Joint dimensions were described using parallelepipeds assigned to the cranial, middle, and caudal parts of each ligament. Of these analyses, the key findings were: the interosseous ligamentous regions are the most extensive (Figure 23), there are obvious differences between the geometries of male and females, and the shape and size of the SIJ surfaces and ligaments vary extensively person to person.

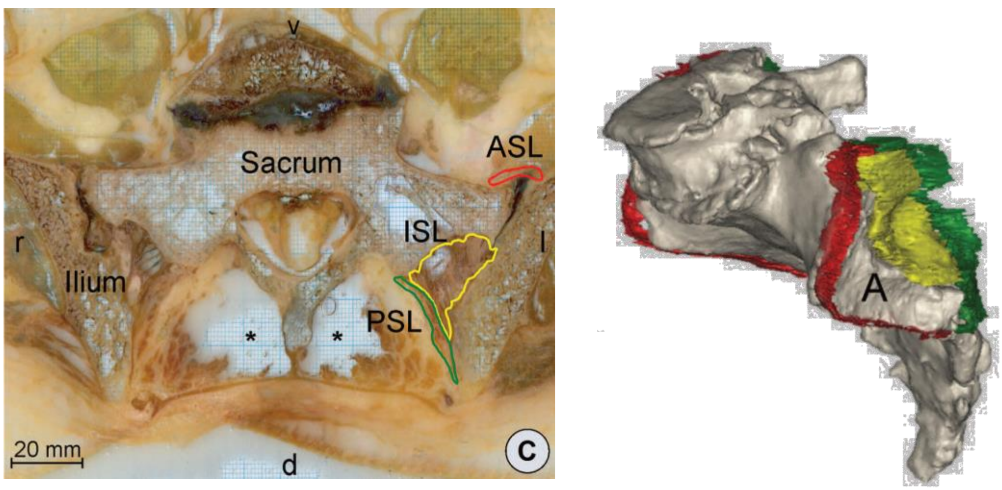

Figure 23. Transverse plane view of the sacroiliac joints in the pelvis, along with the described digital reconstructions of the geometries of the sacroiliac joint and its ligamentous structure described in Steinke, 2011.

In the CAVEMAN model, provided by Zygote was the surface geometry of the anterior and posterior sacroiliac joint ligaments, but not the 3-D descriptions nor the interosseous ligament in any form. First the interosseous ligament geometry of the CAVEMAN model was created by doing a void space fill in SolidWorks of the gap between the ilium and sacrum. The void fill was then sectioned in order to fit the measurements reported in Steinke. This interosseous region was then meshed using Bolt and its geometric measurements were compared to those made in Steinke (Figure 24). This created interosseous ligament was within 1 S.D. of all the reported measurements made in Steinke 2011.

Interosseous Ligament - Geometric Measurement Comparison			
Region	**Steinke - Measurements (mm)**	**SD**	**CAVEMAN - Measurements (mm)**
[-1]	**Length**		**Length**
	10.1	2.9	8.92
	Width		**Width**
	23.5	4.1	19.2
[0]	**Length**		**Length**
	7.9	2	7.1
	Width		**Width**
	26.2	5.1	19.2
[1]	**Length**		**Length**
	7.2	2	5.7
	Width		**Width**
	21.1	5.9	19.3
Total	**Height**		**Height**
	32.1	8	29.7

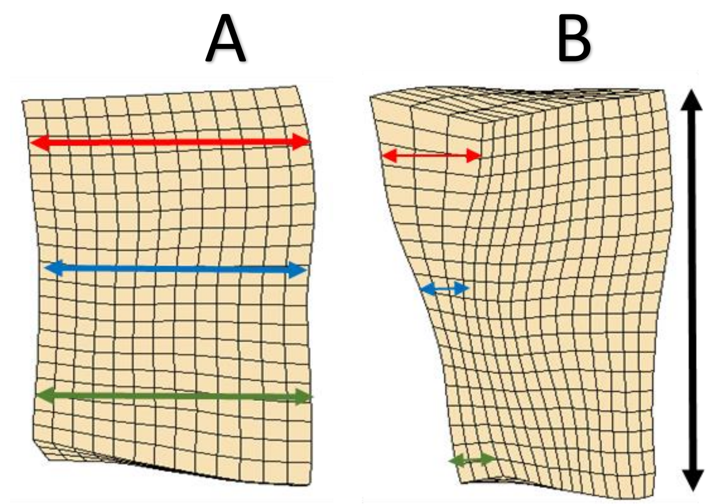

Figure 24. Lateral (A. widths) and posterior (B. lengths and height) views of the CAVEMAN interosseous ligament with a geometric measurement comparison to the anatomical data reported in Steinke, 2011.

It was desired to continue utilizing the CAD provided by Zygote, thus the surface geometries of the anterior and posterior SIJ ligaments were utilized. Based on the described thickness and coverage areas reported in Steinke 2011, a 3-D geometry of the anterior and posterior ligaments was created. The geometries created from the Zygote surfaces matched well in 2/3 of each of the dimensions for anterior, posterior, and medial measurements. The major discrepancy coming from the side to side lengths of the ligaments, particularly the anterior side. This geometric issue can be viewed in Figure 25 and in Appendix D. In order to compensate for this, the thickness of the SIJ ligaments were adjusted so that a match of the reported coverage areas could be achieved. Since the soft tissues here expected to contribute significantly to model response getting accurate coverage areas was deemed crucial.

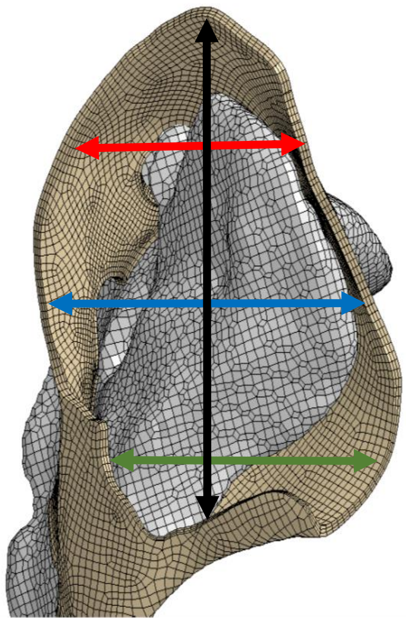

SIJ Ligamentous Structure- Geometric Measurement Comparison			
Region	Steinke - Measurements (mm)	SD	CAVEMAN - Measurements (mm)
[-1]	Width		Width
	52.3	7.5	52.2
[0]	Width		Width
	69.1	5.1	69.4
[1]	Width		Width
	50.2	11	55.4
Total	Height		Height
	56.3	8.5	89.2

Figure 25. Lateral (widths and height) view of the CAVEMAN sacroiliac joint ligament structure with a geometric measurement comparison to the anatomical data reported in Steinke, 2011.

The primary geometry validation goal of CAVEMAN confirming the coverage areas of the SIJ connective tissues was accomplished (Table 2). This was done by first creating the geometry of the interosseous ligament from the void fill between the sacrum and ilium and sectioning it to fit within one standard deviation of Steinke's anatomical data. Next the anterior and posterior SIJ ligament geometry provided by Zygote was compared to Steinke. The lengths and height of the anterior-posterior SIJ complex were significantly greater than that reported in Steinke. In order to compensate for this and continue using the Zygote geometry the width of the anterior and posterior SIJ ligaments was set to 1.5 mm, about 0.5 mm less than the lower bounds of the anatomical data. Since the coverage areas were within 1 standard deviation of those reported in literature they were considered validated.

Table 2. Regional ligament attachment areas of the CAVEMAN SIJ compared to Steinke 2011.

Interosseous Ligament - Geometric Measurement Comparison		
Steinke - Measurements	SD	**CAVEMAN - Measurements**
Avg. Attachment Area mm^2	x	Attachment Area (Sacrum) mm2
754	229	514
		Attachment Area (Ilium) mm^2
		583
SIJ Ligaments - Geometric Measurement Comparison		
Steinke - Measurements	SD	**CAVEMAN - Measurements**
Avg. Attachment Area mm^2	x	Attachment Area (Sacrum) mm2
302	110	284
		Attachment Area (Ilium) mm^2
		383

The mechanical properties of the sacroiliac joint ligaments are not well defined in literature. Many of the existing FE models that attempt to model these connective tissues simply reference prior FE models which are built off of Miller et al. 1987 and Simonian et al. 1993, since there are few widely available studies in the literature that experimentally define these mechanical properties. Eichenseer et al. (2011) validated their SIJ ligament material properties by fitting them to Miller's cadaveric tests. These ligaments were represented with tensile beam elements given a piecewise linear material model with higher stiffness at increased strain levels. Stiffness properties in N/mm were reported where that the interosseous ligament was significantly stiffer at (500 N/mm) than the anterior and posterior ligaments (50-100N/mm). Lindsey et al. (2015) reported ligament properties in terms of Young's modulus at varying level of strains. Their model gives maximum strain moduli of the interosseous, anterior, and posterior ligaments as 102, 316, and 380 MPa respectively. Hammer et al. (2013) performed a computational study of the pelvic ligaments on joint stability using anatomical data for ligament geometries. The material properties they used in this model to represent the sacroiliac joint ligaments were from testing of the iliotibial tract (Steinke 2012), where stiffness values of an average of 400 MPa were reported. In this study, it was determined that the ASL, PSL, and most especially the ISL, all played the biggest factors in the stability of the sacroiliac joint. Due to the lack of characterization of the sacroiliac joint ligaments, a plausible starting point was assumed to be the human hip joint mechanical characterizations available in literature. Hewitt et al. 2001 performed tensile tests on hip joint capsule ligaments where modulus of elasticity at 80% of the failure strain ranged from 76 to 285 MPa, which was plausible for connective tissues.

The above studies were used to create baseline stiffness for the SIJ ligaments in the CAVEMAN model; which in turn would be optimized in simulations of the Miller et al. 1987 tests. Miller et al. 1987 performed experiments on fresh frozen isolated sacroiliac joints in order to characterized the load-displacement behavior of single and paired cadaveric specimen. The cadavers in this test series consisted of seven males and one female, aged 59-74 years with an average age of 66 years. The author points out that all joints were CT scanned prior to testing to check for ankyloses and that one specimen was not tested for this reason. Static loads of 294 N were applied to the center of the sacrum to paired sacroiliac joints in the anterior, posterior, superior, inferior, and lateral directions while displacement of the center of the sacrum was measured 1 minute after the load application. This procedure was repeated on a single SIJ following the release of one of the ilium. Miller's tests included just the anterior, posterior, and interosseous ligaments and thus was chosen for a validation case.

The CAVEMAN SIJ model was validated against Miller's tests. The node to be tracked as center of the CAVEMAN sacrum was chosen to fit within one standard deviation of the sacrum center measurements reported in Miller (Figure 26). Loads were applied to this center point in the superior, posterior, anterior, inferior, and mediolateral directions in a similar manner to the experimental data set. The best fits that were reached are reported compared to the experimental averages in Figure 27. The fits achieved to Miller's tests are comparable to both Kim et al. 2014 and Eichenseer et al. 2011 model validations which seemed to be significantly laxer in the mediolateral direction. This is likely due to the simplification of using beam elements to represent ligamentous structures. Overall the force-displacement response of the FE pelvis SIJ structure was within 1 standard deviation for each loading direction, except for the anterior direction. Despite repeated attempts at optimization it was not possible to get all five responses within 1 standard deviation of the respective loading directions. However, this is not expected to drastically dictate the FE pelvis response in injurious high rate loading. Since these were quasi-static and relatively non severe loads (294N) the response of the SIJ in these loading conditions is not of the utmost concern. This validation case is used due to the limited availability of any other SIJ related mechanical test data and to hone in on material parameters that can be used to define the SIJ ligaments. In later model sensitivity studies performed in this thesis, drastic variations made to the stiffness of the SIJ ligaments did not seem to effect injury outcomes or force distribution for the pelvis. This conclusion may not be valid in other injurious loading modes (particularly vertical accelerative loading) so any future mechanical characterization of the SIJ-Pelvis structure in high rate loading would be valuable. The final transverse isotropic hyper elastic material parameters determined from this study are reported in Table 3 Section 3.1.5.

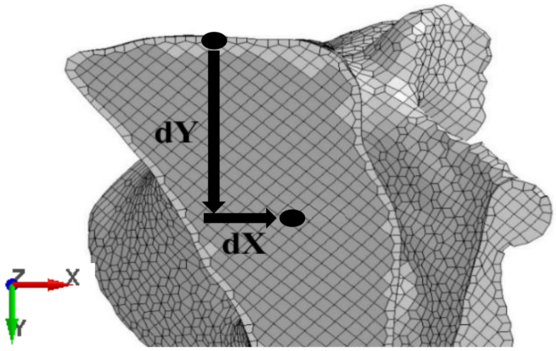

Center of the Sacrum Described in Miller 1987 vs CAVEMAN Distance from Sacral Endplate	
dX (Posterior Direction)	dY (Inferior Direction)
Miller's Average (mm)	Miller's Average (mm)
11.50 (9.40)	29.00 (4.10)
CAVEMAN (mm)	CAVEMAN (mm)
15.61	27.00

Figure 26. Center of sacrum as described in Miller 1987.

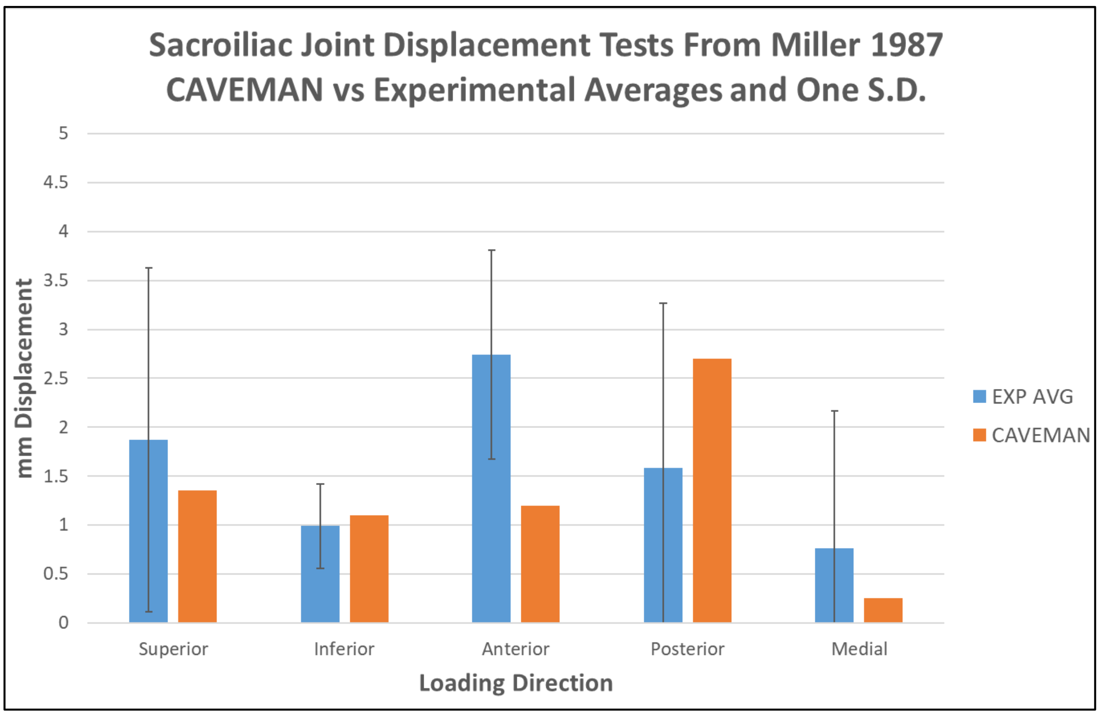

Figure 27. Finite element results compared to Miller's SI joint displacement tests. The anterior direction was the only response not fit within 1 SD of the experimental averages. It is not expected this discrepency will greatly effect the total model repsonse since it is a limited quasi-static loading case.

3.3. FE Pelvis Development Summary

Pelvis bone geometry was reconstructed from scans of a 50th percentile male, while connective tissue geometries were created to corroborate with reported coverage areas of pelvic ligaments in literature. A high-fidelity mesh was applied to the pelvis geometry, meeting the mesh

Table 3. Summary of CAVEMAN Pelvis constitutive equations and material parameters.

CAVEMAN DEFLESHED PELVIS CONSTITUTIVE MODELS AND PARAMETERS			
Material Model	**Formulation**	**Tissue Type**	**Coefficients**
Elastic-Plastic	$\boldsymbol{\sigma} = E\varepsilon, \quad \Vert\boldsymbol{\sigma}\Vert \leq \boldsymbol{\sigma}_0$ $\boldsymbol{\sigma}_y = \boldsymbol{\sigma}_0 + \frac{EE_T}{E - E_T}\bar{\boldsymbol{\varepsilon}}^p \quad \Vert\boldsymbol{\sigma}\Vert > \boldsymbol{\sigma}_0$	Pelvic Cortical Bone	$\rho = 2.0\frac{g}{cm^3}$; $\boldsymbol{\sigma}_0 = 90\ MPa$, $E_T = 2.0\ GPa$; $E = 12.0\ GPa$, $\nu = 0.3$
		Pelvic Cancellous Bone	$\rho = 0.4\frac{g}{cm^3}$; $\boldsymbol{\sigma}_0 = 9.0\ MPa$, $E_T = 10\ MPa$; $E = 55\ MPa$, $\nu = 0.2$
		Sacrum Cortical Bone	$\rho = 2.0\frac{g}{cm^3}$; $\boldsymbol{\sigma}_0 = 80\ MPa$, $E_T = 2.0\ GPa$; $E = 11.2\ GPa$, $\nu = 0.3$
		Sacrum Cancellous Bone	$\rho = 0.4\frac{g}{cm^3}$; $\boldsymbol{\sigma}_0 = 9.0\ MPa$, $E_T = 10\ MPa$; $E = 55\ MPa$, $\nu = 0.2$
Transversely Isotropic Hyperelastic	$\boldsymbol{\sigma} = \boldsymbol{\sigma}_{hyper}$ $\boldsymbol{\sigma}_{hyper} = \frac{1}{J}\boldsymbol{F}\left\{\frac{\partial W}{\partial \boldsymbol{E}}\left(\boldsymbol{E}(\tau)\right)\right\}\boldsymbol{F}^T$ $W_{Mat44} = C_1(\tilde{I}_1 - 3) + C_2(\tilde{I}_2 - 3) + F(\lambda) + \frac{K}{2}(\ln J)^2$	Interrosseous Ligament	$\rho = 1\frac{g}{cm^3}$, $K = 0.7\ GPa$; $C_1 = 4.0\ MPa$, $C_2 = 0.0$, $C_3 = 0.5\ MPa$, $C_4 = 37.5$, $C_5 = 312.0\ MPa$; $\lambda^* = 1.075$
		Posterior SIJ Ligament	$\rho = 1\frac{g}{cm^3}$, $K = 0.7\ GPa$; $C_1 = 3.4\ MPa$, $C_2 = 0.0$, $C_3 = 0.45\ MPa$, $C_4 = 37.0$, $C_5 = 267.0\ MPa$; $\lambda^* = 1.075$
		Anterior SIJ Ligament	$\rho = 1\frac{g}{cm^3}$, $K = 0.7\ GPa$; $C_1 = 3.8\ MPa$, $C_2 = 0.0$, $C_3 = 0.35\ MPa$, $C_4 = 40.5$, $C_5 = 295.0\ MPa$; $\lambda^* = 1.075$
		Pubic Ligament	$\rho = 1\frac{g}{cm^3}$, $K = 0.8\ GPa$; $C_1 = 5.8\ MPa$, $C_2 = 0.0$, $C_3 = 0.95\ MPa$, $C_4 = 41.0$, $C_5 = 371.0\ MPa$; $\lambda^* = 1.055$
Ogden Viscoelastic	$\boldsymbol{\sigma} = \boldsymbol{\sigma}_{hyper} + \boldsymbol{\sigma}_{visco}$ $\boldsymbol{\sigma}_{hyper} = \frac{1}{J}\boldsymbol{F}\left\{\frac{\partial W}{\partial \boldsymbol{E}}\left(\boldsymbol{E}(\tau)\right)\right\}\boldsymbol{F}^T$ $\sigma_{visco} = \frac{1}{J}F\left\{\int_0^t [A_1 + A_2(I_2 - 3)]\left[\sum_{i=1}^{6} G_i e^{-(t-\tau)/T_i}\right]\dot{E}(\tau)d\tau\right\}F^T$ $W_{Ogden} = \sum_{m=1}^{n}\left\{\frac{\mu_m}{\alpha_m}\left[J^{-\alpha_m/3}\left(\lambda_1^{\alpha_m} + \lambda_2^{\alpha_m} + \lambda_3^{\alpha_m} - 3\right)\right]\right\} + \frac{K}{2}(J-1)^2$	Pubic Symphysis Disc	$T_1 = 1.85185\ s$, $T_2 = 16.6666\ s$; $G_1 = 16.00\ kPa$, $G_2 = 540.00\ kPa$; $A_1 = 1.000$, $A_2 = 0.0$ $\mu_1 = 100.0\ kPa$, $\mu_2 = -400.\ kPa$; $\alpha_1 = 2$, $\alpha_2 = -2$; $K = 49.83\ MPa$
Mooney Rivlin	$W = C_1(I_1 - 3) + C_2(I_2 - 3)$	Cartilage	$\rho = 1\ \frac{g}{cm^3}$; $C_1 = 2.87\ MPa$, $C_2 = 0.278\ MPa$; $\nu = 0.495$

quality standards that were previously defined for the lower extremity model. Constitutive models and material properties were assigned through mechanical characterization available in literature and through FE optimization. As an example of optimization, the stiffness of pelvis trabecular bone was not well described in previous studies so it was adjusted to fit experimental test results while staying within the bounds of the literature as explained in Section 4.3.1. Further optimization was performed to define the material stiffness of the SIJ ligaments, based on force-displacement experimental test results on isolated SIJ complexes. Individual experimental test cases were used to validate both the SIJ and pubic symphysis, although SIJ response described in the literature was limited. Table 3 summarizes the constitutive models and corresponding material parameters utilized in the defleshed pelvis FE model. A total of four different types of constitutive models were employed to model 10 different tissue types.

Validation is necessary to evaluate the performance of these various tissue geometries and material properties when they are combined to represent the human pelvis. If this defleshed pelvis model response and injury prediction can be benchmarked to experimental tests, a certain level of confidence can be given to the pelvis model. To perform this model validation, experimental tests on defleshed pelvises at the University of Virginia (UVA) were reconstructed in an FE environment and the pelvis model was assessed.

CHAPTER 4: BENCHMARKING THE CAVEMAN PELVIS MODEL

This chapter covers the corroboration and benchmarking performed in order to provide validation to responses and injury predictions of the CAVEMAN pelvis model. In the prior chapter, the pelvis model was validated on a tissue and joint-structure level, however, it is necessary to evaluate the combined pelvis subsystem. Recreating controlled laboratory tests on PMHS tissues and evaluating the model response in those conditions will give a certain level of confidence in this pelvis model. These validation efforts will compare the model force transmissions and injury prediction to the experimental dataset PMHS responses.

4.1. PMHS Data Set

Cadaveric PMHS tests were performed at UVA. Salzar et al. 2011 performed a cadaveric lateral impact study at UVA on 16 cadaver pelvis. This study was funded by an automotive manufacturer and thus the test boundary conditions were constructed to simulate a lateral automobile impact, with high-rate door panel intrusion into the pelvis.

4.1.1. UVA test setup

As has been elaborated prior (Chapter 1: Section 1), lateral impacts to the pelvis pose a significant injury risk, particularly during military lateral loading blast events. Soft tissues were removed from these male pelvis specimen, the only connective tissues preserved were as follows: the anterior and posterior sacroiliac ligaments, superior and inferior pubic ligaments, interpubic fibrocartilage, and the cartilage of the sacroiliac joint and acetabulum. The age of the cadaver specimens in this test series ranged from 39-76 years with an average age of 59.75 (10.5) years. The average body mass of the cadavers was 72 kg, average height 175 cm, and average BMD 152 +- 24 mg/cc. The pelvic structure was potted in a plasticine fast urethane Fast Cast to hold the left coxal bone, and center left sacrum (Figure 28). The left ilium of each pelvis was then cut to allow for the measurement of separate load paths through the sacrum and pubic symphysis. Understanding the load distribution through the pelvis furthers the understanding of injury mechanisms which in turn can lead to improvements in safety.

The pelvis specimens were then impacted at either the acetabulum to simulate an impact to the femoral head or at the iliac wing. The testing apparatus consisted of a drop tower assembly with a transfer beam to attenuate the severity of the impact and limit the stroke of the impactor to a repeatable distance. Data was collected using a TRAQ-P data acquisition system with a 10 kHz sampling rate, which included readings from the anterior, posterior, and impactor load cells while acoustic crack detection was sampled at 5 MHz to identify fracture timings (Salzar et al. 2009). Salzar's impacts consisted of 2 quasi-static acetabulum impacts, 2 quasi-static iliac wing impacts, 6 dynamic acetabulum impacts, and 6 dynamic iliac wing impacts. Each pelvis failed in testing and was there only tested once. The high-rate impact condition was described to be similar to a 40 km/hr automotive impact. The experimental setup of Salzar's tests are further elaborated on in the following sections.

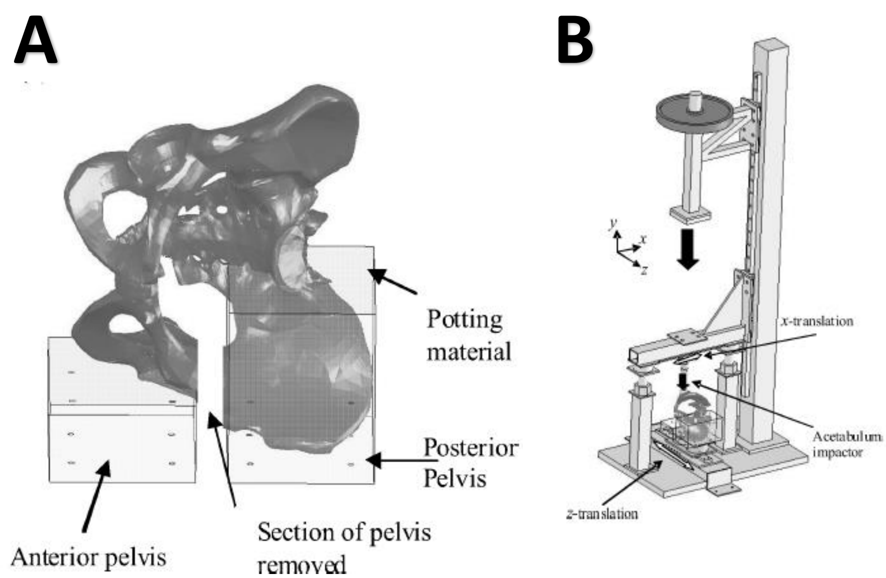

Figure 28. (A) Potted pelvis from the Salzar test series, notice the section of left coxal bone removed in order to measure the force transmission through the pubic and sacroiliac joints. (B) Testing apparatus used in Salzar et al. 2009.

4.1.2. Reconstructing experimental setup of UVA lateral pelvis impact tests

The testing apparatus for the UVA cadaveric study was meshed using CUBIT meshing software developed by Sandia National Laboratories. The potting for the pelvis was created by taking the reference pelvic geometry and creating a mold of it form a reference block of material in SolidWorks. The potting had complex interior geometry so it was meshed in Bolt. The material of this potting was defined with a stiff linear elastic material with a Young’s modulus of 300 MPa to attempt to replicate the material properties fast setting urethane casting resin that was used for the potting during the experiments. Elements in the left ilium were deleted so that the anterior and posterior load share could be measured separately as was done in the experiments. The anterior and posterior load cells were added to the potting beneath each portion of the separated left ilium in order to measure the forces traveling through the pelvis in each impact. The meshed CAVEMAN pelvis and acetabulum impact experimental setup can be viewed in Figure 29.

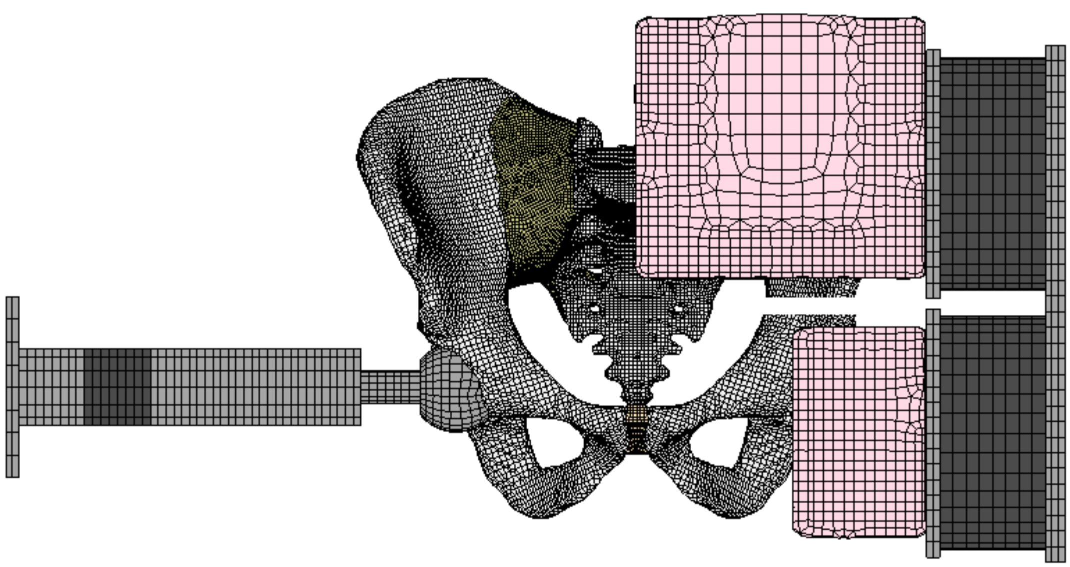

Figure 29. Finite element mesh for the acetabulum impact condition. The apparatus was meshed in Cubit, while the potting was created in Bolt.

Boundary conditions were recreated to match the testing conditions in Salzar et al. 2009. The impactor was allowed to translate freely in the x axis (superior/inferior direction), while the potted reaction fixture was free to translate in the z axis (anterior/posterior direction). These types of orthogonally oriented boundary conditions were used in the experiment to limit artificial constraining of the pelvis as well as to limit off-axis loading. Figure 30 illustrates these boundary conditions for each impact recreated in FE.

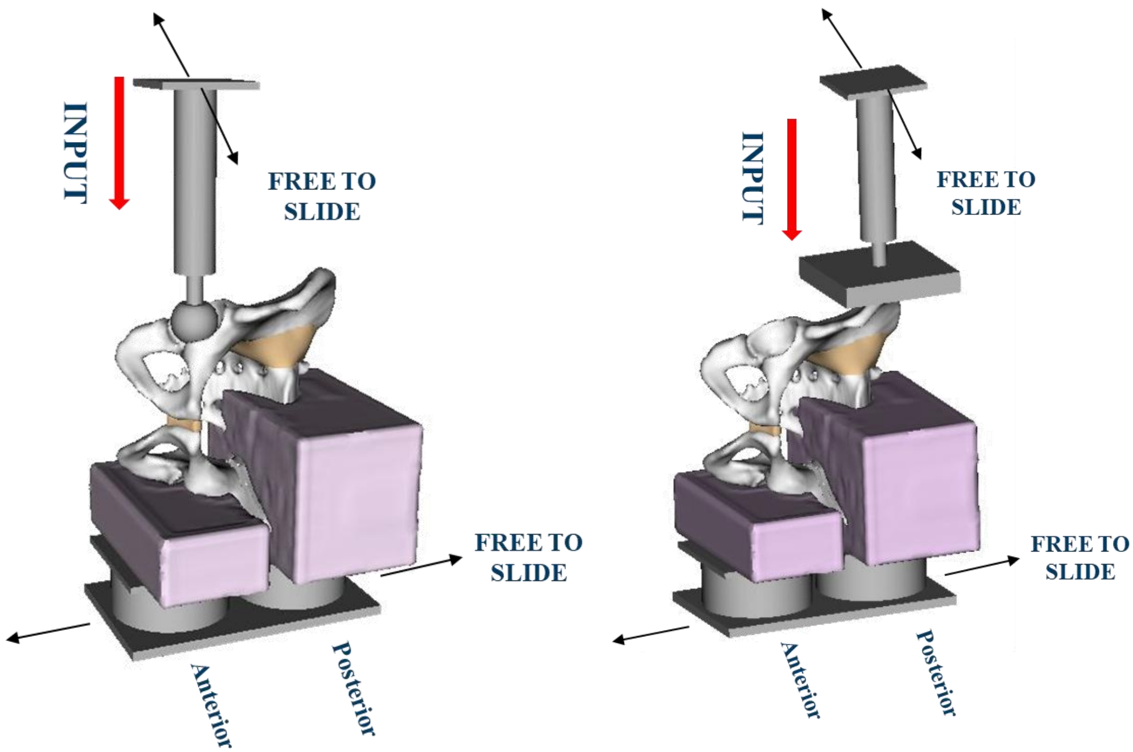

Figure 30. Description of boundary conditions for each of the impact conditions. Acetabulum impact (left) and iliac wing impact (right).

Salzar describes CF-45 Confor Foam (EAR Specialty Composites, Indianapolis) as being used to cover the iliac wing impactor. FE tests were done to measure the effect of different foams on the model response. The response was not sensitive to changes between different types of soft foam material descriptions, thus a soft material foam in Corvid's material database was chosen.

Post-processing of the Salzar data included measuring the vertical displacement of the impactor plate or sphere over time with high speed motion tracking video. A representative time-displacement was chosen from both the iliac and acetabulum impacts and then the derivative of these curves were taken in MATLAB to create representative velocity profiles (Figure 31). The peak input velocity for the acetabulum and iliac wing impacts was determined to be 4.33 and 3.23 m/s, respectively. Using this input boundary conditions, the drop tower impactor and transfer beam did not have to be modeled. A prescribed velocity at each point in time was given to a set of nodes on the top of the impactor structure creating the motion causing the impact event. Since the motion of the impactor itself was being prescribed, the mass of the impactor did not play a role in the response for these simulations.

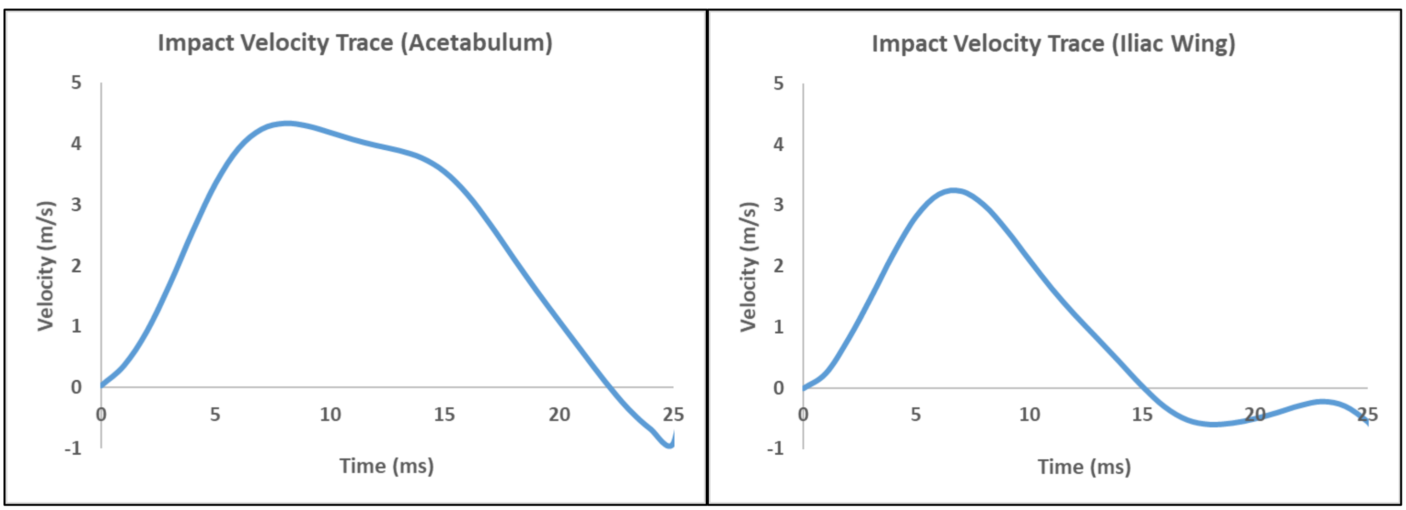

Figure 31. Impactor velocity traces derived from time-displacement data from Salzar et al. 2011. These were used to describe the velocity of the impactor at each point in time during the FE simulation.

4.2. Defleshed Pelvis Force Response and Injury Prediction

Reproducing the outcomes measured by experimental testing is a critical validation step in the development of a human body FE model. This section will explain the performance of the pelvis model in the Salzar-UVA impact conditions. Force response was plotted with experimental traces and a PMHS-conscious CORA analysis was performed. Qualitative comparisons between the injury outcomes from the PMHS and the FE model were also performed.

4.2.1. Pelvis model force responses in UVA lateral pelvis testing configuration

The defleshed pelvis model was impacted in the two loading cases from the Salzar's tests. Simulations were run out to 20 milliseconds which took approximately 3 hours of real time. Injuries were extensive in the acetabulum impact and less severe in the iliac wing impact. See section 3.3.3 for further descriptions of injury. A step-by-step view of the acetabulum case is available in Figure 32 and the force response curves for that impact are presented in Figure 33. When looking at the anterior compression force for the acetabulum impact, there are two prominent peaks: The initial peak occurs around 5.0 ms just before the pubic ramis fractures, then the second peak occurs leading to the ischium fracture around 7.0 ms. At that time, the anterior portion of the pelvis becomes completely disengaged from transferring load through the pelvis. The peak force in the posterior portion of the pelvis occurs roughly at 5.5 ms when the sacrum begins to fail in bending toward the path of the impactor. Based on the force traces, the failure and disengagement of the sacrum appears to progress more slowly than the experimental results, which could stem from limitations in modeling compressive type fractures that occur in the anterior pelvis. The loading rates of the anterior and posterior pelvis model appears to be less than that of the average experimental trace, but the overall response compares well to the acetabulum impact data.

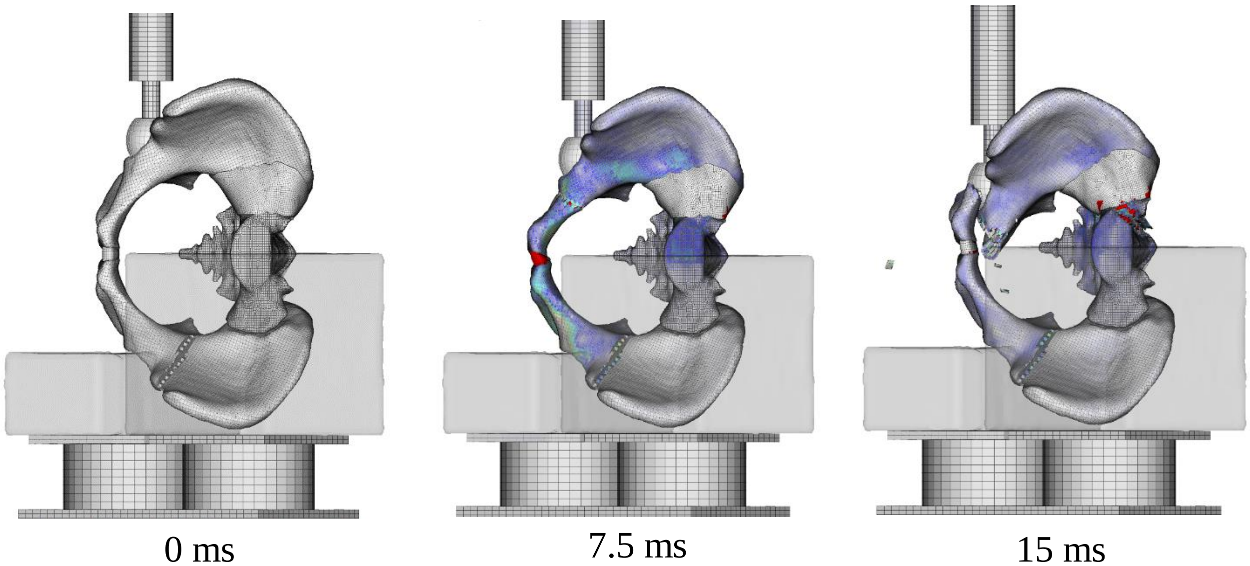

Figure 32. Images of the acetabulum impact, from 0, 7.5, and 15 ms in simulation time. Fractures first begin in the pubic ramis then to the ischium, and then later in time tensile fractures of the sacrum appear. This can be seen step by step where the sacrum begins to rotate towards the loading direction.

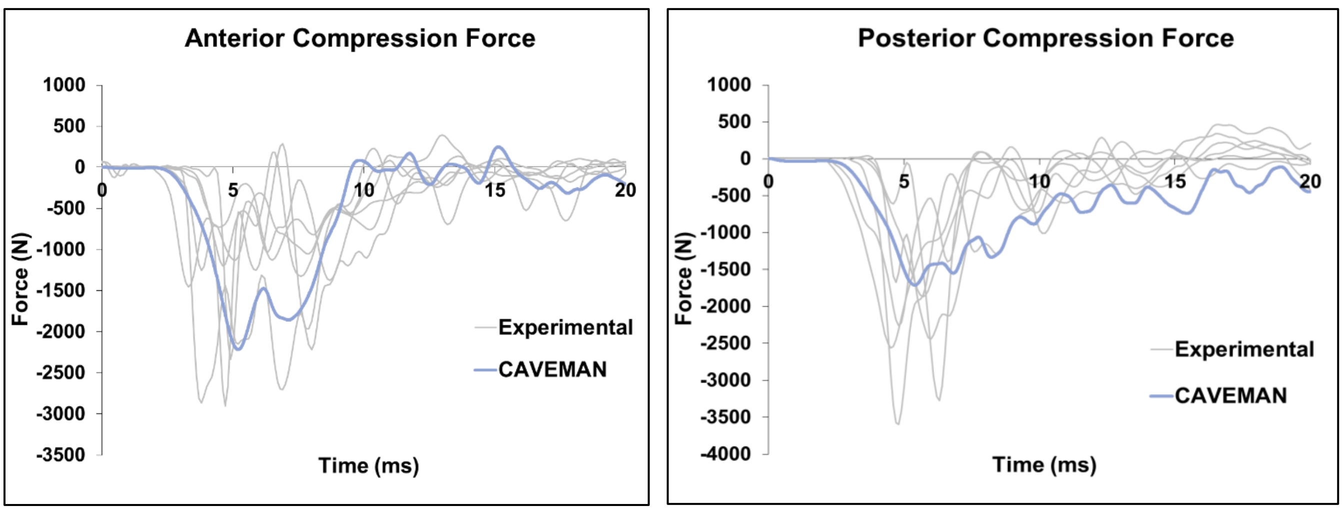

Figure 33. Anterior and posterior load cell readings from the acetabulum impact, compared to experimental traces from each of Salzar's test (6 experimental traces). Peak anterior force is 2224 N at 5.17 ms, Peak posterior force is 1710 N at 5.47 ms.

See Figure 34 and Figure 35 for the results of the iliac impact. The model response compares favorably to these experimental traces, where very little force travels through the anterior side of the pelvis and a significant peak force of 3110 N occurs at 8 ms. Around this time, the sacrum, which is in compression, begins to disengage force transmission. Similar to the acetabulum impact, the loading rates are less in the pelvis model than in the experimental traces.

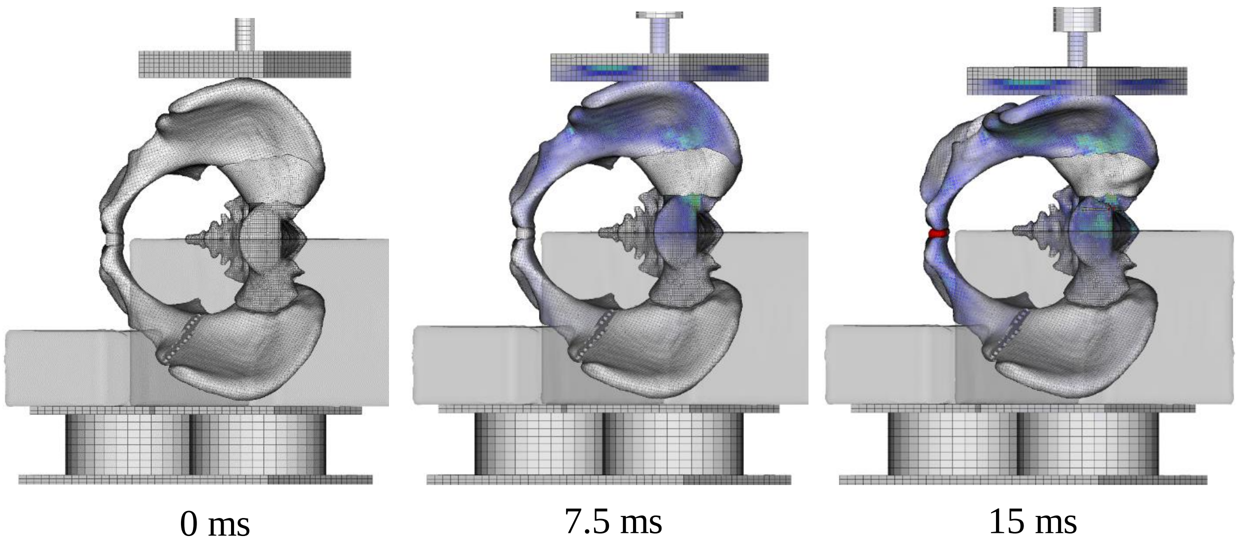

Figure 34. Images of the iliac wing impact, from 0, 7.5, and 15 ms in simulation time. Fractures are solely in the sacrum at the joint interface region. Generally, this impact is less severe from an injury standpoint than the acetabulum impact.

The dynamic peak force distribution of the pelvis FE model compared favorably to what was observed in the data set. For both impacts the distributions were within 1 standard deviation

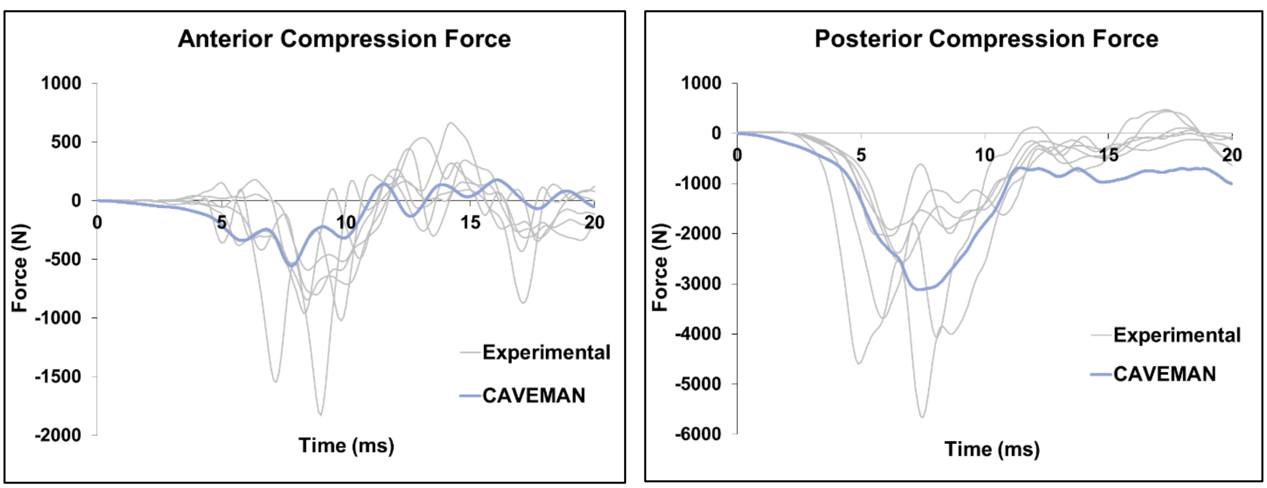

Figure 35. Anterior and posterior load cell readings from the iliac wing impact, compared to experimental traces from each of Salzar's test (6 experimental traces). Peak anterior force is 554 N occurring at 8.54 ms, Peak posterior force is 3110 N occurring at 8 m

(SD) which is especially important for the iliac wing impact considering the SD of that case is just 6%. For the acetabulum impact condition, 56% of force was going through the anterior pelvis at the first peak. However, in the iliac wing impact the vast majority of load travelled through the posterior pelvis at 92%.

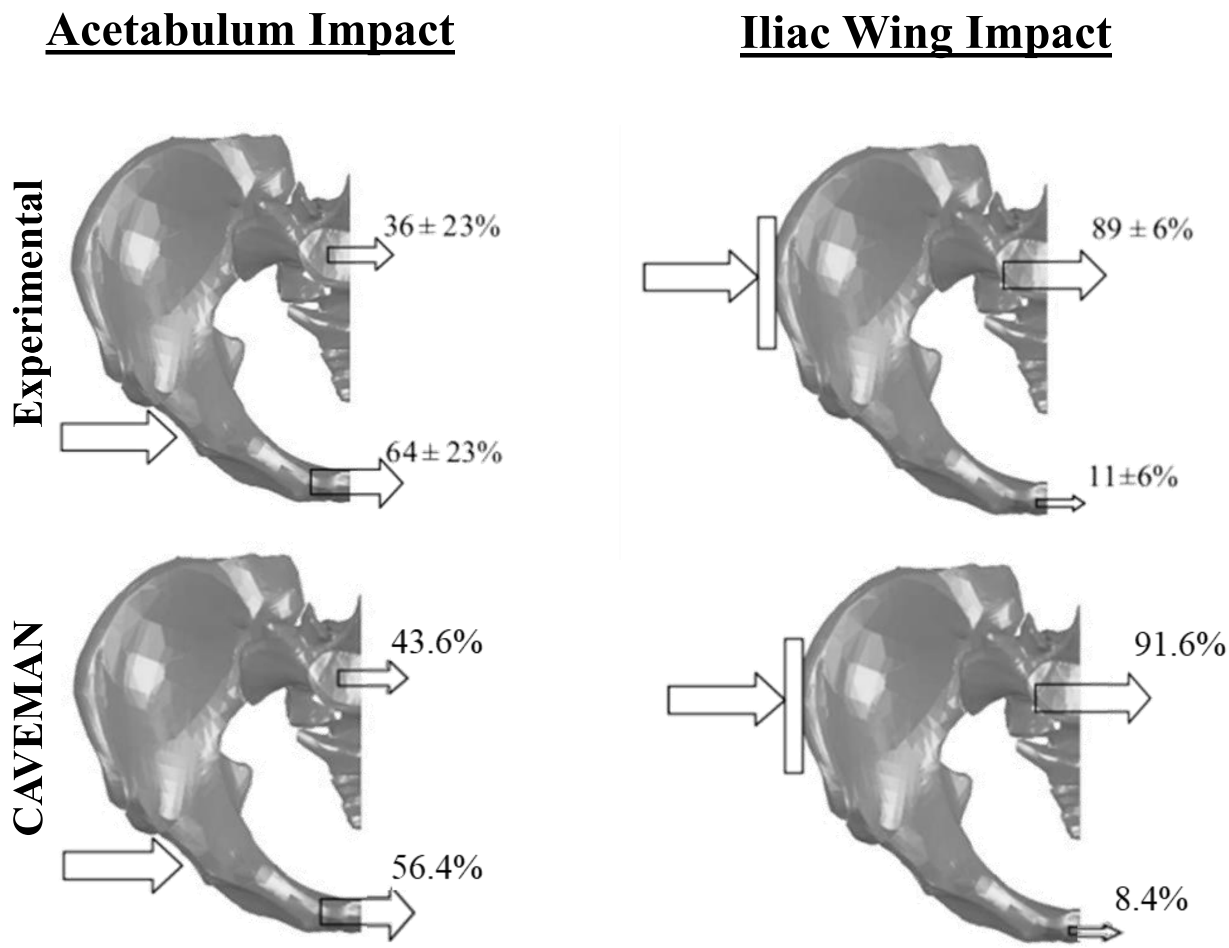

Figure 36. Comparison of the dynamic peak force distribution between Salzar's test series and the finite element pelvis model.

In summary, the pelvis model force response compares favorably to the experimental data. The dynamic force distributions are within 1 SD of the PMHS data set. If a model response trace was changed to the same color and viewed alongside the other experimental traces it would not be easily identifiable from the experimental traces. That being said, a qualitative evaluation is not robust or scientific, therefore an objective metric was used to evaluate the biofidelity of the pelvis model's biomechanical response.

4.2.2. CORA scoring to evaluate variation between experimental traces and to assess the biofidelity of the FE pelvis model

CORA (CORrelation and Analysis) is a correlation and rating method that compares data signals. Gehre et al. 2009 has an extensive resource for understand CORA scoring, but the basics of CORA are summarized below. Possible CORA scores range from 0 to 1, where 0 is no correlation and 1 is an exact fit. (CORAplus Release 4.0.4 User's Manual, Thunert 2017). This global rating is calculated by an equally-weighted combination of a corridor method and cross correlation method (Figure 37). The corridor method takes average of the reference signals (such as PMHS data) then an inner and outer corridor are constructed along this average signal. These corridors are created based off a certain prescribed percentage of peak values. When the evaluated signal is within the inner bounds it scores a 1; if it is in the outer corridor it transitions from 1 to 0; if a signal exits the outer corridor it will receive a score of 0. The bare minimum needed to run the cross-correlation method portion of a CORA analysis is two curves. In this analysis comparisons between the model signal and the experimental signal are made with regards to the shape, phase, and size differences between the signals (Figure 38). A full mathematical description of the cross correlation scoring used in this thesis is available for reference in the Appendix.

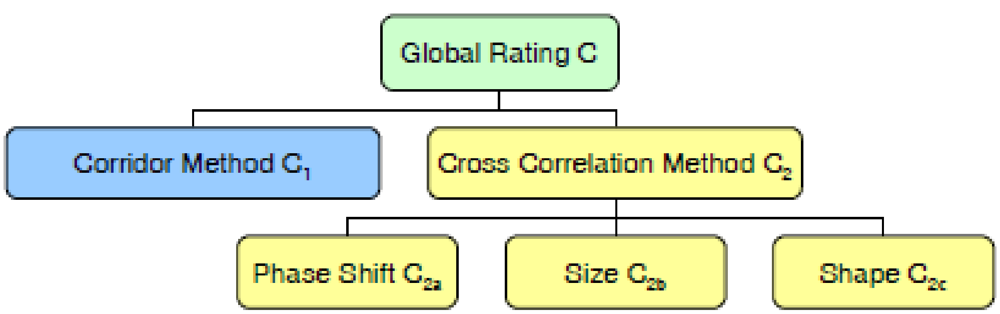

Figure 37. Method diagram illustrating the steps to calculating the global rating ranging from 0 to 1. (Gehre et al. 2009)

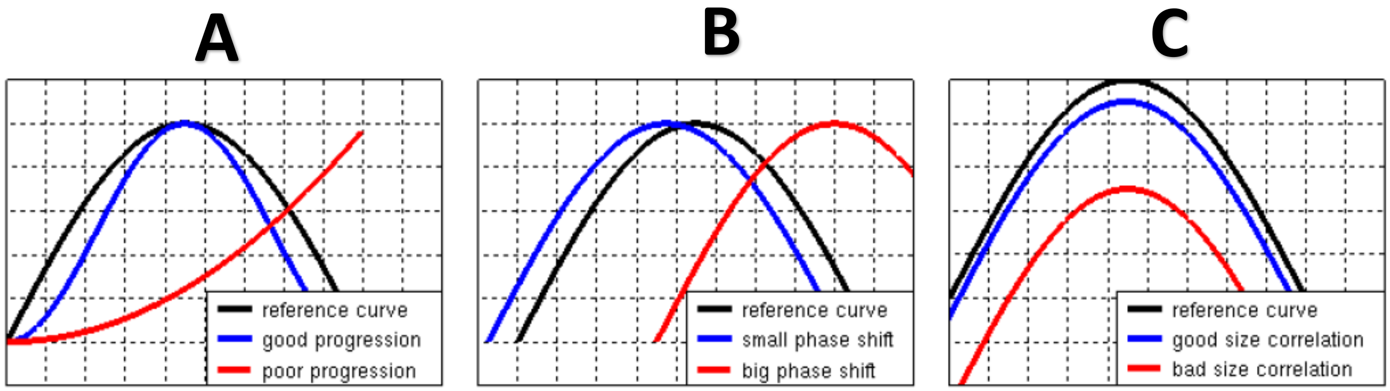

Figure 38. Description of the rating metrics for the cross correlation method (A) Progression/Shape G_V rating, (B) Phase Rating G_P, (C) Size/Magnitude G_G Rating (CORAplus Release 4.0.4 User's Manual, Thunert 2017)

An issue with using the cross correlation method of the CORA scoring is that it does not account for the large variation of response naturally observed from PMHS specimen to specimen. This is partially addressed by incorporating the corridor method into the CORA analysis, but that only affects one half of the score. For example, the lateral impact load cell signals from the FE model were compared to the average of the experimental data using default CORA parameters (Figure 39). These default parameters consider equal weighting between cross correlation and corridor, build inner and outer corridors based on the standard deviation of the experimental average curve, and give an equal weighting to cross correlation shape, phase, and size. Looking at Table 4, CAVEMAN scores ranged from 0.612 to 0.749. According to ISO/TR 9790 (CORA Manual), these scores give biofidelity ratings considered "fair" to "good". However, these types of biofidelity grades were created primarily for ATD evaluation, which are expected to have little variation between test dummy to test dummy response. Also, it is easy to manipulate the corridor portion of this scoring to artificially inflate CORA scores, negating the purpose of an objective rating method. The question becomes, how can the CORA biofidelity score be used for PMHS data which may have significant test to test variability? And further, can a statistical test be used to distinguish the difference between a model response and a group of empirical responses, rating than rely on an arbitrary rating system?

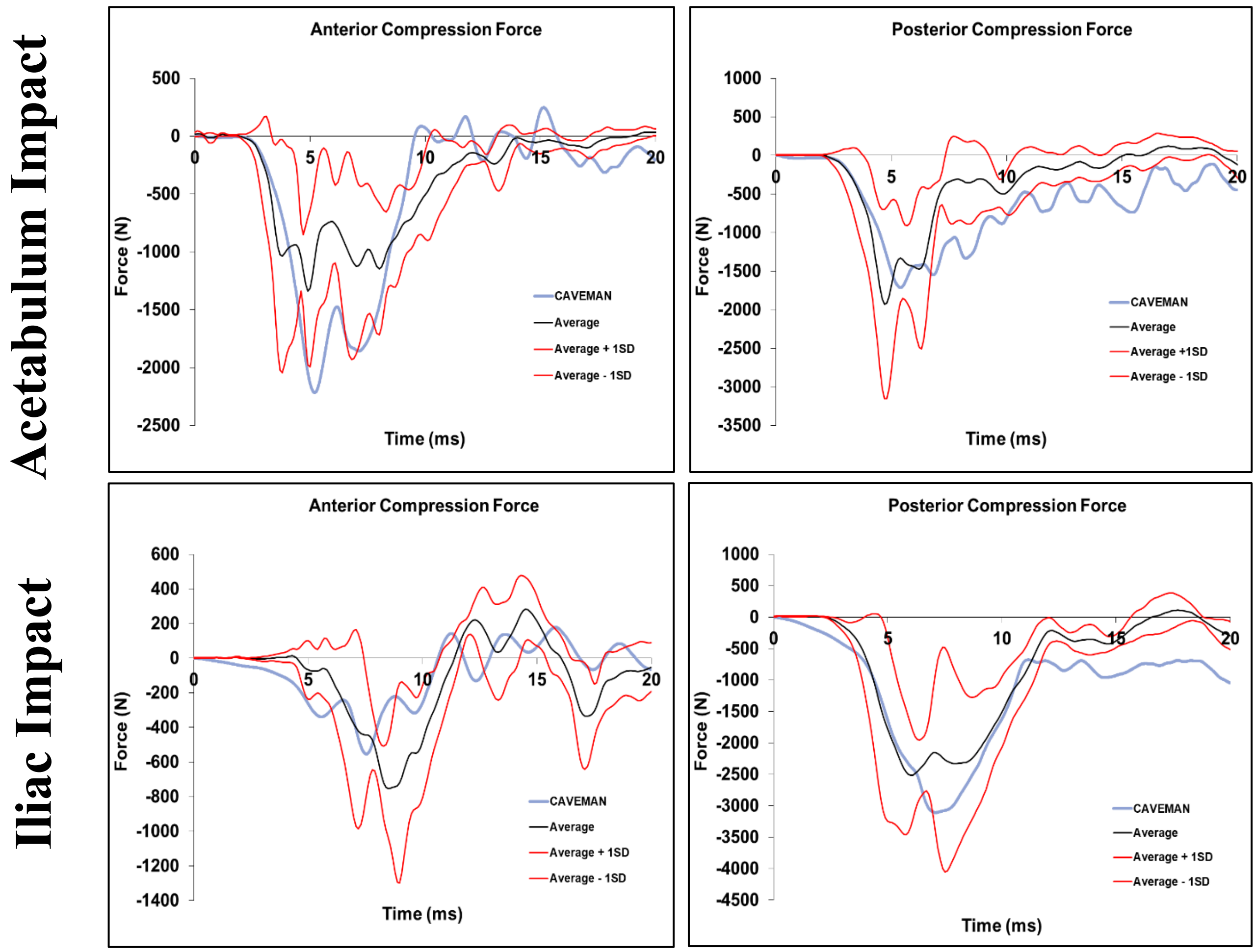

Figure 39. CAVEMAN pelvis force responses in lateral impact compared to the experimental average. Standard deviation corridors included for reference.

Table 4 The CORA scores comparing the average and CAVEMAN signals and consider a corridor built off the average experimental response curve and standard deviations of that curve.

CORA Scores of CAVEMAN Compared to PMHS Average Responses	Anterior - Acet Impact	
	CORA Score	0.748
	Posterior - Acet Impact	
	CORA Score	0.664
	Anterior - Iliac Impact	
	CORA Score	0.732
	Posterior - Iliac Impact	
	CORA Score	0.612

To answer these questions, the corridor scoring method of CORA was omitted from the analysis, and instead, the cross correlation method was applied between each PMHS test to PMHS test to assess how comparable the test data was to itself. Then, the FE model response was compared to each PMHS test individually, also using the cross correlation method, and these scores were compared to the scores amongst the PMHS data. Using this method accounts for the cadaver signal variability and the pelvis FE model can be compared in the same manner to see if it performs as well as a randomly selected pair of individual cadaver tests. With these sets of CORA scores, an average experimental test-to-test score was determined and compared to the average test-to-model score. Acceptable biofidelity was determined if the average FE model's score was within 1 standard deviation of the average experimental score and student t-tests were performed to determine if differences between the experimental and model responses were significant.

For this study, the default parameters for cross correlation method of CORA were left the same, except the phase, magnitude, and shape of the signals were given equal weighting (Table 5). D Min and Max were defined to capture the loading regime of interest across each data signal. Between 2 and 14 ms were when the signal's cross-correlation score was evaluated.

Table 5. CORA parameters used for the test to test to CAVEMAN signal cross correlation analysis. Notice the G_1 parameter is set to zero, thus ignoring any of the corridor related scoring, keeping it cross correlation scoring the signals only.

CORA Parameters Used for Test to Test to CAVEMAN Signal Analysis					
A Thres	**B_THRES**	**A_EVAL**	**B_DELTA_END**	**K**	**G_1**
0.002	0.014	x	x	x	x
a_0/b_0	**a/b_sigma**	**D_MIN**	**D_MAX**	**INT_MIN**	**K_V**
x	x	0.01	0.12	AUTO	10
K_G	**K_P**	**G_V**	**G_G**	**G_P**	**G_2**
1	1	0.33	0.33	0.33	1

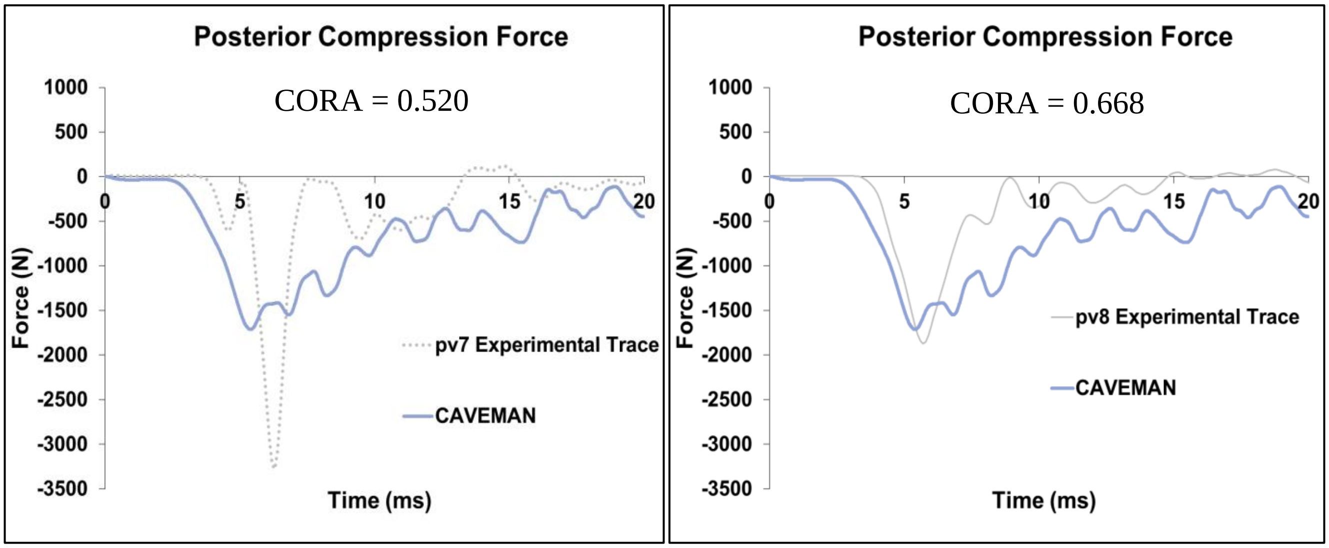

Figure 40. Examples of two differing signal cross correlation scores. This figure illustrates the variability that can exist between PMHS tests. These signals are both taken from an acetabulum impact, posterior load cell.

When compared to the experimental data scoring, the pelvis FE model scored within 1 SD in both the anterior and posterior force traces for each impact condition. This establishes that the model predicts forces through the pubic and sacroiliac joints as well as a random specimen from the sample of data in the UVA test series. In certain cross correlation signal evaluations, the FE model trace was almost the same as the cadaver pelvis, and in other cases, it performed quite poorly. Figure 40 illustrates how variance in the PMHS signal data test to test can lead to drastically different CORA scores. Tables 6 and 7 exhibit the simulation matrix, individual scores, and average CORA scores obtained between the experimental and simulation data. Putting a grade on correlation such as excellent, good, fair, or marginal is impractical when using CORA scoring to evaluate FE models compared to PMHS data, particularly because these categorical assessments were developed to describe ATD kinematic response which is generally easier to match than highly localized FE model response. This new analysis method of evaluating a validation data set with variability provides proper criteria to decide if a model's signals are biofidelic based on CORA scores.

Table 6. CORA scoring results from the experimental acetabulum impact test-to-test and the test-to-model evaluation. The average test-to-model score is within 1 SD of the average test-to-test.score.

Anterior - Acet Impact							
	pv5	**pv6**	**pv7**	**pv8**	**pv9**	**pv10**	**CAVEMAN**
pv5	x	0.440	0.6381	0.670	0.360	0.485	0.712
pv6		x	0.308	0.492	0.524	0.624	0.702
pv7			x	0.583	0.427	0.521	0.398
pv8				x	0.600	0.701	0.476
pv9					x	0.724	0.326
pv10						x	0.630

Average CORA Scores Anterior Acet Impact			
avg exp	0.540	**sd**	0.119
avg FE	0.541	**sd**	0.149

Posterior - Acet Impact							
	pv5	**pv6**	**pv7**	**pv8**	**pv9**	**pv10**	**CAVEMAN**
pv5	x	0.488	0.736	0.717	0.573	0.447	0.810
pv6		x	0.414	0.511	0.649	0.589	0.596
pv7			x	0.602	0.432	0.410	0.520
pv8				x	0.520	0.526	0.668
pv9					x	0.746	0.477
pv10						x	0.370

Average CORA Scores Posterior Acet Impact			
avg exp	0.557	**sd**	0.111
avg FE	0.574	**sd**	0.141

Table 7. CORA scoring results from the experimental iliac wing impact test to test evaluation, as well as test to CAVEMAN. The average" to single test" CAVEMAN score is within 1 S.D. of the average "experiment to experiment" score.

Anterior - Iliac Impact							
	pv11	**pv12**	**pv13**	**pv14**	**pv15**	**pv16**	**CAVEMAN**
pv11	x	0.200	0.3819	0.265	0.409	0.451	0.433
pv12		x	0.829	0.590	0.657	0.461	0.694
pv13			x	0.631	0.686	0.595	0.698
pv14				x	0.304	0.636	0.698
pv15					x	0.410	0.672
pv16						x	0.277

Average CORA Scores Anterior Iliac Impact			
avg exp	0.500	**sd**	0.171
avg FE	0.579	**sd**	0.165

Posterior - Iliac Impact							
	pv11	**pv12**	**pv13**	**pv14**	**pv15**	**pv16**	**CAVEMAN**
pv11	x	0.360	0.491	0.411	0.482	0.658	0.436
pv12		x	0.826	0.834	0.810	0.459	0.604
pv13			x	0.962	0.909	0.672	0.588
pv14				x	0.799	0.613	0.597
pv15					x	0.637	0.572
pv16						x	0.545

Average CORA Scores Posterior Iliac Impact			
avg exp	0.662	**sd**	0.184
avg FE	0.557	**sd**	0.057

Looking at Tables 6 and 7 and the average CORA scores in particular, it is apparent that the FE data traces compare well to the experimental results. Taking this analysis further, two-sample Student's t-tests were performed on the CORA scores of the computational and experimental results to test the null hypothesis: the model-to-experimental CORA scores are not distinguishable from the experimental-to-experimental CORA scores. Unequal variance was assumed based on F-Tests on the sample variances. The following p-values were determined for each data trace: anterior acetabulum impact 0.99, posterior acetabulum impact 0.82, anterior iliac wing impact 0.37, and posterior iliac wing impact 0.08. Based on these p-values being greater than the 0.05 cutoff, the null hypothesis was not rejected, implying that the force responses of the FE model were not distinguishable from those observed in the experimental data, although the differences in the posterior iliac wing response and trending toward significant. In the Appendix further scoring outcomes for the individual phase, size, and shape metrics are included for reference. The different method of using CORA in this thesis, using the cross-correlation method to see if there are statistical differences between the simulation compared to the experimental dataset's variability, is a useful method for validating model biofidelity.

Previously published analysis (Vavalle et al. 2013) comparing different objective rating methods between PMHS data and FE results found that CORA provided the most comprehensive signal evaluation. That being said, the authors of that analysis suggest that for any comparison method multiple assessments should be used for a robust assessment. For an injury predictive FE model, analysis should extend into evaluation of the feasibility of injuries predicted by the model with those observed in the experimental data. A direct comparison of the PMHS injuries in each impact condition to the FE model predictions was explained in the proceeding section.

4.2.3. Injury Prediction

The most important criteria to judge the FE model's performance is its ability to properly reproduce injuries from the validation cases. This is the only way to know if the injury predictive aspect of the model is behaving in a biofidelic manner. The pelvis FE model simulates injuries by an element deletion method: an element of bone is deleted upon hitting a certain maximum principal strain value. As explain in section 3.1.2. the cortical bone elements were dictated by a 1.50% strain threshold; the cancellous bone elements had a strain threshold of 25.0%.

The injuries reported in Salzar's test series were consistent for across each impact. In the acetabulum impacts displaced pubic ramis and ischium fractures were generally observed, completely dismantling the ability of the pelvis to transmit load on the anterior side. Along with the anterior injuries, posterior fractures of the sacrum were observed in 5/6 impacts. The single test without sacral injury experienced complete disruption of the posterior sacroiliac ligaments. These sacral fractures were generally vertical oriented passing through the right sacral holes. The injury mechanism of the sacroiliac joint and sacrum (Lebarbe et al. 2016) has been traced to the initial failure of the pubic areas of the pelvis. The failure of the pubic ramus allows for the posterior pelvis to rotate forward and inward causing bending and tensile fractures of the sacrum or even SIJ rupture. It has been observed in literature that avulsion type fractures of the sacrum can be induced by sacroiliac joint ligaments (Steinke 2014). The pelvis FE model's injury prediction in the acetabulum impact scenario was consistent with the experimental data and injury mechanisms defined in literature. For the acetabulum impact the following injuries were observed in the pelvis model: displaced fractures of the right ilio pubic ramus and right ischio pubic ramus, vertical fracture of the sacrum body through S1 to S3 right sacral holes, superior through the sacra ala. Injuries occurring in the pelvis FE model acetabulum impact scenario are presented in Figures 41 and 42. A diagram view is available in Figure 43. Compared to the PMHS test series, similar anterior pelvis fractures occurred in 5/6 pelvises tested. Similar posterior fractures occurred in 4/6 pelvises tested. Overall the injury patterns predicted by the pelvis FE model were consistent with 4/6 impact tests. The two non-corroborative injury outcomes from the dataset included an immediate acetabular cup failure as well as a case where SIJ soft tissues ruptured, preventing posterior sacral injury.

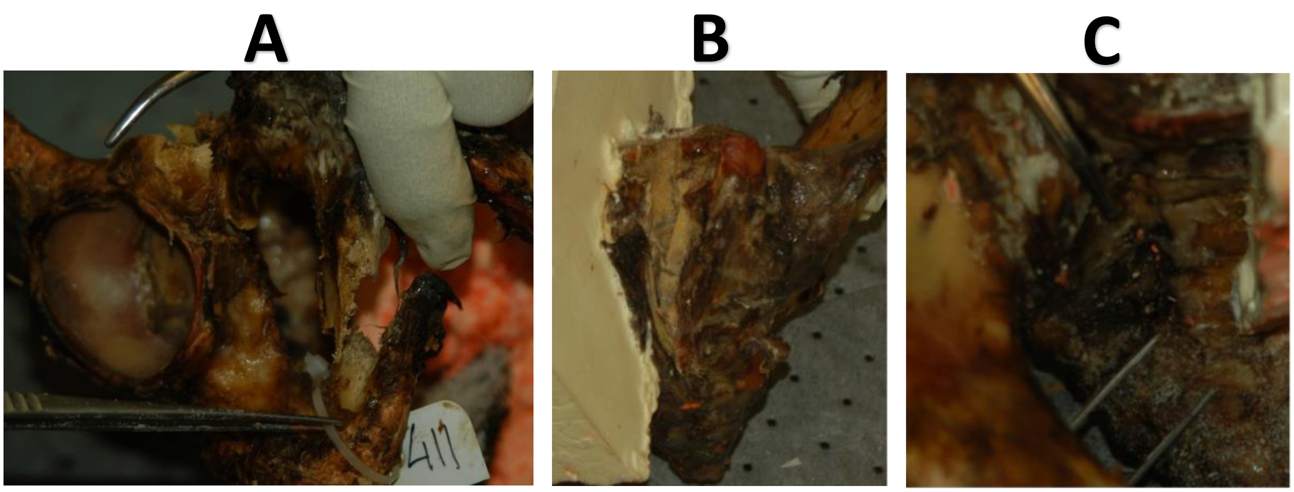

Figure 41 Cadaveric images showing the fractures occurring during an acetabulum impact. A. Ramis and Ischium fractures of the anterior pelvis. B. Posterior fracturing of the sacrum, particularly along the SIJ-Bone interface. C. Anterior sacrum fractures through the sacral holes. (These images are from the same cadaver from PV6 test in the Salzar test series.)

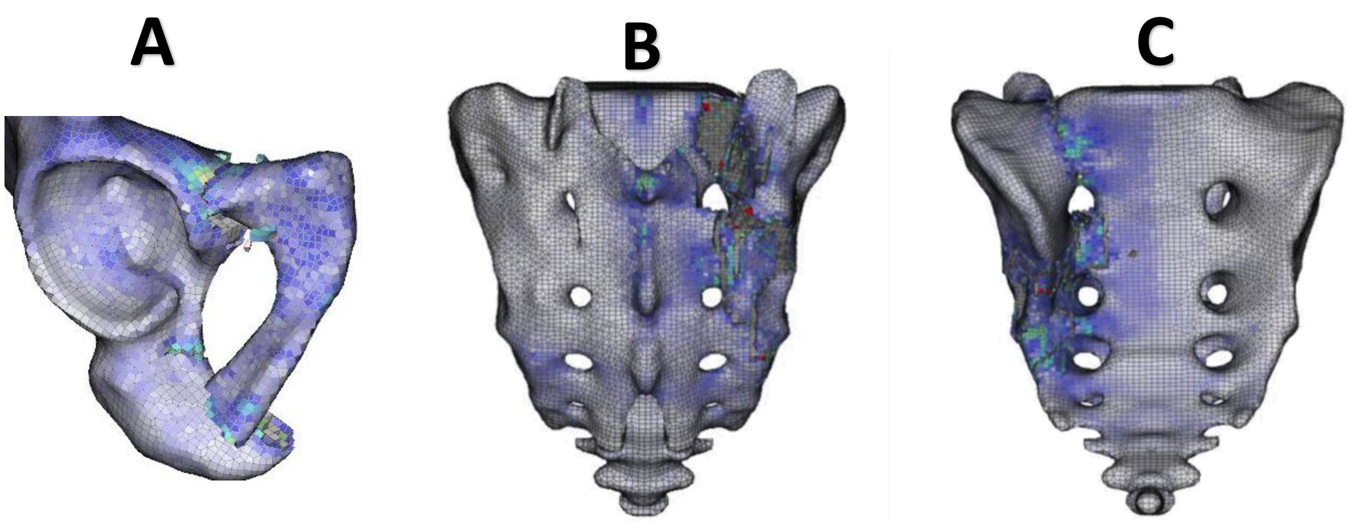

Figure 42. Injuries predicted in the CAVEMAN model for the acetabulum impact condition. A. Pubic ramis and ischium fractures. B. Posterior sacrum fractures are predicted, in part induced by the SIJ since the deletion is beginning at the ligament bone interface. C. Anterior pelvis fractures through the sacra ala and sacral holes.

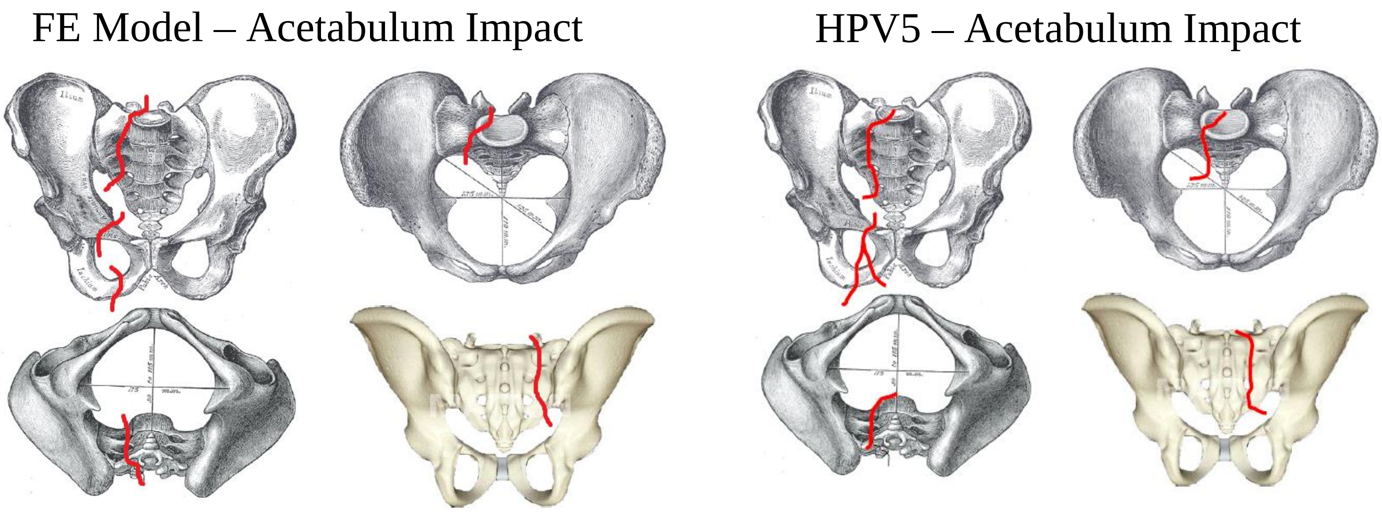

Figure 43. Left: Fractures occurring in the pelvis model during acetabulum impact. Right: Fractures occurring in a cadaveric pelvis (HPV5) during acetabulum impact. impact. This injury pattern occurred in 4/6 pelvises in the acetabulum impact condition.

In the iliac wing impacts, fractures reported and observed were restricted to the sacrum. Injuries in the data set consist of dislocations of the SIJ, fractures through ossification bridges between the ilium and sacrum, and compressive non-displaced fractures to the right sacrum at the SIJ interface. An example of a compressive fracture to the sacrum at the joint interface is presented in Figure 44. Described laxities and dislocations of the SIJ are not quantifiable or observable in simulations because these types of injuries are a function of the soft tissues that comprise the SIJ complex. Again, the fractures occurring in the pelvis model during the iliac wing impact scenario compared favorably to Salzar's data set. For the iliac wing impact, the following injuries were observed in the pelvis model: fracture on the surface of the sacrum at the SIJ interface and posterior vertical fracture towards the sacra ala (Figures 44 and 45). The fractures occurring in the iliac wing impact condition were less catastrophic than those occurring in the acetabulum condition. See Figure 46 for diagram views of the fractures occurring in the pelvis model and a cadaveric pelvis in iliac impact. Overall the fracture pattern consisting of posterior sacral joint interface fractures occurred in 4/6 pelvises tested in the iliac wing impact. Two of the pelvises impacted did not experience fractures. A comparison of the force-time histories of the FE pelvis, injurious, and non-injurious response is available in the Appendix.

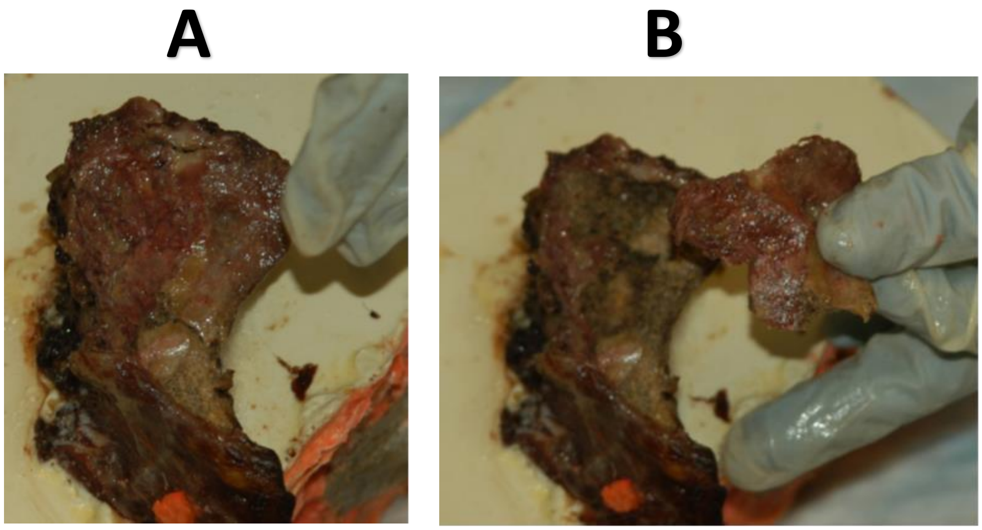

Figure 44. Cadaveric images showing the fractures occurring during an iliac wing impact. A. Comminuted fracture occurring on the sacrum at the sacrum-ilium interface. B. Shows how severely the interface at the sacrum is compromised, the cracked bone can be removed by hand.

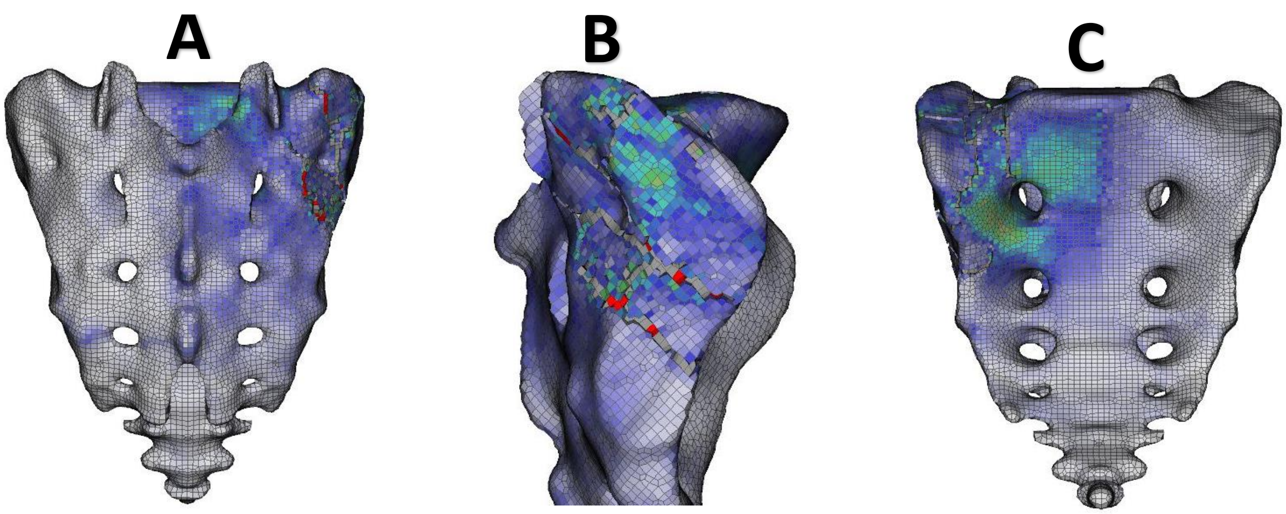

Figure 45. Injuries predicted in the sacrum model for the iliac wing impact condition. A. Posterior sacrum fractures are predicted, begin to travel from SIJ surface to sacra ala. B. Lateral view of the sacrum shows extensive element deletion predicting fracture in the SIJ interface. C. Anterior pelvis fractures can only be viewed in the superior sacra ala.

Based on the results of the lateral impacts to the pelvis model, the FE model predicts injuries that compared favorably to those reported in Salzar's experimental study. Both the model and test data suggest that impacts to the anterior portion of the pelvis, the acetabulum portion, pose a greater risk of serious injury to the pelvis. In lateral impacts to the acetabulum, fractures of the sacrum only occur after the complete displacement fractures of the pubic ramus. In the iliac wing impacts, fractures of the anterior pelvis were not observed. This corroborates with the findings of the force distributions determined in the preceding section. During iliac wing impacts 90% of the force travels through the sacrum and SIJ complex, which is beneficial for the integrity of the pelvis since these are primarily compressive loads. Further evaluation of the fracture tolerances of the pubic ramus warrant further study based on the results of the experimental and computational data. This type of analysis will be included in the following chapter.

FE Model – Iliac Wing Impact

HPV15 – Iliac Wing Impact

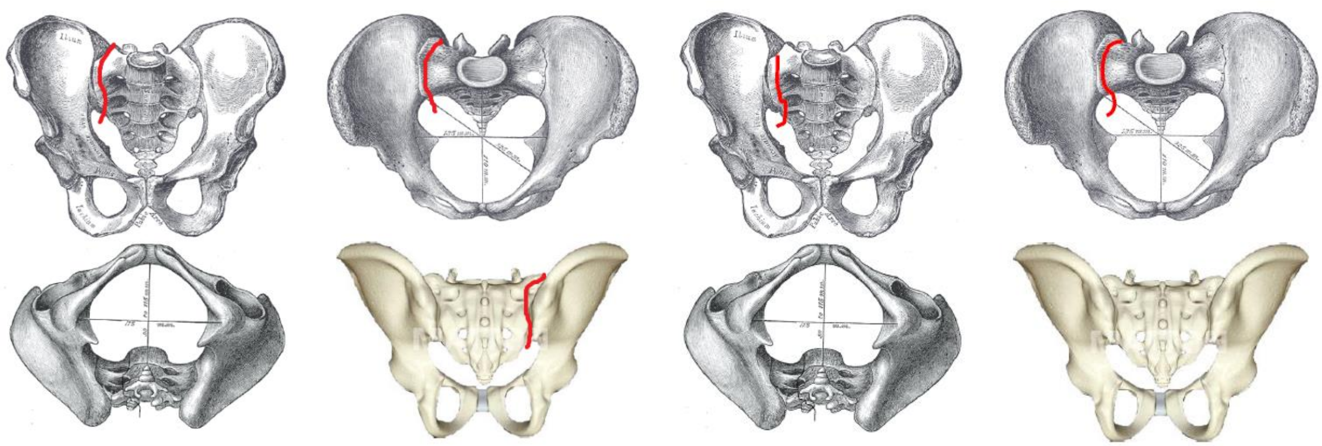

Figure 46. Left: Fractures occurring in the CAVEMAN pelvis model during iliac wing impact. Right: Fractures occurring in a cadaveric pelvis (HPV15) during iliac wing impact. This injury pattern occurred in 4/6 pelvises in the iliac wing impact condition.

A full description of the injuries observed in the Salzar dynamic lateral impact tests are presented in Appendix E. Now that the force traces and injury prediction has been validated against experimental data it is possible to use the pelvis model in accessory studies to gain further insight into lateral pelvis injury.

4.3. Defleshed Pelvis Model Parameter and Variation Study

A sensitivity study was conducted on the material properties of the FE model pelvis, similar to what was done with the lower extremity to gain more insight into which parameters were driving the force response and predicted injuries. In addition to the material sensitivity study, another study examining the potential effect of ossification, ridging, and fusion of the pelvic joints was performed.

4.3.1. Material parameter study methodology and results

Based on the work done with the lower extremity as shown prior, it was anticipated that the connective tissues that connects the bones such as the pubic symphysis and sacroiliac joint would have a substantial effect on model response. To assess this, the baseline pelvis model material parameters were varied, systematically, to measure the effect on force response and injury prediction. The following parameters were varied: cortical bone stiffness + and – 50%, cortical bone failure strain + and – 33%, cancellous bone stiffness x0.1 and x10, cancellous bone failure strain + and – 33%, pubic joint ligament and disc stiffness x0.1 and x10, and sacroiliac joint ligament stiffness x0.1 and x10. The full simulation matrix and its results are provided in Table 8.

Somewhat surprisingly, the cancellous bone stiffness had the greatest effect on the response of the pelvis model force in lateral impact, with cortical bone properties, SIJ ligaments, and pubic ligaments showing less sensitivity. These results were in contrast to the results of the sensitivity study done on the lower extremity model. The sensitivity to cancellous bone properties are presented in Figure 47. An interesting phenomenon observed was the joint sensitivity was only observable in the single loading condition. For example, changing the stiffness of the SIJ in iliac wing impacts had a greater effect than in acetabulum impacts and changing the stiffness of the pubic joint in acetabulum impacts had a greater effect than in the iliac wing impacts (Figure 48).

This type of direction dependent sensitivity ties back to the dynamic force distributions, where the observed load predominately travels through the either the anterior or posterior pelvis depending on impact conditions.

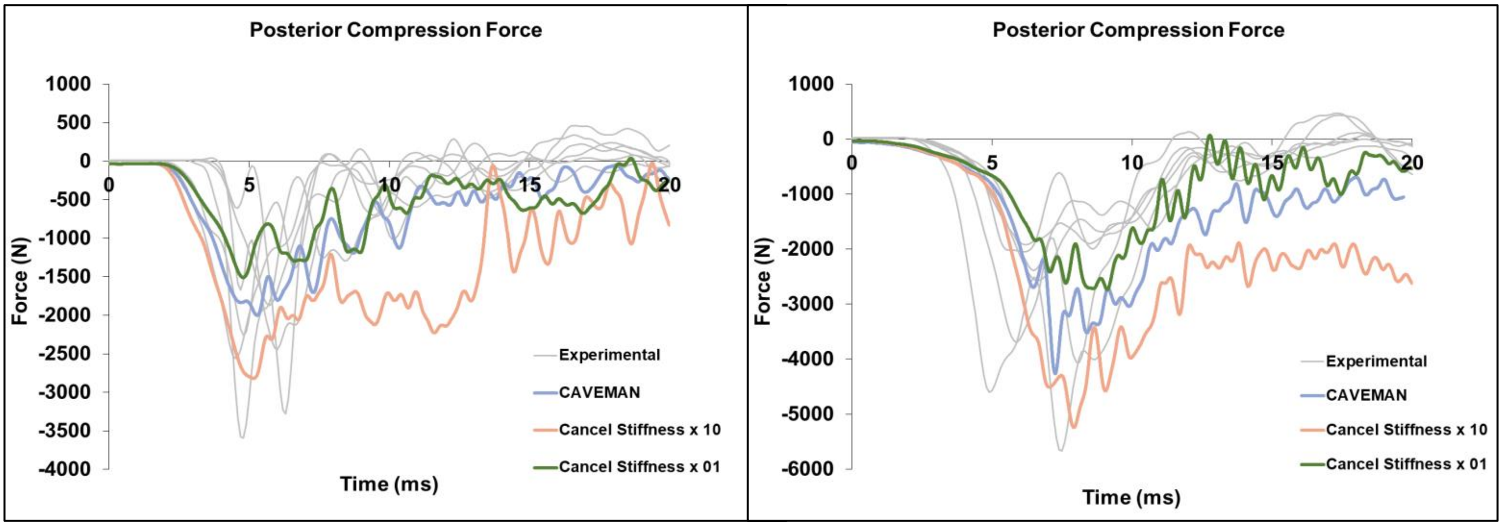

Figure 47. Examples of the posterior force response sensitivity to changes in the cancellous bone stiffness, for both the acetabulum and iliac wing impacts. The response of the model varies significantly based on the cancellous bone stiffness defined. The high volume of cancellous bone in the sacrum is hypothesized to be the cause of such significant sensitivity in the posterior force response.

Looking at the sensitivity the model has to the cancellous bone material properties and the lack of definitive literature on the mechanical characterization of cancellous tissue in the pelvis, an optimization using an inverse FE analysis was performed. Different values of cancellous bone stiffness were ran through each impact condition (within bounds of literature) and the best stiffness was determined based on model response compared to the experimental data. This optimization was centered around better matching the force responses in the Salzar impact conditions. It was determined that the less stiff cancellous bone models gave results more comparable to the experimental data. The optimization led to a value of E= 55 MPa and tangent modulus = 10 MPa stiffness being decided upon rather than the original E = 200 MPa and tangent modulus = 20 MPa. The tuned stiffness was in the lower bound of the pelvic cancellous bone properties defined in literature, but similar values were reported in Dalstra et al. 1993. This updated optimized model was used for all validation and accessory study simulations ran in section 3.3 and 3.5.

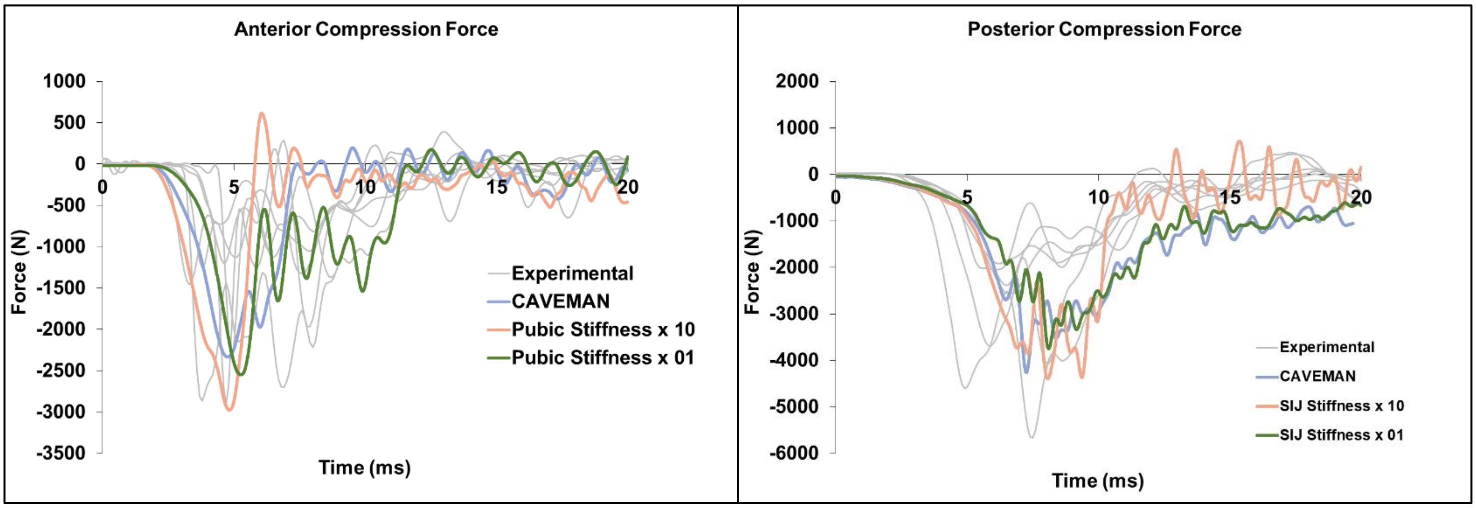

Figure 48. Examples of force responses that were sensitive to changes in model parameters. (left) Anterior compression force with variations in the pubic joint stiffness in an acetabulum impact. (right) Posterior compression force with variations in the sacroiliac joint stiffness in an iliac wing impact.

In summary, the pelvis FE model was most sensitive to changes in the cancellous bone stiffness. Cancellous bone makes up a large percent of the volume of the sacrum, which is why the model was especially sensitive in the posterior load cell. In this study, cortical bone properties were shown less sensitive, but it is worth noting that the stiffness values were altered less than the cancellous bone. Changes to the material properties were contained to the bounds of literature; bone stiffness was increased/decreased by half, not by an order of magnitude. Alterations to stiffness of the joints showed sensitivity in impacts where the joint was more engaged, such as when the anterior force for acetabulum impacts with pubic joint alterations and the posterior force for iliac wing impacts with the sacroiliac joint alterations. Future sensitivity studies should involve geometric considerations such as cortical bone thickness, acetabular cup shape, pubic joint width, wing to wing length, and pelvis height. It is hypothesized that these type of variations would play a significant role in the response and injury prediction of a pelvis FE model.

Table 8. Summary of material sensitivity study performed for the defleshed pelvis model, performed in both acetabulum and iliac wing impacts.

Summary of the Material Sensitivity Study - Acetabulum Impact				
Impact	**Variation Description**	**Change in Anterior Force Response**	**Change in Posterior Force Response**	**Change in Fracture**
Acetabulum	Cortical Bone Stiffness - 50%	N	N	N
	Cortical Bone Stiffness x 10	N	N	N
	Cortical Bone Failure Strain - 33%	Y	N	Y
	Cortical Bone Failure Strain + 33%	Y	N	N
	Cancellous Bone Stiffness x 0.1	N	N	N
	Cancellous Bone Stiffness x 10	Y	Y	Y
	Cancellous Bone Failure Strain - 33%	Y	N	N
	Cancellous Bone Failure Strain + 33%	N	N	N
	Pubic Joint Stiffness x 0.1	Y	N	N
	Pubic Joint Stiffness x 10	N	N	N
	Sacro-Iliac Joint Stiffness x 0.1	N	N	N
	Sacro-Iliac Joint Stiffness x 10	N	N	N
Summary of the Material Sensitivity Study - Iliac Wing Impact				
Impact	**Variation Description**	**Change in Anterior Force Response**	**Change in Posterior Force Response**	**Change in Fracture**
Iliac	Cortical Bone Stiffness - 50%	N	N	N
	Cortical Bone Stiffness x 10	N	N	N
	Cortical Bone Failure Strain - 33%	Y	N	N
	Cortical Bone Failure Strain + 33%	N	N	N
	Cancellous Bone Stiffness x 0.1	N	Y	Y
	Cancellous Bone Stiffness x 10	N	Y	Y
	Cancellous Bone Failure Strain - 33%	N	N	N
	Cancellous Bone Failure Strain + 33%	N	N	N
	Pubic Joint Stiffness x 0.1	N	N	N
	Pubic Joint Stiffness x 10	N	N	N
	Sacro-Iliac Joint Stiffness x 0.1	N	N	N
	Sacro-Iliac Joint Stiffness x 10	N	Y	Y

4.3.2. *Investigation into the simulated effects of pelvic joint dysfunctions in the elderly during lateral impact*

The purpose of this section is to investigate using a computational study how degeneration of the joints in the pelvis effect force distributions and injury outcomes. Older passengers are more likely to experience serious injury during automotive collisions (Morris and Welsh 2003). For the elderly, the effects of aging include increased mechanical fragility of biological components and physiological changes such as visual, morphological, and musculoskeletal decline (Yoganandan et al. 2007). Other studies show that around 40% of crashes involve drivers over the age of 65

(Lyman et al. 2002). As life expectancies increase and the quality of older age continues to improve, it is feasible to assume that there will be more elderly drivers on the road in the coming years compares to past decades. Consultation with Dr. Rob Salzar at UVA whom performed the defleshed pelvis impact suggested that varying mobility of the SIJs were observed in the PMHS specimen tested, partially attributed to the age of the specimens. Although the computational pelvis model has been developed for military related analyses, to represent a younger aged 50^{th} percentile male, the Salzar study specimens include an older population. Due to the perceived variance in ossification and SIJ mobility in the test data, these effects were simulated to understand the potential effect on model response. If degenerative differences have a significant effect on injury outcomes and force response, adjustments may need to be made to account for age related joint changes. Differences observed in the data set specimens' joint mobility were theorized to stem from ossification of the articular joint surfaces. Degeneration was simulated to understand if age related ossification would dictate pelvis response. It was theorized that it would be possible to distinguish different PMHS responses in the Salzar data by assuming a level of ossification of the pubic joints.

Rosatelli et al. (2006) performed a topographic study of the interosseous region of the sacroiliac joint complex. Axial sectioning determined that in the majority of cases ossification was observed in the central region of the interosseous ligament, essentially fusing the ilium and sacrum at the posterior side of the pelvis (Figure 49). Additionally, ridging was observed which could be reasonably theorized to further reduce the mobility of the joint. Rosatelli's description of these joint degradations states that all sacroiliac joint specimen greater than 60 years old had experienced a combination of either ridging or ossification (Table 9). It is worth noting that 20-year-old male specimen in this study had no ossification of the interosseous region and only slight ridging when compared to the older cadavers. If these changes are simulated in the pelvis model, it will be possible to see the consequence of such degeneration for lateral impacts to the pelvis.

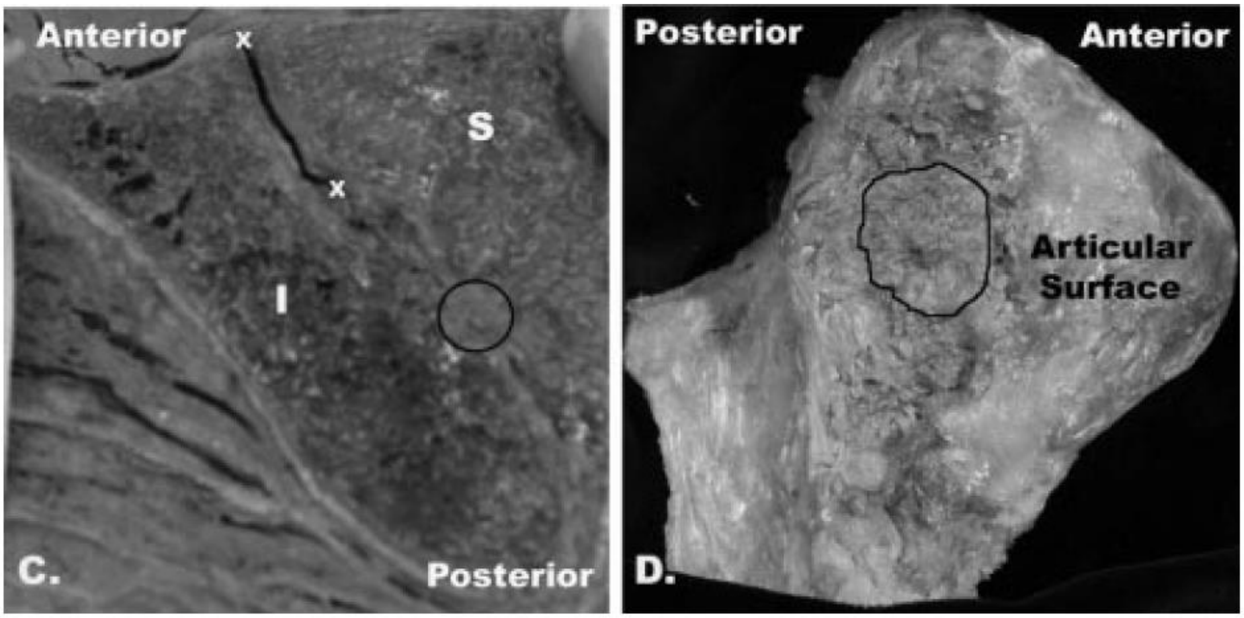

Figure 49. Superior and Medial SIJ views of an 84-year-old female cadaveric specimen. Circled areas point out ossification points of the interosseous sacroiliac ligament. (Rosatelli et al. 2006)

Table 9. Rosatelli et al. (2006) describes interosseous region degeneration with consideration to age group.

Summary of Interosseous Region of SIJ Topogrpahy - Rosatelli et al. 2006			
Age Group	**# of Specimen**	**Ridging**	**Region of Ossification**
20	1	Slight Ridging	None
55-67	6	3 Moderate 3 Extensive	1 None 1 Fibrotic 4 Central
80-91	4	1 Moderate 3 Extensive	1 None 1 Superior Anterior 2 Central

The pelvis FE model was run with simulated sacroiliac joint degeneration. Based on the regions of ossification reported in Rosatelli, the material properties of the interosseous ligament were changed to cortical bone. Next the articular surfaces of the sacrum and ilium were artificially "ridged" by increasing the friction definitions between the two articular surfaces from 0.2 static and 0.1 dynamic to 0.95 static and 0.85 dynamic. It was assumed that drastically changing these friction coefficients could simulate riding without making geometric morphing changes to the articular surfaces. Upon running the iliac and acetabulum impacts, there was not a significant change to the model response with these ossification type effects added to the sacroiliac joint. More sensitivity was shown with the iliac wing impact, which makes sense when compared to the results of the material sensitivity study in the prior section (Figure 50).

There are also prominent morphological changes observed in the pubic symphysis

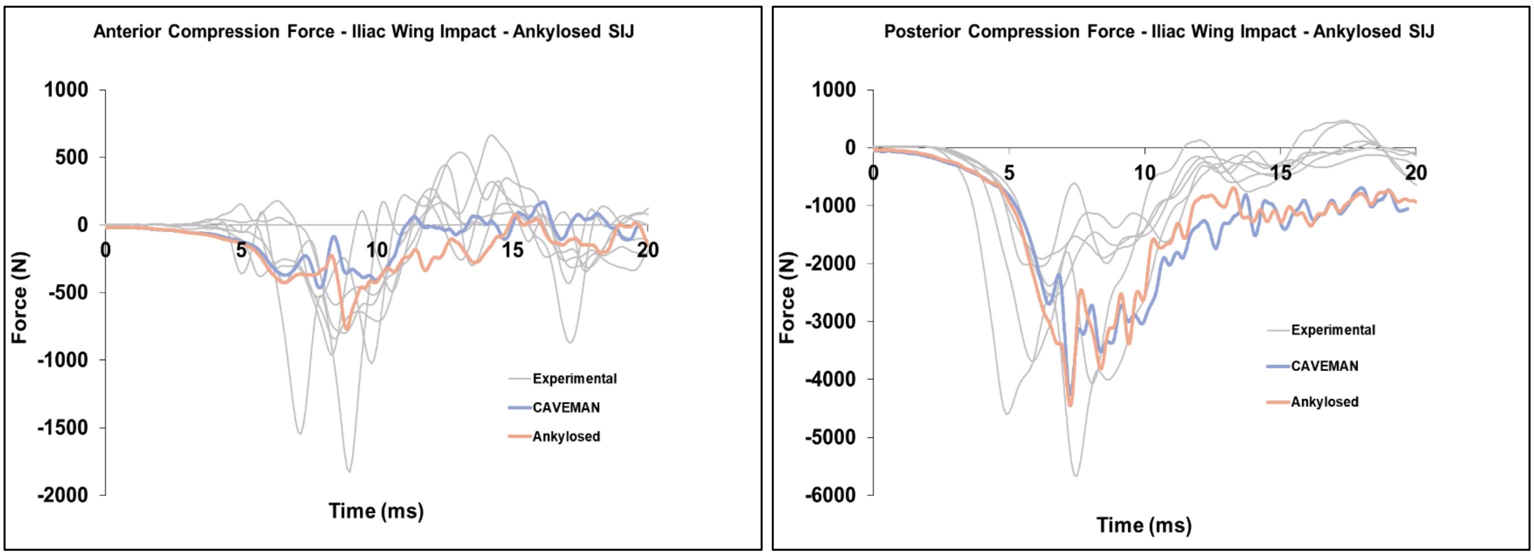

Figure 50. Force response of the simulated ankylosed SIJ pelvis compared to a baseline model. Close to no sensitivity was observed in the acetabulum impact case with simulated anklyosis of the SIJ.

throughout the aging process. Jajic and Grazio 2000 examined ankylosis spondylitis arthritis related changes of the pubic symphysis with radiological scans, within a sample of 66 men. This type of arthritis more often effects men and although begins onset in early adulthood its effect become more serious with aging (Figure 51). Morphological features including ossification of the pubic symphysis have also been used to identify the age of human remains in previous studies (Sarajilic and Gradascevic 2012) so age related changes to the symphysis are documented in the literature. This type of degeneration was modeled in the pelvis by simply changing the material definitions of the pubic symphysis disk to cortical bone to simulate full ossification of the joint. The results of this test for an acetabulum impact are presented in Figure 52.

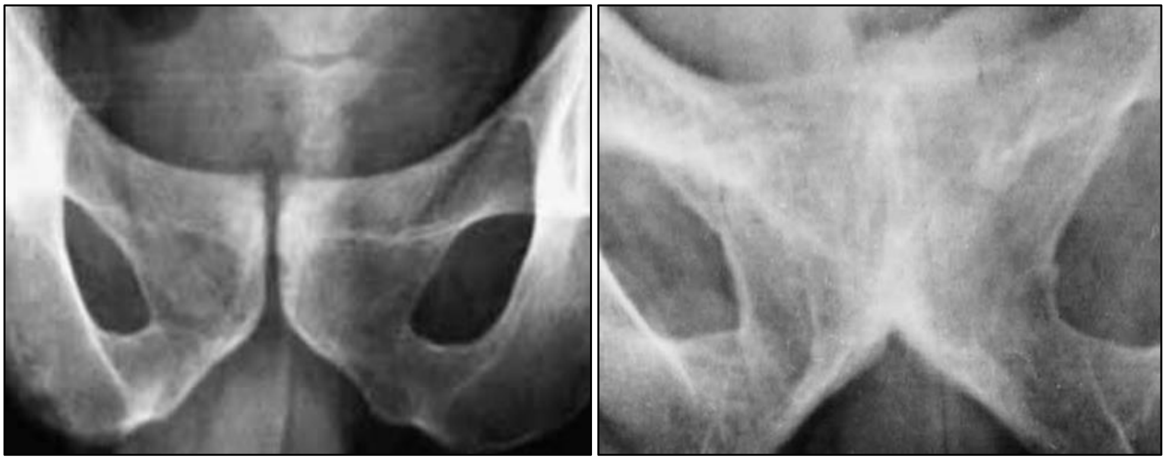

Figure 51. Radiographies of a healthy (left) and severely ankylosed (right) pubic symphysis (Jajic and Grazio 2000). Bridging of the pubic symphysis in the ankylosed specimen included the superior pubic ligament.

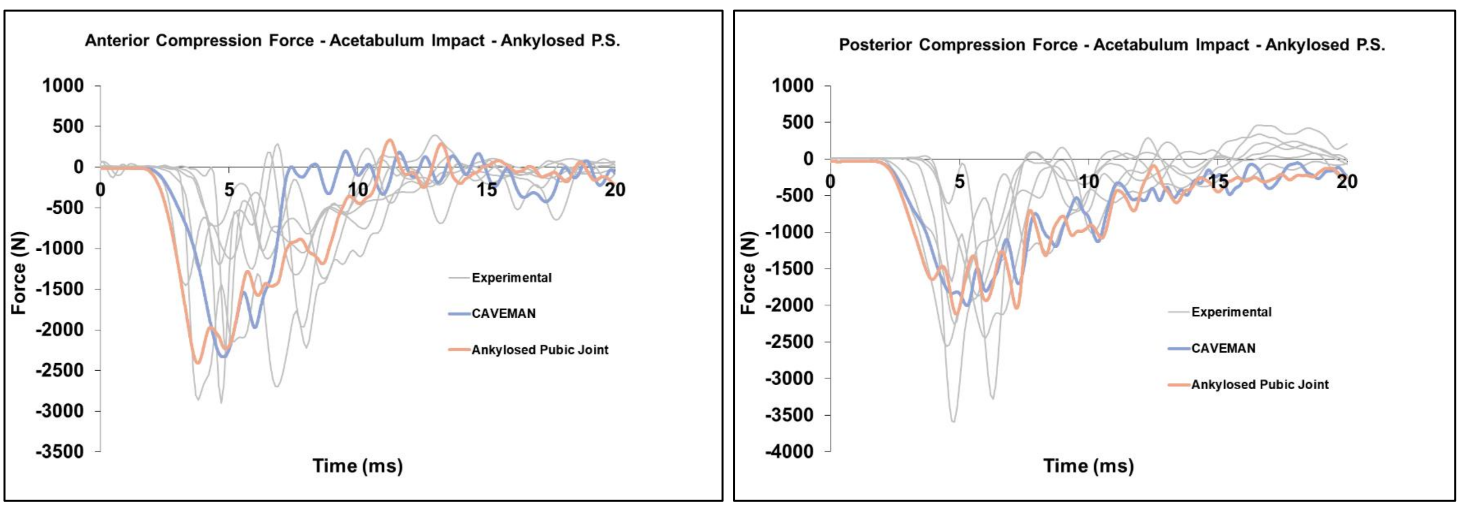

Figure 52. Force response of the simulated ankylosed pubic joint pelvis compared to a baseline model. Almost no sensitivity was observed in the iliac wing impact case with simulated anklyosis of the pubic joint.

In summary, the results of these instances of simulated ossification suggest that aging related ossification of the pelvis joints do not significantly affect the response of the human pelvis in lateral impact. This rejects the hypothesis that lack of mobility attributed to ossification observed in the Salzar data set had a strong effect on pelvis response. Most likely, morphometric variation played a large role in the variability of the Salzar pelvis responses. Analysis on the sensitivity to geometric differences would be a valuable future study, examing whether particular variances would predispose a pelvis to a particular injury pattern. However, based on this FE study, age of the cadaver pelvis should not be of huge concern, at least related to ossification of the SIJ. Although the average PMHS age was 60 years in the Salzar data set, it still has direct applicability to the current pelvis model, which was developed to represent a warfighter associated with a younger age. Another question that could be posed: would other age related changes have any effect on response? Based on prior pelvis lateral impact studies on the relation between injury and age, the answer seems to be no.

Ramachandra et al. 2017 investigated the injury risk of during near side impacts with respect to driver age, sex, and considered anatomical location of injury. There was an increased risk of injuries for those over 60 years old, especially for females, however there was not a strong correlation found for an increased risk of pelvis injury (Figure 53). These conclusions from Ramachandra's study support the simulation results in this section, which suggest that aging of the pubic and sacroiliac joints does not increase the injury risk of the human pelvis in lateral automotive type loading. For protecting elderly populations in nearside impacts, the data suggests that more efforts should focus on protecting the head, thorax, abdomen, and lower extremities. Future degeneration related studies of the pelvis joints would seem to have more applicability in orthopedic and mobility related studies, not injurious impact biomechanics; at least for lateral impact.

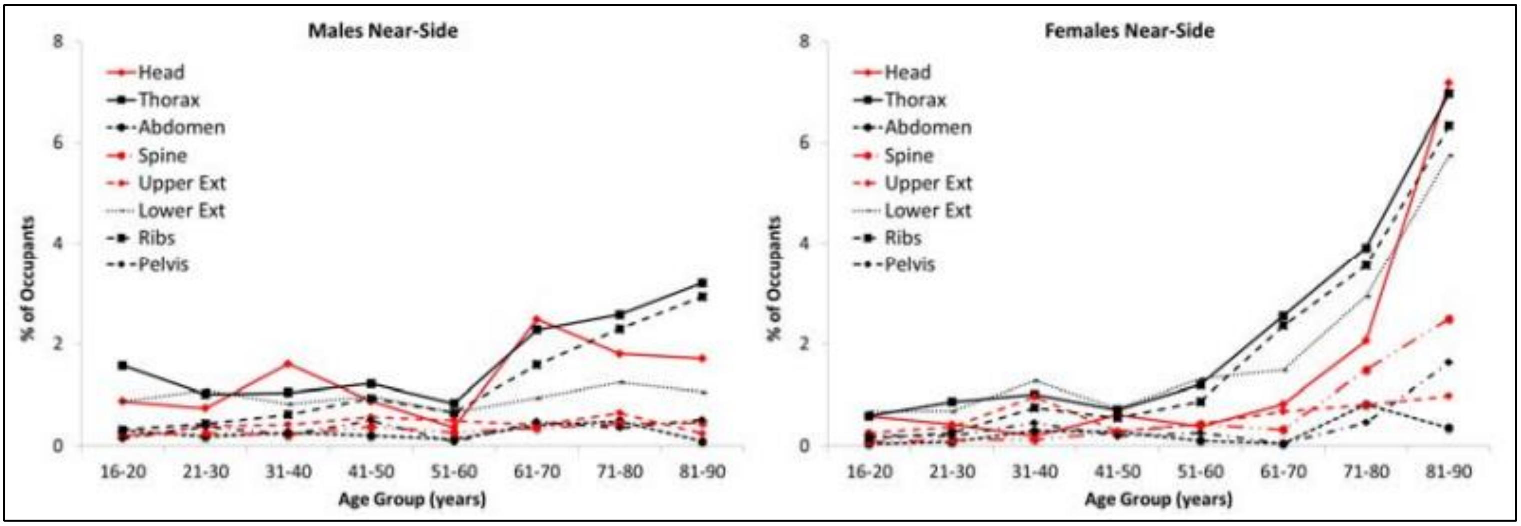

Figure 53. The increased risk to elderly occupants in near side impact is apparent in these figures from Ramachandra et al. 2017. An increased risk of pelvis injury is not especially apparent compared to the head, thorax, and abdomen which seem to be at significantly more risk of injury with age

4.4. Pelvis FE Model Summary

A model of the bony human pelvis with sacroiliac joints and the pubic symphysis was developed and benchmarked for lateral impact conditions. Using the Corvid-CAVEMAN modeling procedures, the pelvis geometry and mesh was constructed to represent a 50th percentile male and meet mesh quality standards. Pelvis cortical and trabecular bone properties were taken from literature, although trabecular bone was found to have poor and wide-ranging characterization. Special developmental effort was given to the pelvic joints. Pubic response was in line with both dynamic and quasi-static load-displacement responses of isolated PMHS pubic joints. The sacroiliac joints were reconstructed to match geometric descriptions and were tuned to match mechanical response reported in literature. This work highlighted a lack of research of into the SIJ pertaining to injurious biomechanics. The model was impacted in replicated loading scenarios from PMHS testing done at UVA. A comparison of force response was initially made based on visual data trace examination. Going further, a new objective rating method was developed that takes into account PMHS variability, and this was performed to confirm the force response was acceptable. Injuries reproduced via element deletion in the pelvis model were consistent with injuries occurring in the PMHS specimen. Further accessory studies were performed on model material properties and possible joint degeneration. The model was most sensitive to changes in trabecular bone, thus the mechanical stiffness of the trabecular bone was adjusted to better fit the test data while staying within the range of values reported in literature. Simulated ossification of pubic and SI joints did not have a significant effect on model response. Based on the work performed in this chapter, the pelvis model is suitable to perform further analysis on side impact injury tolerances and predictive metrics.

CHAPTER 5: INJURY RISK FINITE ELEMENT STUDY

In this chapter, the injury tolerances of the newly developed human pelvis model were examined and injury outcomes based on measureable metrics were compared to those existing in literature. Statistical analysis was performed to construct FE based injury risk functions in both the anterior and posterior lateral impact conditions. Injury threshold analysis was performed with the pelvis FE model to determine whether anterior or posterior force is a better injury predictor. This simulation approach will also identify in which impact the pelvis is more vulnerable to injury: anterior or posterior loading?

5.1. Existing Injury Risk Evaluations of the Pelvis in Lateral Loading

Injury risk functions (IRFs) are valuable tools in predicting the probability of an injury based on a certain measurable metric or set of metrics. Determination of reliable injury metrics that correlate to pelvic fracture during lateral impacts can lead to safer military and commercial vehicles. Existing injury risk functions and previously explored injury metrics will be discussed and analyzed with the pelvis FE model.

A number of IRFs related to the pelvis have been explored in the past 20 or so years, but their usefulness hinges on their ability to accurately correlate injury to measurable criteria. Many of these initial constructed IRF's (Cavanaugh et al. 1990, Zhu et al. 1993, Maltese et al. 2002) used impact force as the metric to predict injury. Cavanaugh et al. 1990 performed 12 side impact sled tests at Wayne State University that impacted a whole body cadaver with a sidewall boundary condition. This test series in particular highlights some of the issues with earlier attempted IRF generation. A "lateral impact" IRF was created from a test series where load was transmitted primarily through the greater trochanter (anterior pelvis) thus not accounting for posterior loading and a range of loading conditions were not considered. Later investigations revealed that impact force as an injury predictor was not consistent over different types of impact conditions.

Leport et al. 2007 developed a PMHS pelvic injury risk curve based on pubic force. A pubic load cell was developed which replaced the pubic symphysis. This was based on the assumption that load going through the pubis was a good predictor of pelvic fracture. Based on the injury patterns and timing of the pelvis, where the anterior side of the pelvis consistently fractured before the posterior side, pubic force as an injury predictor was considered to be valid. Sixteen side impact tests were performed on 8 cadavers using boundary conditions used in sled and impactor tests from the literature. The authors determined ratios based on these tests that translates peak impact force to peak pubic force. Using these ratios (3.3 for impactor tests and 4.6 for sled tests) the pubic forces were calculated from reported impact forces in 90 PMHS cadaver tests from the literature to provide a more extensive sample size. It was determined that pubic force was a consistent injury predictor (Figure 54) across different testing configurations when compared to impact force. A limitation in Leport's study was that the replacement of the cadaveric pubic symphysis with a load cell artificially effects the biofidelity of the pelvis. Another source of potential error includes the inexactness of the determining ratios to translate impactor force to pubic force based on sub-injurious tests. None-the-less, Leport's work suggests that impact force was not a reliable or consistent metric to base injury risk on, due to its variance in different impact configurations.

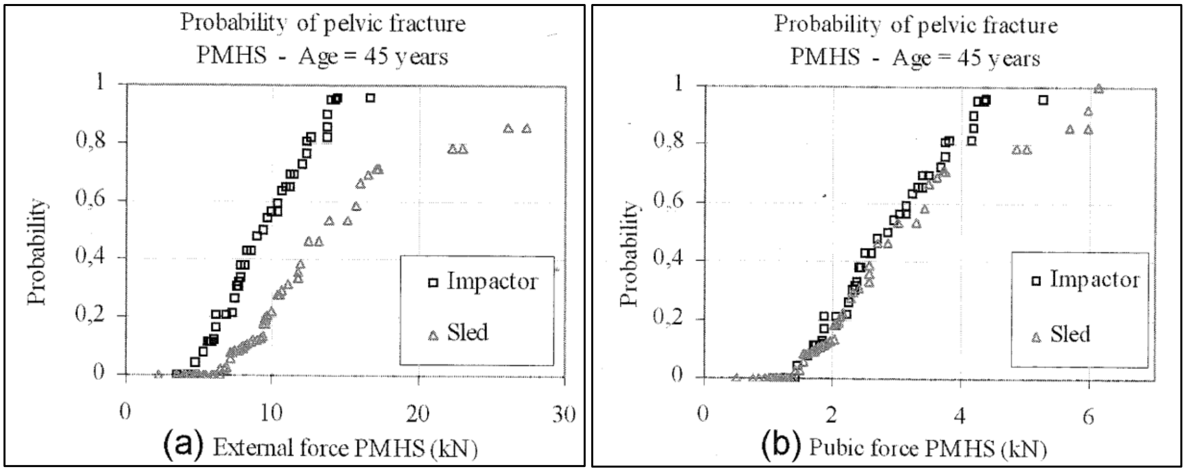

Figure 54. Leport et al. 2007 illustrated that pubic force is a more consistent predictor of injury risk across different types of impacts than impactor force.

Petitjean et al. 2012 published work pertaining to the development of the WorldSID 50th percentile male ATD. The WorldSID (Worldwide Harmonized Side Impact Dummy) is a crash test dummy, which was specifically developed to assess vehicle occupant injury risk during lateral impacts (First Technology, Rev A 2007). The injury risk curves were developed from paired ATD tests and PMHS side impact tests that were available in literature. Petitjean recreated the tests performed in literature with the WorldSID ATD to correlate measured values to injuries reported in cadaveric specimens. Figure 55 illustrates the injury risk curve based on maximum pubic force created in Petitjean et al. 2012 for a 45-year old male. The 95% confidence interval becomes wider as injury risk increases. P-values were not reported, but according to the quality index the authors state this correlation ranges from “marginal” to “fair”. However, one can visually examine Figure 55 and note that there does not seem to be a strong correlation between the maximum pubic force of AIS 2 injured and non-injured pelvises. Still, the pubic force was suggested for use as a predictor of pelvis injury in lateral impact, based on the understood injury mechanism in which anterior pelvis fractures led to posterior injury. Fractures of the ramis and ischium (anterior pelvis) have been observed to occur before posterior sacral fractures.

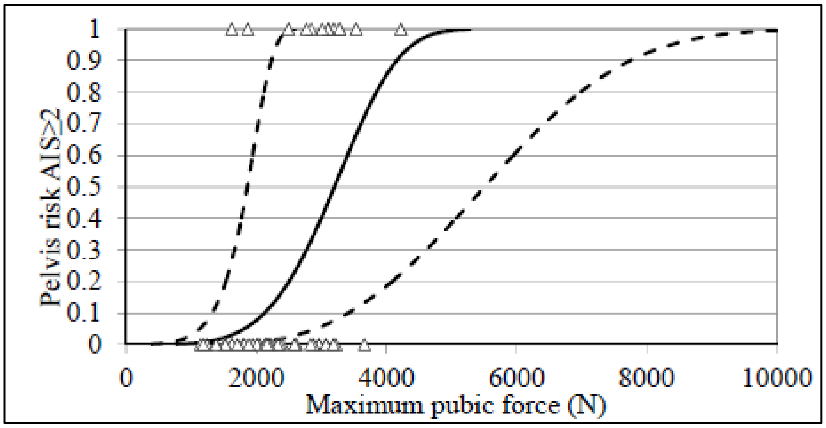

Figure 55. Injury risk curve defined developed for the WorldSID ATD scaled to 45 and 67 year olds considering AIS2+ and AIS3+ injury risk (Petitjean et al. 2012)

Peres et al. 2016 developed injury risk curves that predict pelvic fractures based on global metrics such as force and local metric such as strain using the Total Human Model (THUMS), which is a human body FE model. Peres reproduced a number of PMHS tests using the THUMS model to observe injury indicators and compare the capabilities of the existing IRFs. Injury predictors tested were impactor force, pubic force, and the sum of pubic and SIJ force, as well as maximum principal strain (MPS) of the cortical bone. A limitation in this study is that the authors deactivated bone failure in the model to measure the maximum principal strain of the pelvic cortical bone in each impact. This will have a drastic effect on the biofidelity of the simulation forces since the failure of the pubic ramis were not modeled and thus the closed book fracture behavior of the sacrum does not occur. In the discussion section, Peres acknowledged that impactor force would likely fall apart as a good injury predictor with consideration to variation in impact conditions; to greater trochanter, iliac wing, or both.

Lebarbe et al. 2016 studied the injury mechanism of the sacroiliac joint in lateral impact. It was determined that the pubic area of the pelvis was the weakest and the majority of injuries to this area are caused by failure of the pubis, which correlates well with the results of the computational study in this thesis. Similar analysis performed one-year prior (Petit et al. 2015) examined injury characteristics of the pelvis in lateral impacts and confirmed that SIJ fractures always occur after anterior pelvis fractures. These pure lateral impact cases involve significant loading to both the anterior and posterior pelvis together, and while more load travels through the posterior SIJ, proposed injury metrics do not take into account unevenly distributed loading.

Petit et al. 2018 proposed a major update to the pelvis injury risk criterion related to the WorldSID dummy. Sixty-four lateral impact PMHS tests were reproduced with WorldSID ATD tests, instrumented with a pubic load cell, SIJ load cell, and femur neck load cell. These ATD test result peak forces were paired with injury data from the sample of PMHS tests. Logistic regression was performed in order to determine the best injury prediction metric, p-values were used where the outcome variable were: 1 for an AIS 2 or greater injury and 0 otherwise. These p-values are presented in Table 10. The parameter with the best p-value was peak sacrum Y-Force (0.005), while the peak pubic force p-value was the worst (0.943).

Table 10. P-values assessed using logistic regression show peak sacrum force as a significantly better predictor of pelvic ring injury than peak pubic force (Petit et al. 2018).

Parameter	p-values
Peak Femur Neck Resultant force	0.385
Peak Pubic force	0.943
Peak Sacrum Y-force	0.005
Peak Sacrum Z-moment	0.011

The posterior side sacroiliac force was a better pelvic rink injury predictor than the anterior side pubic force. This finding rejects the conclusions of prior studies (Petit et al. 2015, Lebarbe et al. 2016, Leport et al. 2007, Petitjean et al. 2012) where the pubic force was suggested as the best predictor of pelvic injury. The reasons for this finding include the observed instable rotating of the pubic load cell due to lack of stiffness in ATD bone and because the tests were done in very similar loading conditions (pure lateral). Further statistical analyses were performed to construct updated IRFs and corresponding confidence intervals (Figure 56).

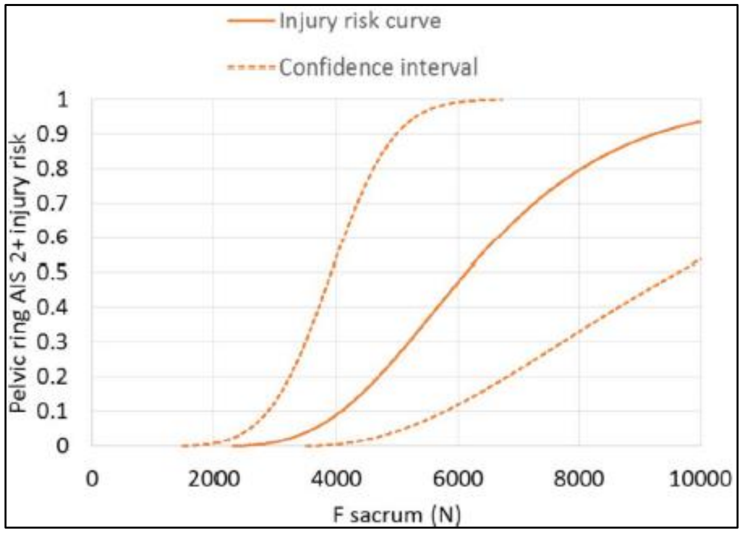

Figure 56. Injury risk curve for AIS 2+ pelvic ring injuries based on peak sacrum force going through the posterior WorldSID pelvis, for a 78kg male aged 45 years. (Petit et al. 2018) Includes age and weight as covariates.

For each of the injury criteria that were proposed, the pelvis was loaded laterally with load going through both the anterior and posterior pelvis. These studies do not examine the different load path distribution during lateral impacts in which the acetabulum and iliac wings are loaded independently of each other. The Salzar test data on an FE model is informative to this injury predictor question because it measures the load going through the anterior and posterior pelvis individually. A hypothesis was made that the force distribution of the pelvis itself in lateral loading conditions is what is causing discrepancies in the determination of a reliable injury predictor.

5.2. Methods

The pelvis FE model was subjected to impacts of varying mass and velocity and injury thresholds were found based on impactor mass and velocity. Peak force was also tracked during these impacts in the anterior and posterior load cells as well as through cross sections of the pubic symphysis and sacrum. A simulation matrix was created consisting of 25 impacts for both the acetabulum and iliac wing impacts. Initial velocity was prescribed across a node set at the top of the impactor surface, while the mass of the impactor was adjusted by changing the density of the impacting structure. This matrix was created in a manner that would capture regions of loading between non-injury and injury, so that injury risk could be defined and injury thresholds determined. In the identification of which portion of the pelvis was more prone to injury, the impactor mass and velocity was used to calculate impact momentum and impact kinetic energy. Momentum being impactor mass times velocity and kinetic energy being one-half mass times velocity squared. The impact condition that took less impactor momentum and energy to fracture the pelvis was described as the more vulnerable case.

To check the feasibility of using anterior and posterior force as injury metrics, logistic regression (Equation 5.2.1) was used to see whether a relationship to injury existed. Pelvic ring injury was defined as being when any elements of cortical bone were deleted (following the 1.5% maximum principal strain criteria).

$$P_{inj} = \frac{e^{a+bx}}{1+e^{a+bx}} \qquad \textbf{\textit{Equation 5.2.1}}$$

To assist in injury metric selection, Akaike Information Criteria (AIC) was used. AIC (Akaike 1974, Yoganandan et al. 2016) has been used in recent studies directly pertaining to developing injury risk curves for the pelvis (Petitjean 2012). In a group of analyzed models, the one with the lowest AIC score was described as being the most accurate, and in this case, the best injury predictor (Equation 5.2.2). L is defined as the maximum likelihood for the candidate model and V is the number of independent variables (V=1).

$$AIC = -2\log(L) + 2V$$ ***Equation 5.2.2***

To better understand the accuracy of the determined AIC, Akaike weights were used (Equation 5.2.3) so that 95% confidence intervals could be generated along with an injury risk curve. This confidence interval was created by summing up the Akaike weights from each unit until the sum is 0.95, while the weight for all is 1.0.

$$w_i(AIC) = \frac{\exp(-0.5\Delta_i(AIC))}{\sum_{i=1}^{K}\exp(-0.5\Delta_i(AIC))}$$ ***Equation 5.2.3***

$$\Delta_i(AIC) = AIC_i - \min AIC$$ ***Equation 5.2.4***

Projecting these 95% confidence intervals provides a better sense of an injury metrics consistency across a range of data. Injury risk functions and the corresponding confidence intervals were constructed using International Organization of Standardization (ISO) outlined procedure (ISO/TR 12350). A Weibull distribution was used (Equation 5.2.5) to construct the s-shaped injury risk function related to each injury predictive metric. Weibull distributions are commonly used in survival analysis, reliability studies, as well as weather forecasting. Statistical analysis was performed in R-studio (3.5.3; 2019-03-11).

$$P_{inj} = 1 - e^{\left(-e^{\left(\frac{1}{b}*\ln(x)-\frac{a}{b}\right)}\right)}$$ ***Equation 5.2.5***

5.3. Injury Evaluation Results

The matrices for the acetabulum and iliac wing impacts were simulated (Table 11 and Table 12). For the acetabulum impacts, impactor mass was varied from 1 kg to 5 kg and initial impact velocity from 1 m/s to 5 m/s. For the iliac wing impacts, impactor mass was varied from 1 kg to 5 kg and initial impact velocity varied from 3 m/s to 7 m/s. The reasoning for the different velocities was due to the lower velocities not causing any element deletion in the iliac wing impact (1, 2, and 3 m/s). Thus, to capture the injurious and non-injurious responses the initial velocities were increased. The peak anterior and posterior force was tracked during each of these simulations. In addition, artificial load cells added to the cross sections of the sacrum and pubic symphysis were included to be more comparable to the instrumentation locations of the WorldSID ATD. However, there was not a significant difference found in the magnitude of the FE determined peak forces observed between the pubic symphysis and anterior load cells, as well as the sacrum and posterior load cells. Since no difference was observed, the experimentally validated traces of the anterior and posterior load cells were used.

Table 11. Acetabulum impact study simulation matrices.

		Pelvic Ring Fracture				
Mass (kg)	5	No	Yes	Yes	Yes	Yes
	4	No	No	Yes	Yes	Yes
	3	No	No	Yes	Yes	Yes
	2	No	No	Yes	Yes	Yes
	1	No	No	No	No	Yes
		1	2	3	4	5
		Velocity (m/s)				

		Anterior Load Cell Force (N)				
Mass (kg)	5	1281	2248	2055	2288	2424
	4	1180	2373	2032	2273	2402
	3	989	1943	2138	2257	2379
	2	776	1601	2498	2216	2234
	1	520	1043	1603	2180	2272
		1	2	3	4	5
		Velocity (m/s)				

		Posterior Load Cell Force (N)				
Mass (kg)	5	859	1612	1928	2076	2183
	4	769	1536	1751	2048	2153
	3	665	1274	1946	1988	2103
	2	546	1049	1607	1907	2053
	1	452	823	1216	1627	1900
		1	2	3	4	5
		Velocity (m/s)				

Table 12. Iliac wing impact study simulation matrices.

		Pelvic Ring Fracture				
Mass (kg)	5	No	Yes	Yes	Yes	Yes
	4	No	No	Yes	Yes	Yes
	3	No	No	Yes	Yes	Yes
	2	No	No	No	No	Yes
	1	No	No	No	No	No
		3	4	5	6	7
		Velocity (m/s)				

		Anterior Load Cell Force (N)				
Mass (kg)	5	147	243	257	434	459
	4	126	184	243	343	430
	3	123	153	221	310	384
	2	114	145	190	261	344
	1	94	123	140	174	216
		3	4	5	6	7
		Velocity (m/s)				

		Posterior Load Cell Force (N)				
Mass (kg)	5	934	1432	1956	2337	2649
	4	928	1220	1661	2046	2332
	3	770	950	1420	1686	2193
	2	575	659	888	1238	1611
	1	374	433	564	724	913
		3	4	5	6	7
		Velocity (m/s)				

The injury thresholds for the pelvis in each impact were observed. Injury was identified as being when any elements of cortical bone were deleted (1.5% MPS). For the acetabulum impact the maximum survivable impactor momentum was 8 kg*m/s, while the iliac impact was 16 kg*m/s. In regards to impactor kinetic energy, the maximum survivable acetabulum impact was 8 joules, while the iliac wing impact was 36 joules. This analysis shows that the pelvis model was more prone to injury during acetabular loading than iliac wing loading (Figure 57). This conclusion was supported by conclusions made in Salzar et al. 2009, and could be better supported if injury severity was considered. Many of the injuries occurring in the acetabular impacts, particularly the higher momentum and energy injuries were quite severe, including ramis, ischium, and closed book sacrum fractures. The iliac wing impacts, on the other hand, mostly had fracture limited to the articular surface of the sacrum. Even in the highest energy iliac wing impact, the structural integrity of the iliac wing was not affected. The geometric topography of the iliac wings themselves appear to give the pelvis a certain level of compliance during wing loading. This compliance does not exist in the acetabular loading cases, the ramis and ischium do not have a great deal of flexibility during the anterior pelvis loading.

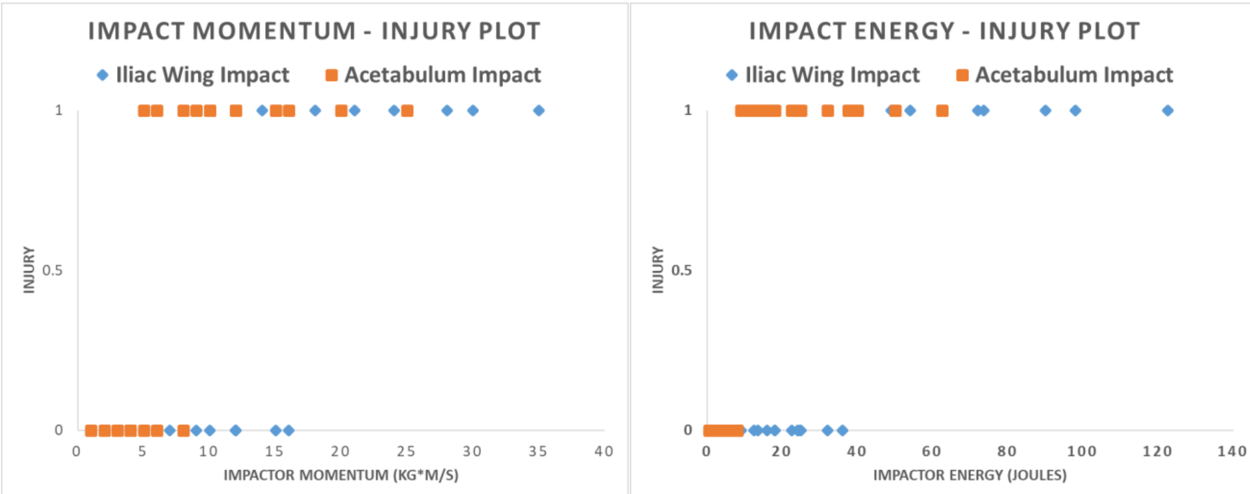

Figure 57. Comparison between anterior and posterior force as pelvis injury predictors in lateral impact. The acetabular cup loading has a lower injury threshold than iliac wing loading.

Based on peak forces tracked during the impactor mass and velocity varying simulations, injury risk analysis was performed. Injury risk functions were generated along with 95% confidence intervals to showcase the injury predictive capability of both anterior and posterior pelvis force (Figure 58). AIC was calculated as 66.69 for anterior force as an injury predictor across both impact conditions. For posterior force's dual impact prediction AIC was calculated to be 24.04. The significantly lower AIC number for posterior force shows that it is a significantly better injury predictor than anterior force. This information is valuable when trying to define an IRF for the pelvis based on a measurable quantity. Examining the anterior force Weibull plot in Figure 58, there exists two clusters of injurious data points: one in the range of 250-500N and the other 2000-2500N. Why are there two prominent clusters? This was traced back to the lateral dynamic force distribution of the pelvis itself. In the acetabulum wing impact, the majority of force is transmitted through the anterior pelvis hence the higher force cluster. However, during iliac wing loading the force was primarily transmitted through the posterior pelvis (over 90%) so very little force goes through the anterior. This low force cluster is extremely misleading and would cause an inaccurate injury risk function. For example, IRFs were created solely from the acetabular and iliac wing impacts (n=25) to understand just how unreliable anterior force is as an injury predictor. For the acetabulum impact based on anterior force, 50% injury risk occurs at 1950N while for the iliac wing impact 50% injury risk occurs at 215N. In comparison for acetabulum impact based on posterior force, 50% injury risk occurs at 1550N while for the iliac wing impact 50% injury risk occurs at 1300N. Posterior force is more consistent across the two extreme case lateral loading scenarios. The range in which anterior force can predict an injury is too wide.

Relating this study back to a more realistic side panel intrusion environment. If a panel intrudes into the pelvis, it is unlikely that it will only impact either the iliac wing or acetabulum. In the average case, it is hypothesized that there would be an intrusion that laterally impacts the pelvis as a whole. This is why in the recent ATD based tests (Petit et al. 2018) to develop IRFs all of the tests impact the entire pelvis laterally. They concluded that posterior force was a better predictor since in their pure lateral loading scenario load goes similarly through the anterior and posterior pelvis. However, this being a conclusion does not hold valid, since it would suggest anterior force would be an equally good predictor. From a force distribution standpoint, the extreme scenarios of either solely acetabular or wing loading that this FE study explores help nail down why exactly posterior force was the better predictor. This study identifies that posterior force can be traced to injury consistently in both the extreme lateral loading cases, those being solely acetabular or solely iliac wing.

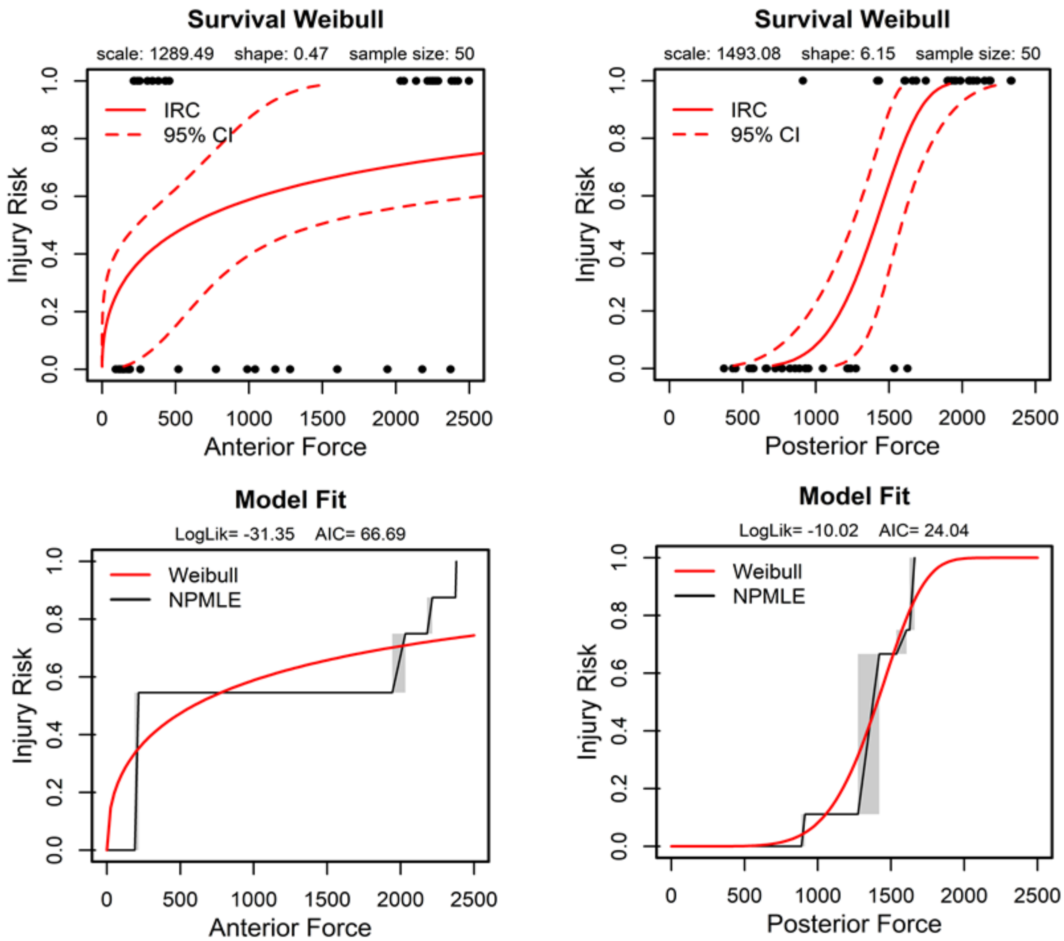

Figure 58. Comparison between anterior and posterior force as pelvis injury predictors in lateral impact. Posterior force is a more consistent injury predictive metric than anterior force.

These generated IRFs should not be taken as true injury risk predictors based on particular force measurements. These generated IRFs were created for the purpose of showing that posterior pelvic force was a better predictor than anterior pelvic force. To generate proper IRFs, ones that are FE derived and trace a specific peak force to an injury probability, further analysis would be needed. How much work would this require? A more comprehensive pelvis model would be needed, one that includes the soft tissues and flesh that were disregarded in this study. Furthermore, a single FE model is not valid to perform an injury risk analysis to represent a population of people. To generate population representative pelvises, mesh morphing techniques and adjustments to material properties would be required to better model such variant population groups.

5.4. Injury Threshold and Predictive Metric Summary

The pelvis FE model was used in an accessory study to evaluate the injury risk metrics and thresholds to the pelvis in lateral impact. Based on the literature review of existing injury risk evaluations done for the human pelvis in lateral impact, there seemed to be a consensus that pubic force would be a good indicator (Petitjean et al. 2012) until Petit et al. 2018 showed not only was sacrum force a better predictor, but that pubic force was a poor one. Conclusions given in Petit were not clear as to why this was the case. Simulation matrices of the Salzar-UVA acetabulum and iliac wing impacts were created where impactor mass and velocity was incrementally changed in order to capture injurious and non-injurious outcomes. Based on these simulation matrices it was determined that the anterior pelvis is more prone to injury than the posterior pelvis. Not only did the FE pelvises in acetabular loading fracture at lower impactor momentum and kinetic energy, but the injuries that occured were more severe than those that occured in iliac wing loading. Statistical analysis was performed in R in order to evaluate anterior force (pubic) and posterior force (sacrum) as injury predictive metrics. Based on computed AIC, posterior force was determined to be a better estimator of pelvis ring fracture than anterior force. Injury risk functions were generated with 95% confidence intervals in order to illustrate the superiority of using posterior force over anterior force to predict injury. These findings were in support of Petit's study using the WorldSID ATD. Encouragingly, the same injury metric conclusion as Petit was reached using a completely different method and means of evaluation.

CHAPTER 6: CONCLUSIONS

This chapter will conclude this graduate thesis. Contributions that this research adds to the field will be specifically addressed and the avenues for future research based on this thesis will be discussed. Limitations related to the methods and assumptions contained in this thesis will be explained.

6.1. Concluding Remarks

The main goals of this master's thesis were stated in Chapter 1 as follows: develop a pelvis FE model using the Corvid-CAVEMAN modeling approach, benchmark the FE model response and injury to experimental PMHS data, and analyze injury thresholds of the FE pelvis to evaluate currently used injury predictive metrics. These tasks were outlined to contribute better scientific understanding in the field of impact biomechanics, directly relating to lateral pelvis loading in military blasts.

Chapter 2 highlighted background information on Corvid Technologies, Velodyne, and the CAVEMAN modeling approach. Prior modeling work related to the lower extremity in UBB accelerative loading was summarized. FE parameter studies performed on the lower extremity showed a hyper sensitivity to the ligamentous connective tissues. Due to the significant role these connective tissues played in the force and injury responses, special consideration was taken in developing the connective joint regions of the CAVEMAN pelvis.

Chapter 3 discussed the development process of the CAVEMAN pelvis model. Pelvis geometry was compared to the defleshed pelvis used in the Salzar pelvis impact test series, in addition to prior comparisons to military handbook described 50th percentile male measurements. Cortical bone thickness was confirmed for both the coxal bones and sacrum with measurements reported in literature. Mesh generation was done using Bolt, and the vast majority of elements (over 94%) met the scaled Jacobian criteria of 0.4. Material properties were taken from literature as they were available. Cortical bone stress-strain response was validated against pelvic bone dynamic tensile tests. Trabecular bone, not being well characterized, was estimated based on the density in the FE model from an empirical equation. Trabecular bone material properties were later optimized based on the results from material parameter studies directly related to dynamic lateral pelvis impacts. Based on the conclusions of Chapter 2, extra effort was given to the connective regions of the pelvis. The pubic symphysis was independently validated against Dakin's isolated joint PMHS tests performed in literature. The sacroiliac joints were reconstructed to match geometric descriptions recently reported in literature. SIJ force-displacement response was measured against Miller's directionally loaded PMHS tests reported in the literature. The material properties of the SIJ ligaments were tuned to best fit the FE response to the cadaveric averages. The modeling efforts related to the SIJ identify a lack of understanding of the biomechanics response of these joints and the need for further experimental characterization of them.

Upon development of the pelvis model, it was subjected to the PMHS testing conditions of the Salzar-UVA test series in Chapter 4. The Salzar test conditions, which consisted of dynamic impacts to a defleshed pelvis at the acetabular cup or iliac wing, were recreated in Velodyne to match experimental conditions. Input velocity traces were directly prescribed to dictate impactor motion. Load cells positioned under the anterior and posterior portions of the pelvis tracked force response as well as the dynamic force distribution of the pelvis in each impact. The dynamic distribution of force was within one standard deviation of those reported in the experimental dataset. The force traces, when plotted against the experimental traces, compared favorably. CORA scoring was used in a PMHS-variability conscious way to better assess the biofidelity of the FE force responses. Cross-correlation scoring was used between each PMHS test to determine an average experimental CORA score from the two load cell readings in each test condition. The model was scored to each individual PMHS test to determine an average model CORA score for each load cell reading. The average model CORA score was within 1 standard deviation of the experimental scores. Two-sample Student's t-tests were performed on these to confirm that the pelvis model's response was not distinguishable from the experimental results. Injuries that were predicted by the pelvis model using maximum principal strain element deletion were comparable to those occurring in the dataset. A material sensitivity study was performed which suggested the model response was most sensitive to trabecular bone stiffness. Based on these results the trabecular bone stiffness was later reduced, as it better fit the experimental data as well as was within range of pelvic trabecular bone properties reported in Dalstra et al. 1993. An accessory study investigating the effect of joint ossification in the pelvis was performed. This was done since it was noted that the pelvises in the Salzar test series were observed to have variable joint flexibility. The results of this study suggested that joint ossification does not affect the response of the human pelvis during lateral impact.

After developing and benchmarking the response of the pelvis model, it was used in an injury threshold analysis in Chapter 5 to evaluate existing injury risk metrics. The pelvis was impacted in the acetabulum and iliac wing impacts at varying impactor masses and initial velocities. The testing matrices consisted of 25 impacts in each impact condition. The matrices were constructed to capture both non-injurious and injurious results. Injury was defined as occurring when any element deletion of the cortical bone was observed. It was determined that the injury tolerances of the pelvis are significantly lower in the anterior pelvis than the posterior pelvis. Based on the results of this finite element analysis and prior cadaveric testing, it is apparent that protection efforts of the pelvis in lateral impacts should be centered around reducing acetabular loading. In military vehicles during, for instance, a VBIED attack intrusion of the vehicular side panels may load the pelvis. Side rails and other panel designs should be designed to avoid making contact with the femoral head during potential lateral loading scenarios. Protecting the femoral head in lateral intrusion events will limit the amount of load traveling through the anterior pelvis, thus reducing injury risk. As was shown in the dynamic force distributions, impacts that are directed through the iliac wing structure only predispose the anterior pelvis to about 10% of the peak load distribution.

A brief literature review in Chapter 5 introduced recent contradictory findings related to an injury prediction metric related to lateral pelvis loading. Research pertaining to the WorldSID side impact ATD had initially suggested using anterior pubic force as an injury predictor (Petitjean et al. 2012) since fracture in pure lateral impact was initiating in the anterior pelvis. More recent findings (Petit et al. 2018) that replicated the PMHS-ATD paired impact tests included a posterior sacral load cell and statistical analysis showed posterior force to be a significantly better injury predictor. Conclusions as to why posterior force was a better injury predictor were not made clear. Statistical analysis was performed on the results from the impact mass/velocity FE study. It was determined that posterior pelvis force through the sacrum was a substantially better injury predictor than anterior pelvis force through the pubic symphysis. This was not an intuitive conclusion when taking into account injury mechanisms of the pelvis in lateral impact. It is understood that failure of the pubic ramis and ischium of the anterior pelvis leads to closed book fractures of the sacrum, so initially there was justification that anterior force would be a better injury predictor. However, based on Petit's ATD tests and the FE analysis performed in this study, it was apparent that posterior force is a more consistent predictor. This conclusion was based on the way force was distributed to the pelvis during lateral loading, and leads to the reasoning that future development of military related ATDs that desire to capture lateral loading response should include load cells in the sacrum.

6.2. Contributions

The contributions of this graduate thesis are as follows:

1. *Provides a framework for development and validation of an FE human pelvis model.*

The structure of the development portion of thesis was arranged so that it can be referenced for future pelvis model development efforts. The cortical bone and pubic symphysis were well characterized in the literature and similar component level validation efforts should be used in other models. Trabecular bone properties were not well characterized from a mechanical property standpoint. Optimization related to these properties can hone in on a more tuned model response. A novel three-dimensional model of the sacroiliac joint was developed and newly described material model parameters were validated from isolated sacroiliac joint tests, including isotropic hyperelastic material properties for interosseous, anterior, and posterior sacroiliac ligaments. These modeling efforts relating to the SIJs were unique in that they used 3-D geometric descriptions of the SIJ ligament complex and used experimental based FE tests to tune ligament response. The high-fidelity meshing schemes used by the CAVEMAN model did well in simulating fracture patterns of human bone.

Based on the biofidelity validation efforts, this model was deemed worthy for evaluation of lateral impact conditions involving the human pelvis. CORA scoring was used in a manner that better takes into account the variability of the PMHS test data. The presented CORA method that uses cross-correlation to individually score the test-to-test data and then compare it test-to-model traces is a transparent evaluation. This CORA method is straightforward for PMHS data comparisons, compared to using CORA the default way and simply displaying a single number to score biofidelity. CORA scoring can easily be misused and CORA scores misinterpreted. For instance, the average PMHS response may not necessarily be a biofidelic response. The scoring and subsequent statistical analysis efforts in this thesis simply determine whether the model response were distinguishable from the set of experimental data. The procedures followed in this thesis can be used in future pelvis model studies.

2. *Yields an injury predictive pelvis FE model, validated for dynamic lateral impact*

The developed and experimentally validated FE model can be used for injurious biomechanical analysis of the human pelvis in lateral impact conditions. This model is a valuable tool in assessment of injurious biomechanics, since its analysis capabilities are faster and cheaper than experimental testing methods. As this model was integrated into the full CAVEMAN human body model, developed for military loading conditions, it will be used to influence design guidelines for PPE and vehicle safety characteristics.

3. *Distinguishes an increased injury vulnerability of the human pelvis in anterior loading.*

An investigation into the injury tolerances of the bony pelvis, using an impactor mass/velocity variation study identified that the anterior pelvis is more predisposed to fracture in lateral impact than the posterior pelvis. This conclusion, based on FE analysis, was further supported in the PMHS tests performed by Salzar-UVA. Posterior pelvis loading was less likely to lead to fracture and the injuries that do occur are less severe than those observed in anterior pelvis loading. For efforts related to protecting the human pelvis in lateral impact, acetabular loading should be limited as much as possible.

4. *Identifies an injury prediction metric that is consistent across different lateral pelvis impact scenarios.*

The injury tolerance study data was used to create model-based injury risk functions. While these injury risk functions do not have intrinsic value by themselves, due to the pelvis being defleshed and limited to a single model, they do provide more information into a recently challenged injury metric related to the WorldSID ATD. This analysis showed that posterior pelvis force is a significantly better injury predictor than anterior pelvis force, in agreement with findings made in Petit et al. 2018. The reason for this counter-intuitive finding was related to the load path distribution in the pelvis. Little load travels through the anterior pelvis during posterior impact, yet during anterior impact a sizable amount of load travels posterior through the sacrum. The study in this thesis considered the two extreme lateral loading conditions of pure anterior and posterior loading through the acetabulum and iliac wings, adding to the pure lateral ATD impacts in Petit. This contribution can influence the design and instrumentation of future develop ATDs, suggesting that load cells be placed in the sacrum, particularly for military loading. Posterior force was shown to be better at generating a defined IRF with tighter confidence intervals.

6.3. Limitations

The limited number of PMHS-pelvis samples in each impact condition are a limitation to the model validation and accessory studies. An increased sample of PMHS impacts would have led to more confidence behind the validated FE pelvis model. The mechanical characterization of trabecular bone, particularly of the pelvis, is another limitation in this study. Further experimental tests on trabecular bone especially involving the post yield behavior of trabecular bone, would be beneficial to this field of study. Rate dependent behavior of trabecular bone is not well defined, and it is hypothesized that rate effects are especially evident in trabecular bone (Xie et al. 2017).

The scarcity of PMHS test data that mechanically characterizes the sacroiliac joints limits the ability to fully understand the biomechanics of the SIJ structure.

Another experimental related limitation to this study is the range of velocities in which the pelvises were impacted. Lebarbe et al. 2012 investigated the effect of lateral IED blast related to panel intrusion into the human shoulder. The loading conditions used by Lebarbe to represent this scenario consisted of high velocity (27 m/s) and short duration impacts, compared to the current PMHS study impacting between 3-4 m/s. However, velocity itself is not a good indicator of an impact scenario, one must also consider other boundary conditions. Boundary conditions between the current study and Lebarbe's study were different in that the present lateral pelvis impacts had a rigid boundary conditions while Lebarbe's PMHS subjects were permitted to freely translate after impact. While the loading conditions and boundary conditions in the present study were quite serious, they may not properly represent a true lateral panel intrusion from an IED blast.

The method for fracture modeling was another limitation, and one that is common in other human body FE models. Current bone fracture modeling methods simply delete the element that exceeds a failure threshold (in this case, maximum principle strain). The disappearance of bone materials is not realistic and may negatively affect the post-injury biofidelity of human body models. This can have an adverse effect on prediction of secondary injuries in FE models, such as when a particular injury mechanism is tied to an earlier occurring fracture. Having a higher resolution mesh does help control how rapidly bone is deleted from a simulation from a volume standpoint.

6.4. Future Research Directions

The primary future direction of this research is implementation of this developed pelvis subsystem model into the encompassing CAVEMAN human body model. As CAVEMAN continues to develop and have its subsystems validated, it will be used for full body injury evaluations in blast events. This pelvis model will be evaluated in other loading conditions, outside of the realm of side impact. Preliminary evaluations of the performance of this defleshed model added to a larger sub-assembly subject to under body blast type loading conditions are underway. So far these results show good corroboration of injury data with the PMHS data series, but are lacking in the vertical force transmission signals. It is hypothesized that further sacroiliac joint complex understanding is needed. The vertical orientation of the outermost posterior SIJ ligaments was not included in this analysis, as well as the accessory SIJ ligaments.

This thesis identifies a potential need for PMHS cadaveric testing of the SIJ structure in high rate loading. So far there are just two isolated SIJ cadaveric test series available in literature from the late 1980's and these are both quasi-static load-displacement studies. The accuracy of existing pelvis FE models is limited by this lack of experimental data. FE simulations run at UVA involving the pelvis in UBB loading conditions (Greenlaugh M.S. Thesis 2019), suggested that the sacroiliac joints play a sizeable role in model response. Improving the biomechanical understanding of the sacroiliac joints through experimental means will improve the correctness of human body FE models. Additional testing could also include different boundary and loading conditions, such as the high velocity free boundary condition lateral impacts performed in Lebarbe et al. 2012. Different boundary conditions and impact velocities could lead to a different injury mechanism or failure threshold.

Development of future ATDs that evaluate lateral loading should consider that force traveling through the posterior pelvis as a better injury predictor than anterior loads. The methods used in the injury threshold study could be repeated on other body regions where there exists question involving the validity of currently used injury metrics. Further analysis of lateral loading should consider oblique loads, angled outside of pure lateral impact, and their effects on the human pelvis.

Creation of useful model derived injury risk functions is another future direction this research could move toward. Side impacts to the pelvis on population specific models could provide a well-ranged description of injury risk. This would involve tuning of material properties to describe age groups and sexes, as well as mesh morphing techniques to adjust the physical representation of the pelvis. Such model-derived IRFs have been previously developed at UVA for the human femur in three-point bending (Park et al. 2017).

Most importantly, this research can contribute to the future mission of improving warfighter safety. As VBIEDs continue to be a potential threat in future conflicts, understanding the consequence of a lateral blast loading toward a military vehicle will be further studied. This pelvis model will be valuable in evaluating the protection capabilities of military vehicles for lateral pelvis loads. Potential work involves implementing the pelvis FE model into a vehicle design and simulating side panel intrusion into the pelvis. Understanding pelvis injury mechanisms and tolerances is necessary to identify the level and direction of future protection design.

REFERENCES

Akaike, H. 1974. “A New Look at the Statistical Model Identification.” *IEEE Transactions on Automatic Control* 19 (6): 716–23.

Akrami, Mohammad, Zhihui Qian, Zhemin Zou, David Howard, Chris J Nester, and Lei Ren. 2018. “Subject-Specific Finite Element Modelling of the Human Foot Complex during Walking: Sensitivity Analysis of Material Properties, Boundary and Loading Conditions.” *Biomechanics and Modeling in Mechanobiology* 17 (2): 559–76.

Anderson, Andrew E., Christopher L. Peters, Benjamin D. Tuttle, and Jeffrey A. Weiss. 2005. “Subject-Specific Finite Element Model of the Pelvis: Development, Validation and Sensitivity Studies.” *Journal of Biomechanical Engineering* 127 (3): 364.

Arun, Mike W. J., Sagar Umale, John R. Humm, Narayan Yoganandan, Prasanaah Hadagali, and Frank A. Pintar. 2016. “Evaluation of Kinematics and Injuries to Restrained Occupants in Far-Side Crashes Using Full-Scale Vehicle and Human Body Models.” *Traffic Injury Prevention* 17 (sup1): 116–23.

Bailey, James R., Daniel J. Stinner, Lorne H. Blackbourne, Joseph R. Hsu, and Michael T. Mazurek. 2011. “Combat-Related Pelvis Fractures in Nonsurvivors:” *The Journal of Trauma: Injury, Infection, and Critical Care* 71 (supplement): S58–61.

Bailey, Ann 2016. “Injury Assessment for the Human Foot/Leg Exposed to Axial Impact Loading.” *UVA Center for Applied Biomechanics PhD Dissertation*.

Becker, Ines, Stephanie J. Woodley, and Mark D. Stringer. 2010. “The Adult Human Pubic Symphysis: A Systematic Review: The Pubic Symphysis.” *Journal of Anatomy* 217 (5): 475–87.

Beilas et al. 2001. “Lower Limb: Advanced FE Model and New Experimental Data.” *Stapp Car Crash Journal* Vol. 45 pp. 469-494.

Butz, Kent, Chad Spurlock, Rajarshi Roy, Cameron Bell, Paul Barrett, Aaron Ward, Xudong Xiao, Allen Shirley, Colin Welch, and Kevin Lister. 2017. “Development of the CAVEMAN Human Body Model: Validation of Lower Extremity Sub-Injurious Response to Vertical Accelerative Loading.”

Cavanaugh et al. 1990. “Biomechanical Response and Injury Tolerance of the Pelvis in Twelve Sled Side Impacts.” *Wayne State University* 902305.

Chen, H., Poulard, D., Forman, J., Crandall, J., & Panzer, M. B. (2018). Evaluation of geometrically personalized THUMS pedestrian model response against sedan–pedestrian PMHS impact test data. Traffic injury prevention, 19(5), 542-548.

Cheung, Jason Tak-Man, Ming Zhang, Aaron Kam-Lun Leung, and Yu-Bo Fan. 2005. "Three-Dimensional Finite Element Analysis of the Foot during Standing—a Material Sensitivity Study." *Journal of Biomechanics* 38 (5): 1045–54.

Dalstra et al. 1995. "Development and Validation of a Three-Dimensional Finite Element Model of the Pelvic Bone." *ASME 1991* Vol.117 pp 272-278.

Dakin, Greg J., Raul A. Arbelaez, Fred J. Molz, Jorge E. Alonso, Kenneth A. Mann, and Alan W. Eberhardt. 2001. "Elastic and Viscoelastic Properties of the Human Pubic Symphysis Joint: Effects of Lateral Impact Loading." *Journal of Biomechanical Engineering* 123 (3): 218.

Davis, Jana M., Daniel J. Stinner, James R. Bailey, James K. Aden, and Joseph R. Hsu. 2012. "Factors Associated With Mortality in Combat-Related Pelvic Fractures:" *Journal of the American Academy of Orthopaedic Surgeons* 20: S7–12.

DoD Blast Injury Research Program Coordinating Office "Prevention, Mitigation, and Treatment of Blast Injuries." *FY14 Report to the Executive Agent Science and Technology Efforts and Programs.*

Eichenseer, Paul H., Daryl R. Sybert, and John R. Cotton. 2011. "A Finite Element Analysis of Sacroiliac Joint Ligaments in Response to Different Loading Conditions:" *Spine* 36 (22): E1446–52.

Eskridge, Susan L., Caroline A. Macera, Michael R. Galarneau, Troy L. Holbrook, Susan I. Woodruff, Andrew J. MacGregor, Deborah J. Morton, and Richard A. Shaffer. 2012. "Injuries from Combat Explosions in Iraq: Injury Type, Location, and Severity." *Injury* 43 (10): 1678–82.

Fressmann, Dirk, Thomas Münz, Oliver Graf, and Karl Schweizerhof. 2007. "FE Human Modelling in Crash – Aspects of the Numerical Modelling and Current Applications in the Automotive Industry." *LS*, 12.

Gabler, Panzer, and Salzar. 2014 "High-Rate Mechanical Properties of Human Heel Pad for Simulation of a Blast Loading Condition." *IRCOBI CONFERENCE* IRC-14-87 pp 796-808.

Gayzik, F Scott, Daniel P Moreno, Nicholas A Vavalle, Ashley C Rhyne, and Joel D Stitzel. n.d. "Development of the Global Human Body Models Consortium Mid- Sized Male Full Body Model," 11.

Gehre, Christian, and Heinrich Gades. n.d. “OBJECTIVE RATING OF SIGNALS USING TEST AND SIMULATION RESPONSES,” 8.

Guillemot, HervC, and Claude Got. n.d. “PELVIC BEHAVIOR IN SIDE COLLISIONS: STATIC AND DYNAMIC TESTS ON ISOLATED PELVIC BONES,” 13.

Hallquist, John 2006. “LS-Dyna Theory Manual.” *Livermore Software Technology Corporation* ISBN: 0-9778540-0-0.

Hammer, Niels, and Stefan Klima. 2019. “In-Silico Pelvis and Sacroiliac Joint Motion—A Review on Published Research Using Numerical Analyses.” *Clinical Biomechanics* 61 (January): 95–104.

Hammer, Niels, Hanno Steinke, Uwe Lingslebe, Ingo Bechmann, Christoph Josten, Volker Slowik, and Jörg Böhme. 2013. “Ligamentous Influence in Pelvic Load Distribution.” *The Spine Journal* 13 (10): 1321–30.

Hewitt, John, Farshid Guilak, Richard Glisson, and T. Parker Vail. 2001. “Regional Material Properties of the Human Hip Joint Capsule Ligaments.” *Journal of Orthopaedic Research* 19 (3): 359–64.

Irvine, John A, James D Martin, and Gregory T Beck. n.d. “Does the MRAP Meet the US Army’s Needs as the Primary Method of Protecting Troops from the IED Threat.” 90.

ISO/TR 12350. 2013. “Road vehicles – Injury risk curves for the evaluation of occupant protection in side impact tests.” *ISO/TR 12350 2ND ED.*

Hugo Kaaman 2019 “Car Bombs As Weapons of War: ISIS’s Development of SVBIEDs 2014-2019” *Middle East Institute*

Kotwal et al. 2016 “The Effecet of a Golden Hour Policy on the Morbidity and Mortality of Combat Casualties” *JAMA Surg.* pp 15-24.

Jajić, Z., I. Jajić, and S. Grazio. 2000. “Radiological Changes of the Symphysis in Ankylosing Spondylitis.” *Acta Radiologica* 41 (4): 307–9.

Jastrzebski et al. 2017. “Development of Morphed Ribcage Finite Element Models for Comparison with PMHS Data.” *IRCOBI CONFERENCE 2017* IRC-17-07 pp 745-747.

Joukar 2017. “Gender Specific Sacroiliac Joint Biomechanics: A Finite Element Study.” *Master’s Thesis University of Toledo.*

Kemper, Andrew R, Craig McNally, and Stefan M Duma. 2008. “DYNAMIC TENSILE MATERIAL PROPERTIES OF HUMAN PELVIC CORTICAL BONE,” 6.

Kikuchi and Takahashi 2006. “Development of a Finite Element Model for Pedestrian Pelvis and Lower Limb.” *SAE International 2006* ISN 0148-7191.

Kumar et al. 1991. “The Calcaneus Normal and Abnormal.” *Radiographic 1991* 11:415-440

Kura, Hideji, Harold B. Kitaoka, Zong-Ping Luo, and Kai-Nan An. 1998. “Measurement of Surface Contact Area of the Ankle Joint.” *Clinical Biomechanics* 13 (4–5): 365–70.

Lebarbé, Matthieu, Pascal Baudrit, Pascal Potier, Philippe Petit, Xavier Trosseille, Sabine Compigne, Mitsutoshi Masuda, Takumi Fujii, and Richard Douard. 2016. “Investigation of Pelvic Injuries on Eighteen Post Mortem Human Subjects Submitted to Oblique Lateral Impacts.”

Lebarbé, M, A Petitjean, P Baudrit, and D Lafont. 2012. “Protection of Armored Vehicle Occupants - Towards a New Shoulder Injury Criterion Adapted to the Dynamics of Lateral IED Blasts,” 12.

Leport, Baudrit, et al. 2007. “Assessment of the Pubic Force as a Pelvic Injury Criterion in Side Impact.” *Stapp Car Crash Journal* Vol. 51 pp. 467-487.

Li, Zuoping, Jorge E. Alonso, Jong-Eun Kim, James S. Davidson, Brandon S. Etheridge, and Alan W. Eberhardt. 2006. “Three-Dimensional Finite Element Models of the Human Pubic Symphysis with Viscohyperelastic Soft Tissues.” *Annals of Biomedical Engineering* 34 (9): 1452–62.

Li, Zuoping, Matthew W. Kindig, Jason R. Kerrigan, Richard W. Kent, and Jeff R. Crandall. 2013. “Development and Validation of a Subject-Specific Finite Element Model of a Human Clavicle.” *Computer Methods in Biomechanics and Biomedical Engineering* 16 (8): 819–29.

Lindsey, Derek P., Ali Kiapour, Scott A. Yerby, and Vijay K. Goel. 2015. “Sacroiliac Joint Fusion Minimally Affects Adjacent Lumbar Segment Motion: A Finite Element Study.” *International Journal of Spine Surgery* 9 (November).

Lyman, S. 2002. “Older Driver Involvements in Police Reported Crashes and Fatal Crashes: Trends and Projections.” *Injury Prevention* 8 (2): 116–20.

Maltese, Matthew R., Rolf H. Eppinger, Heather H. Rhule, Bruce R. Donnelly, Frank A. Pintar, and Narayan Yoganandan. 2002. “Response Corridors of Human Surrogates in Lateral Impacts.” In.

Miller, J. A. A., A. B. Schultz, and G. B. J. Andersson. 1987. “Load-Displacement Behavior of Sacroiliac Joints.” *Journal of Orthopaedic Research* 5 (1): 92–101.

Mo, Fuhao, Fan Li, Michel Behr, Zhi Xiao, Guanjun Zhang, and Xianping Du. 2018. “A Lower Limb-Pelvis Finite Element Model with 3D Active Muscles.” *Annals of Biomedical Engineering* 46 (1): 86–96.

Morris, Andrew, Ruth Welsh, and Ahamedali Hassan. 2003. “Requirements for the Crash Protection of Older Vehicle Passengers.” *Annual Proceedings / Association for the Advancement of Automotive Medicine* 47: 165–80.

Morris, Julia E. n.d. “2012 Anthropometric Survey of U.S. Army Personnel: Methods and Summary Statistics,” 454.

Nie, B., Crandall, J. R., & Panzer, M. B. (2017). Computational investigation of the effects of knee airbag design on the interaction with occupant lower extremity in frontal and oblique impacts. Traffic injury prevention, 18(2), 207.

Ombregt, Ludwig. 2013. “Applied Anatomy of the Sacroiliac Joint.” In *A System of Orthopaedic Medicine*, e233–38. Elsevier.

Panzer, M. B., Fice, J. B., & Cronin, D. S. (2011). Cervical spine response in frontal crash. Medical engineering and physics, 33(9), 1147-1159.

Penn-Barwell, Jowan G. et al. 2014. “The incidence of pelvis fractures with traumatic lower limb amputation in modern warfare due to improvised explosive devices.” *Journal of the Royal Navy Medical Service* pp 152-156.

Peres, J, S Auer, and N Praxl. 2016. “Development and Comparison of Different Injury Risk Functions Predicting Pelvic Fractures in Side Impact for a Human Body Model,” 18.

Petit, Philippe, Xavier Trosseille, Mathieu Lebarbé, Pascal Baudrit, Pascal Potier, Sabine Compigne, Mitsutoshi Masuda, Akira Yamaoka, Tsuyoshi Yasuki, and Richard Douard. 2015. “A Comparison of Sacroiliac and Pubic Rami Fracture Occurrences in Oblique Side Impact Tests on Nine Post Mortem Human Subjects.” In .

Petit, Philippe, Xavier Trosseille, Matthieu Lebarbé, Pascal Baudrit, Sabine Compigne, Takuma Kawai, Takumi Fujii, Kenichiro Koshizako, and Mitsutoshi Masuda. 2018. “Update of the WorldSID 50th Male Pelvic Injury Criterion and Risk Curve.” In .

Petitjean, Audrey, Xavier Trosseille, Norbert Praxl, David Hynd, and Annette Irwin. 2012. “Injury Risk Curves for the WorldSID 50th Male Dummy.” *Stapp Car Crash Journal*, 25.

Portier et al. 1997. “Dynamic Biomechanical Dorsiflexion Responses and Tolerances of the Ankle Joint Complex.” *SAE, Inc.* pp. 207-224.

Quapp, K. M., and J. A. Weiss. 1998. “Material Characterization of Human Medial Collateral Ligament.” *Journal of Biomechanical Engineering* 120 (6): 757.

Ramachandra et al. 2017. “Injury Patterns of Elderly Occupants Involved in Side Crashes.” *IRCOBI CONFERENCE 2017* IRC-17-21 pp. 113-115.

Ramasamy, Major Arul, Captain Adam M Hill, Spyridon Masouros, Lieutenant-Colonel Iain Gibb, Lieutenant-Colonel Rhodri Phillip, Anthony MJ Bull, and Colonel Jon C Clasper. 2013.

“Outcomes of IED Foot and Ankle Blast Injuries:” *The Journal of Bone and Joint Surgery-American Volume* 95 (5): e25-1–7.

Richards, Andrew M., Nathan W. Coleman, Trevor A. Knight, Stephen M. Belkoff, and Simon C. Mears. 2010. “Bone Density and Cortical Thickness in Normal, Osteopenic, and Osteoporotic Sacra.” *Journal of Osteoporosis* 2010: 1–5.

Rosatelli, Alessandro L, Anne M Agur, and Sam Chhaya. 2006. “Anatomy of the Interosseous Region of the Sacroiliac Joint.” *RESEARCH REPORT* 36 (4): 9.

Sabry et al. 2000. “Internal Architecture of the Calcaneus: Implications for Calcaneus Fractures.” *Foot and Ankle International* Univ. Toledo pp. 114-118.

Salzar, R. S., D. Genovese, C. R. Bass, J. R. Bolton, H. Guillemot, A. M. Damon, and J. R. Crandall. 2009. “Load Path Distribution within the Pelvic Structure under Lateral Loading.” *International Journal of Crashworthiness* 14 (1): 99–110.

Sarajlić, Nermin, and Anisa Gradaščević. 2012. “Morphological Characteristics of Pubic Symphysis for Age Estimation of Exhumed Persons.” *Bosnian Journal of Basic Medical Sciences* 12 (1): 51–54.

Simonian et al. 1997. “The unstable iliac fracture: a biomechanical evaluation of internal fixation.” *Elsevier: Injury* Vol. 28, No 7. Pp. 469-475.

Schleifenbaum, Stefan, Torsten Prietzel, Carsten Hädrich, Robert Möbius, Freddy Sichting, and Niels Hammer. 2016. “Tensile Properties of the Hip Joint Ligaments Are Largely Variable and Age-Dependent – An in-Vitro Analysis in an Age Range of 14–93 Years.” *Journal of Biomechanics* 49 (14): 3437–43.

Shi, Dufang, Fang Wang, Dongmei Wang, Xiaoqin Li, and Qiugen Wang. 2014. “3-D Finite Element Analysis of the Influence of Synovial Condition in Sacroiliac Joint on the Load Transmission in Human Pelvic System.” *Medical Engineering & Physics* 36 (6): 745–53.

Shin, Jaeho, Neng Yue, and Costin D. Untaroiu. 2012. “A Finite Element Model of the Foot and Ankle for Automotive Impact Applications.” *Annals of Biomedical Engineering* 40 (12): 2519–31.

Song, Bo, Weinong Chen, Yun Ge, and Tusit Weerasooriya. 2007. “Dynamic and Quasi-Static Compressive Response of Porcine Muscle.” *Journal of Biomechanics* 40 (13): 2999–3005.

Song, Eric, Laurent Fontaine, Xavier Trosseille, and Hervé Guillemot. n.d. “PELVIS BONE FRACTURE MODELING IN LATERAL IMPACT,” 13.

Steinke, Hanno, Niels Hammer, Volker Slowik, Jörg Stadler, Christoph Josten, Jörg Böhme, and Katharina Spanel-Borowski. 2010. "Novel Insights Into the Sacroiliac Joint Ligaments:" *Spine* 35 (3): 257–63.

Tilvawala, Khushali, Kailash Kothari, and Rupal Patel. 2018. "Sacroiliac Joint: A Review." *Indian Journal of Pain* 32 (1): 4.

Three-M Technologies. "E-A-R Confor EG Foams Material Summary Sheet 50." *Aearo Technologies*

Untaroiu, Costin D., Robert S. Salzar, Hervé Guillemot, and Jeff R. Crandall. 2008. "The Strain Distribution and Force Transmission Path Through Pubic Rami During Lateral Pelvic Impacts." In *Volume 17: Transportation Systems*, 79–88. Boston, Massachusetts, USA: ASME.

Ursano, Robert J., Ronald C. Kessler, James A. Naifeh, Holly Herberman Mash, Carol S. Fullerton, Paul D. Bliese, Alan M. Zaslavsky, et al. 2017. "Risk of Suicide Attempt Among Soldiers in Army Units with a History of Suicide Attempts." *JAMA Psychiatry* 74 (9): 924.

Vavalle, Nicholas A., Daniel P. Moreno, Ashley C. Rhyne, Joel D. Stitzel, and F. Scott Gayzik. 2013. "Lateral Impact Validation of a Geometrically Accurate Full Body Finite Element Model for Blunt Injury Prediction." *Annals of Biomedical Engineering* 41 (3): 497–512.

Vleeming, A, M D Schuenke, A T Masi, J E Carreiro, L Danneels, and F H Willard. 2012. "The Sacroiliac Joint: An Overview of Its Anatomy, Function and Potential Clinical Implications." *Journal of Anatomy* 221 (6): 537–67.

Wilson, Clay. n.d. "Improvised Explosive Devices (IEDs) in Iraq: Effects and Countermeasures," 7.

Xie, Shuqiao, Krishnagoud Manda, Robert J. Wallace, Francesc Levrero-Florencio, A. Hamish R. W. Simpson, and Pankaj Pankaj. 2017. "Time Dependent Behaviour of Trabecular Bone at Multiple Load Levels." *Annals of Biomedical Engineering* 45 (5): 1219–26.

Yoganandan, Narayan, Anjishnu Banerjee, Fang-Chi Hsu, Cameron R. Bass, Liming Voo, Frank A. Pintar, and F. Scott Gayzik. 2016. "Deriving Injury Risk Curves Using Survival Analysis from Biomechanical Experiments." *Journal of Biomechanics* 49 (14): 3260–67.

Yoganandan, Narayan, Frank A. Pintar, Brian D. Stemper, Thomas A. Gennarelli, and John A. Weigelt. 2007. "Biomechanics of Side Impact: Injury Criteria, Aging Occupants, and Airbag Technology." *Journal of Biomechanics* 40 (2): 227–43.

Zhang, Kai, Libo Cao, Abeselom Fanta, Matthew P. Reed, Mark Neal, Jenne-Tai Wang, Chin-Hsu Lin, and Jingwen Hu. 2017. “An Automated Method to Morph Finite Element Whole-Body Human Models with a Wide Range of Stature and Body Shape for Both Men and Women.” *Journal of Biomechanics* 60 (July): 253–60.

Zhao, Jay, and Gopal Narwani. n.d. “Development of a Human Body Finite Element Model for Restraint System R&D Applications,” 13.

Zhu et al. 1993. “Pelvic Biomechanical Response and Padding Benefits in Side Impact Based on a Cadaveric Test Series” *Wayne State University* 933128.

APPENDIX A: CAVEMAN LOWER EXTREMITY MATERIAL DESCRIPTIONS

Table 13. Material model formulations and parameters used in the CAVEMAN lower extremity FE model.

Material Model	Formulation	Tissue Type	Coefficients
Elastic-Plastic Model	$\boldsymbol{\sigma} = E\boldsymbol{\varepsilon}, \quad \lVert\boldsymbol{\sigma}\rVert \leq \boldsymbol{\sigma}_0$ $\boldsymbol{\sigma}_y = \boldsymbol{\sigma}_0 + \frac{EE_T}{E - E_T}\bar{\boldsymbol{\varepsilon}}^p \quad \lVert\boldsymbol{\sigma}\rVert > \boldsymbol{\sigma}_0$	Cortical Bone	$\rho = 2.0\frac{g}{cm^3}$ $\boldsymbol{\sigma}_0 = 140\ MPa$ $E_T = 5.29\ GPa$ $E = 17.5\ GPa$
		Cancellous Bone	$\rho = 1.1\frac{g}{cm^3}$ $\boldsymbol{\sigma}_0 = 8.564\ MPa$ $E_T = 961\ MPa$ $E = 445\ MPa$
		Calcaneus Cancellous Bone	$\rho = 1.1\frac{g}{cm^3}$ $\boldsymbol{\sigma}_0 = 0.544\ MPa$ $E_T = 61.1\ MPa$ $E = 70\ MPa$
Linear Elastic Solid	$\boldsymbol{\sigma} = E\boldsymbol{\varepsilon}$	Ligament	$\rho = 1\frac{g}{cm^3}$ $E = 467\ MPa$ $\nu = 0.48$
Linear Elastic Shell	$\boldsymbol{\sigma} = E\boldsymbol{\varepsilon}$	Fascia	$\rho = 1\frac{g}{cm^3}$ $E = 60\ MPa$ $\nu = 0.3$
		Skin	$\rho = 1\frac{g}{cm^3}$ $E = 300\ kPa$ $\nu = 0.495$
Neo Hookean	$W = C_1(I_1 - 3)$	Cartilage	$\rho = 1\frac{g}{cm^3}$ $C_1 = 4.00\ MPa$ $\nu = 0.495$
Odgen Viscoelastic Model	$\boldsymbol{\sigma} = \boldsymbol{\sigma}_{hyper} + \boldsymbol{\sigma}_{visco}$ $\boldsymbol{\sigma}_{hyper} = \frac{1}{J}\boldsymbol{F}\left\{\frac{\partial W}{\partial \boldsymbol{E}}(\boldsymbol{E}(\tau))\right\}\boldsymbol{F}^T$ $\boldsymbol{\sigma}_{visco} = \frac{1}{J}\boldsymbol{F}\left\{\int_0^t\left[\sum_{i=1}^{6}\gamma_i e^{-(t-\tau)/T_i}\right]\frac{\partial W}{\partial \boldsymbol{E}}(\boldsymbol{E}(\tau))d\tau\right\}\boldsymbol{F}^T$ $W_{Ogden} = \sum_{m=1}^{n}\left\{\frac{\mu_m}{\alpha_m}\left[J^{-\alpha_m/3}\left(\lambda_1^{\alpha_m} + \lambda_2^{\alpha_m} + \lambda_3^{\alpha_m} - 3\right)\right]\right\} + \frac{K}{2}(J-1)^2$	Heel Pad and Fat	$\mu_1 = 107.7\ kPa$ $\alpha_1 = 3.350$ $\mu_2 = -482.8\ kPa$ $\alpha_2 = 1.636$ $K = 693\ kPa$ $\mu_3 = 120.5\ kPa$ $\alpha_3 = 4.221$ $T_1 = 0.538\ s$ $\gamma_1 = 0.215\ s^{-1}$ $T_2 = 2.45e-03\ s$ $\gamma_2 = 1.778\ s^{-1}$ $T_3 = 1.46e-03\ s$ $\gamma_3 = 1.926\ s^{-1}$ $T_4 = 9.50e-04\ s$ $\gamma_4 = 1.610\ s^{-1}$ $T_5 = 7.20e-05\ s$ $\gamma_5 = 1.782\ s^{-1}$ $T_6 = 8.76e-06\ s$ $\gamma_6 = 0.306\ s^{-1}$
Odgen Viscoelastic Model	$\boldsymbol{\sigma} = \boldsymbol{\sigma}_{hyper} + \boldsymbol{\sigma}_{visco}$ $\boldsymbol{\sigma}_{hyper} = \frac{1}{J}\boldsymbol{F}\left\{\frac{\partial W}{\partial \boldsymbol{E}}(\boldsymbol{E}(\tau))\right\}\boldsymbol{F}^T$ $\sigma_{visco} = \frac{1}{J}F\left\{\int_0^t[A_1 + A_2(I_2 - 3)]\left[\sum_{i=1}^{6}G_i e^{-(t-\tau)/T_i}\right]\dot{E}(\tau)d\tau\right\}F^T$ $W_{Ogden} = \sum_{m=1}^{n}\left\{\frac{\mu_m}{\alpha_m}\left[J^{-\alpha_m/3}\left(\lambda_1^{\alpha_m} + \lambda_2^{\alpha_m} + \lambda_3^{\alpha_m} - 3\right)\right]\right\} + \frac{K}{2}(J-1)^2$	Muscle	$\mu_1 = 9.52\ kPa$ $\alpha_1 = 2$ $K = 2.5\ MPa$ $\mu_2 = -4.48\ kPa$ $\alpha_2 = -2$ $T_1 = 16.865\ s$ $G_1 = 31.10\ kPa$ $T_2 = 4.81e-02\ s$ $G_2 = 5.14\ kPa$ $A_1 = 1.000$ $T_3 = 9.29e-03\ s$ $G_3 = 12.71\ kPa$ $A_2 = 0.089$ $T_4 = 1.30e-04\ s$ $G_4 = 43.41\ kPa$ $T_5 = 9.91e-06\ s$ $G_5 = 976.94\ kPa$ $T_6 = 6.23e-07\ s$ $G_6 = 652.16\ kPa$
Transversely Isotropic Hyperelastic Model	$\boldsymbol{\sigma} = \boldsymbol{\sigma}_{hyper}$ $\boldsymbol{\sigma}_{hyper} = \frac{1}{J}\boldsymbol{F}\left\{\frac{\partial W}{\partial \boldsymbol{E}}(\boldsymbol{E}(\tau))\right\}\boldsymbol{F}^T$ $W_{Mat44} = C_1(\tilde{I}_1 - 3) + C_2(\tilde{I}_2 - 3) + F(\lambda) + \frac{K}{2}(\ln J)^2$	Tendon	$\rho = 1\frac{g}{cm^3}$ $K = 5\ GPa$ $C_1 = 4.6\ MPa$ $C_2 = 0.0$ $C_3 = 2.7\ MPa$ $\lambda^* = 1.03$ $C_4 = 46.4$ $C_5 = 508.1\ MPa$
		Ligament	$\rho = 1\frac{g}{cm^3}$ $K = 0.8\ GPa$ $C_1 = 1.44\ MPa$ $C_2 = 0.0$ $C_3 = 570\ kPa$ $\lambda^* = 1.06$ $C_4 = 48.0$ $C_5 = 467.1\ MPa$

‘

APPENDIX B: SUMMARY OF MATERIAL SENSITIVITY SUMMARY FOR INJURIOUS CAVEMAN LOWER EXTREMITY IMPACTS

. *Table 14: The sensitivity study results from the CAVEMAN lower extremity impacts in the Bailey test series.*

Medium Impact Sensitivity Study Summary			
Impact	**Variation Description**	**Change in Force Response**	**Change in Fracture**
Medium	Muscle Stiffness x 0.1	N	N
	Muscle Stiffness x 10	N	N
	Tendon Stiffness x 0.1	N	Y (no fracture)
	Tendon Stiffness x 10	N	N
	Heel Pad Stiffness x 0.1	N	N
	Heel Pad Stiffness x 10	N	N
	Ligament Stiffness x 0.1	Y	Y (no fracture)
	Ligament Stiffness x 10	Y	Y (severe fracture)
	Cancellous Bone Stiffness x 0.1	N	N
	Cancellous Bone Stiffness x 10	N	N
	Cortical Bone Stiffness - 25%	N	Y (no fracture)
	Cortical Bone Stiffness + 25%	N	N
Medium	"High" Allignment (4 Deg Dif.)	N	N
Medium	Cortical Thickness Element Inc.	N	Y (no fracture)
	Cortical Thickness Element Dec.	Y	Y (severe fracture)
	Cortical Thickness 3mm Inc.	N	Y (no fracture)
	Cortical Thickness 3mm Dec.	N	N

High Impact Sensitivity Study Summary			
Impact	**Variation Description**	**Change in Force Response**	**Change in Fracture**
High	Muscle Stiffness x 0.1	N	N
	Muscle Stiffness x 10	N	N
	Tendon Stiffness x 0.1	Y	N
	Tendon Stiffness x 10	N	N
	Heel Pad Stiffness x 0.1	N	N
	Heel Pad Stiffness x 10	N	N
	Ligament Stiffness x 0.1	Y	Y (no fracture)
	Ligament Stiffness x 10	Y	N
	Cancellous Bone Stiffness x 0.1	Y	N
	Cancellous Bone Stiffness x 10	N	N
	Cortical Bone Stiffness - 25%	Y	Y (minor fracture)
	Cortical Bone Stiffness + 25%	N	N
High	"Medium" Allignment (4 Deg Dif.)	N	N
High	Cortical Thickness Element Inc.	Y	Y (no fracture)
	Cortical Thickness Element Dec.	Y	N
	Cortical Thickness 3mm Inc.	N	N
	Cortical Thickness 3mm Dec.	N	N

APPENDIX C: COXAL BONE CORTICAL THICKNESS – FE

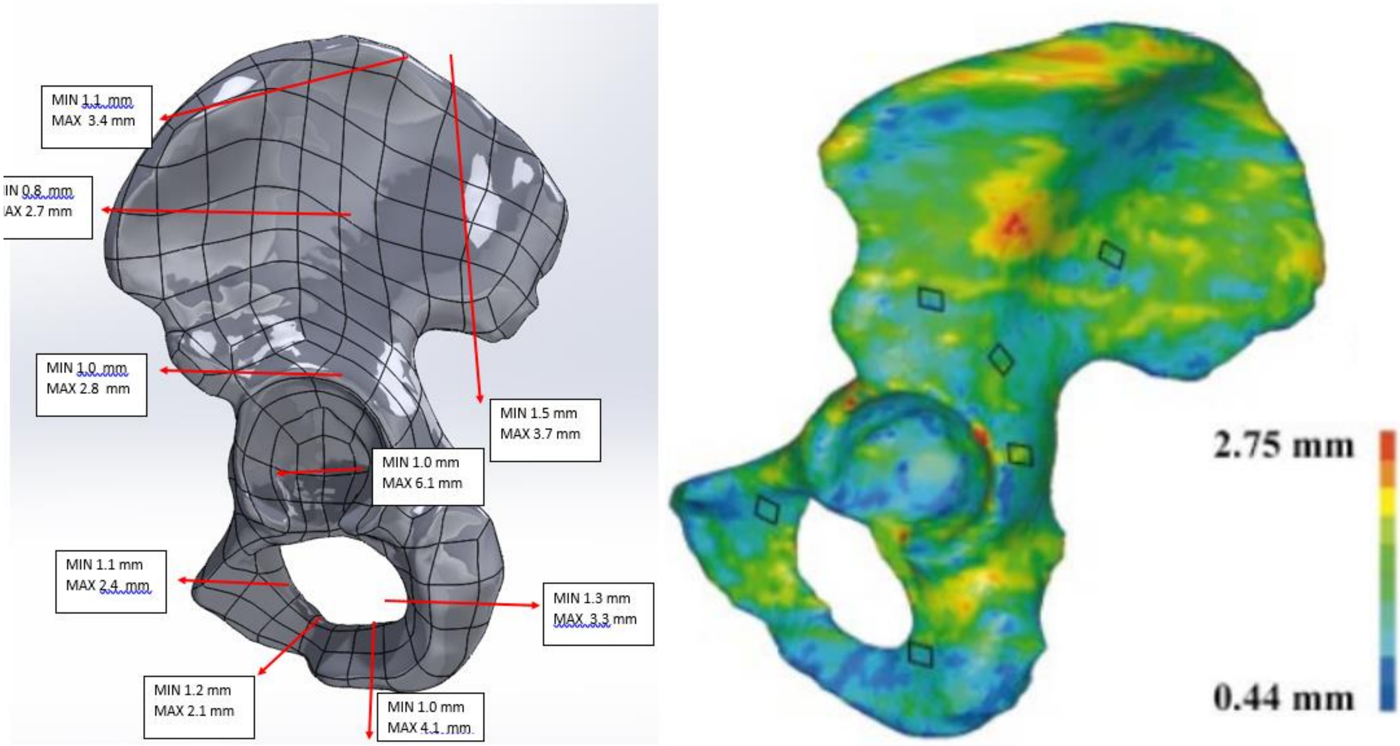

Figure 59. Cortical thicknesses of the CAVEMAN FE model compared to Anderson et al. 2005 measurements

APPENDIX D: SIJ ANTERIOR AND POSTERIOR MEASUREMENTS - FE

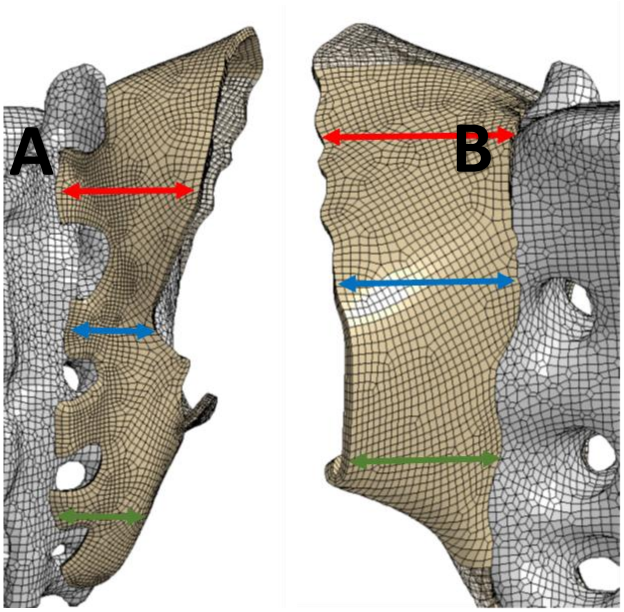

Posterior SIJ Ligament - Geometric Measurement Comparison			
Region	**Steinke - Measurements (mm)**	**SD**	**CAVEMAN - Measurements (mm)**
[-1]	**Length**		**Length**
	19.5	3.8	37.2
	Width		**Width**
	2.5	1	1.5
[0]	**Length**		**Length**
	19.3	4.4	20.1
	Width		**Width**
	3.1	1.3	1.5
[1]	**Length**		**Length**
	20.5	5	30.2
	Width		**Width**
	3.1	1	1.5
Region	**Steinke - Measurements (mm)**	**SD**	**CAVEMAN - Measurements (mm)**
[-1]	**Length**		**Length**
	18.6	4.4	37.8
	Width		**Width**
	2.4	0.6	1.5
[0]	**Length**		**Length**
	16.6	4.2	35.4
	Width		**Width**
	2.4	0.6	1.5
[1]	**Length**		**Length**
	14.8	4.4	32.2
	Width		**Width**
	2.5	0.6	1.5

Figure 60. Posterior (A. lengths) and anterior (B. lengths) views of the CAVEMAN sacroiliac joint ligament structure with a geometric measurement comparison to the anatomical data reported in Steinke, 2011.

APPENDIX E: COMPLETE INJURY DESCRIPTIONS FROM SALZAR ET AL. 2011

Table 15. Complete post-test injury results from the Salzar test series. Tests 1.5-1.10 are acetabulum impacts while tests 1.11-1.16 are iliac wing impacts.

Test ID	Anterior injuries (AIS 98)	Posterior injuries (AIS 98)
1.5-a	Non-displaced Fx of the right ilio PR, 2 non-displaced FXs (superior and inferior) of the right ischio PR (8.5.26.00.**2**)	Fx descending from the top of S1, along the sacral holes (postage-stamp Fx) (8.5.26.00.**2**)
1.6-a	Displaced Fx of right ilio PR, right ischio PR; Fx of the left ilio PR down to the pubic angle. (8.5.26.04.**3**)	Non-displaced Fx through the right sacral holes, from the right 2/3 of the top of S1, descending through the holes 1 to 4; postage-stamp Fx. (8.5.26.00.**2**)
1.7-a	Vertical displaced Fx of both right ilio and ischio rami, parallel to the PS, multiple fragments. (8.5.26.04.**3**)	Non-displaced Fx through right sacrum ala, superior part. (8.5.26.00.**2**)
1.8-a	Complex displaced Fx of the acetabulum, along the fusion line of the 3 bones (ilium-ischium-pubis), extended postily toward the greater sciatic notch, and antily through the right ilio PR. Double Fx of the right ischio PR (T-Fx of Letournel). (8.5.26.04.**3**)	No injury
1.9-a	Complex vertical Fx of both ilio and ischio rami Fx, down along the PS, then going along the axis of the ischio PR, with multiple fragments. (8.5.26.04.**3**)	Vertical Fx of the body of the sacrum, along the centreline (potting), from the top of S1 to the third right sacral post hole (8.5.26.00.**2**)
1.10-a	Non-displaced Fx of the right ilio PR, 2 non-displaced FXs (superior and inferior) of the right ischio PR. (8.5.26.00.**2**)	Non-displaced Fx of the body of the sacrum, along to the post centreline, close to the potting incomplete post Fx of the sacrum, right side, parallel to the SIJ, including the right articular process. (8.5.26.00.**2**; 8.5.26.00.**2**)
1.11-i	Partial disruption of the PS, mostly the ¾ inferior part. (8.5.30.00.**3**)	Partial dislocation of the post-inferior part of the right SIJ; no Fx there. (8.5.28.00.**3**)
1.12-i	Slight laxity	Slight laxity of right SIJ
1.13-i	No Fx; minor disruption/tear	Fx at the post-inferior side of the right SIJ (through an osseous bridge). (8.5.26.00.**2**)
1.14-i	Laxity w/o Fx	Minor post dislocation of the right SIJ (8.5.28.00.**3**)
1.15-i	No injury	Non-displaced complete Fx of the right side of the sacrum, parallel to the SIJ. (8.5.26.00.**2**)
1.16-i	Disruption of the PS, ¾ inferior of the surface of the cartilage is detached from the right iliac bone. (8.5.30.00.**3**)	Partial dislocation of the right SIJ, post side, close to the sup and inf post iliac spines. Post osseous bridge of the right SIJ.(8.5.28.00.**3**)

APPENDIX F: CAVEMAN ILIAC WING RESPONSE COMPARED TO TWO NON-INJURY EXPERIMENTAL CASES

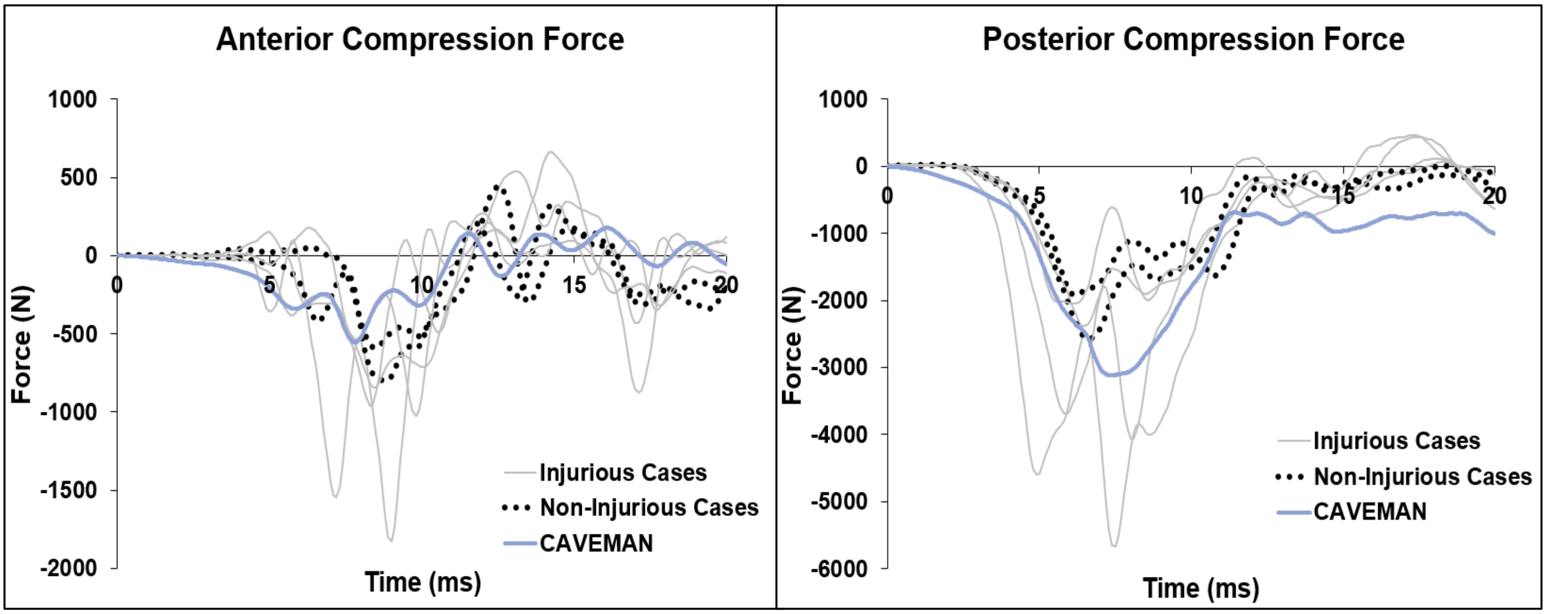

Figure 61. Comparison of the FE iliac wing impact response to both the injurious and non-injurious force-time history responses. These force response curves provide a level of reinforcement to the conclusion made in the prior injury predictive metric evaluation portion of this thesis that peak posterior force is reliable. The 2 cases where no injury occurred in the Salzar data set experienced comparatively lower peak sacral force.

APPENDIX G: REVIEW OF METHODS FOR CROSS CORRELATION SCORING

This portion of the appendix will review the methods used for the CORA cross correlation scoring analysis. Equations and mathematical methods explained in this appendix are directly from MATLAB code from the UVA Center for Applied Biomechanics (CAB) as well as the CORA manual (CORAplus Release 4.0.4 User's Manual, Thunert 2017). These will be reviewed to bring greater clarity to how the CORA scores for the validity of the FE pelvis force-time history response was evaluated.

The first mathematical step in the cross correlation method is determining the maximum cross correlation defined as "K". To achieve this, the reference curve is shifted by multiples of Δt and a cross correlation value "K_{xy}" that varies between -1 and 1 is defined for each altered time shift (Equation A.G.1). The time shifts correspond to the user defined range of evaluation. Before doing so, t_{min} and t_{max} outline the range of time to be evaluated and are defined by the user. In order to avoid artificially inflated or deflating the CORA score, it is wise to choose a time evaluation range that includes regions of interest in the time history, so for this analysis the range of time history to be evaluated was between 2ms and 14ms.

$$K_{xy}(m)=\frac{\sum_{i=0}^{n-1} x(t_{min}+(m+i)\cdot\Delta t)\cdot y(t_{min}+i\cdot\Delta t)}{\sqrt{\left(\sum_{i=0}^{n-1} x^2(t_{min}+(m+i)\cdot\Delta t)\cdot\sum_{i=0}^{n-1} y^2(t_{min}+i\cdot\Delta t)\right)}} \quad \text{with} \quad -1\leq K_{xy}\leq 1$$

Equation A.G.1

A value of K is determined for each time shift. Figure 62 displays a plot of K calculated for each time shift for an example force-time history comparison. The time shift with the maximum K value is then used for the 3 components of the cross correlation rating: progression, phase, and shape.

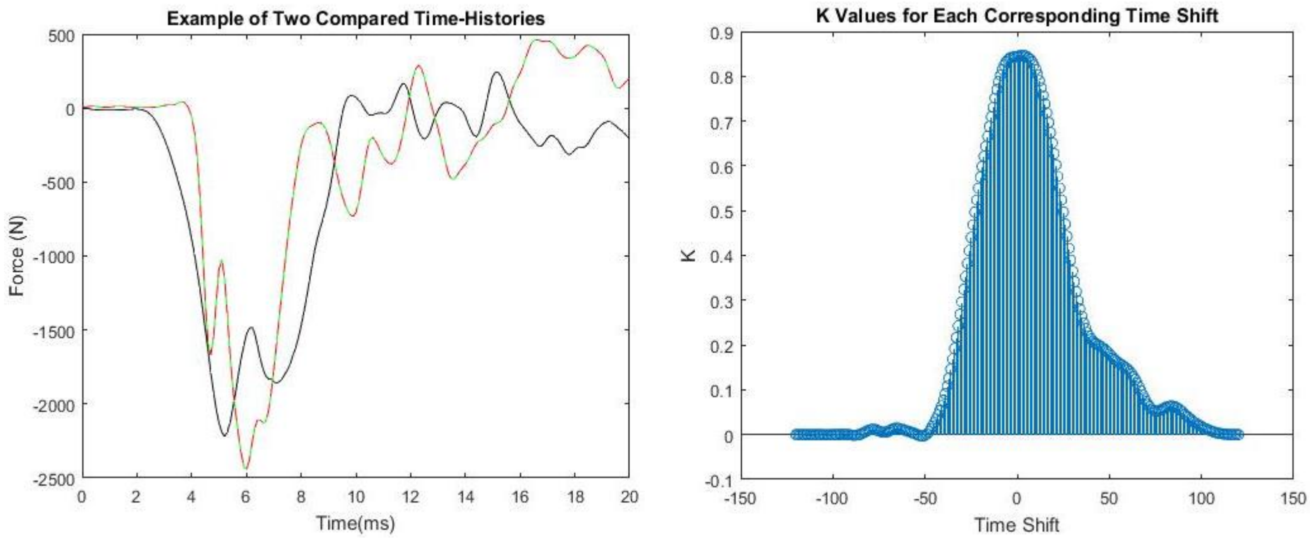

Figure 62. Plot of two force-time histories (left) and the corresponding K value to each time shift. Evaluation range defined between 2 and 14 ms. The maximum K value is used for further calculations.

CORA's "progression" rating (V) is most analogous to what would be described as loading rate in the field of biomechanics. The progression rating is calculated directly from K. The K_v specifies the rate of decline of the progression rating as it deviates from the reference curve. K_v was specified to be 10 for this analysis, since this was suggested in the CORA handbook as well as the default setting in the UVA CAB script.

$$V = \left(\frac{1}{2} (K+1) \right)^{k_v}$$

Equation A.G.2

The timing or phase shift rating (P) is initially dictated by D_{min} and D_{max} which are parameters defined by the user. The values of D_{min} and D_{max} used for all of these analyses were 0.01 and 0.12, respectively. These selected D parameters and prior defined time range of evaluation are used to calculate the signal time values (Equation A.G.3).

$$\delta_{min} = D_{MIN} \cdot (t_{max} - t_{min}) \text{ with } 0 < D_{MIN} \leq 1$$

Equation A.G.3

$$\delta_{max} = D_{MAX} \cdot (t_{max} - t_{min}) \text{ with } 0 < D_{MAX} \leq 1$$

After determining δ_{min} and δ_{max} the phase shift rating is determined by equation A.G.4. The K_p parameter determines the rate of decline between 1 and 0 when scoring. For this analysis this was set to be linear, 1. A maximum score is of one and minimum score of 0.

$$P = \begin{cases} 1 & \text{if} \quad |\delta| < \delta_{min} \\ \left(\dfrac{|\delta_{max} - |\delta||}{\delta_{max} - \delta_{min}} \right)^{k_P} & \text{with} \quad k_G \in N_{>0} \\ 0 & \text{if} \quad |\delta| > \delta_{max} \end{cases}$$

Equation A.G.4

The size or magnitude rating (G) is assigned by determining and comparing the two square of the areas that lie between the time axis and curve boundaries. Since the curves have equally spaced supporting points the ratios in equation A.G.5 are calculated and then used to determine the size rating in equation A.G.6.

$$F_x[t_{min}, t_{max}] \qquad F_y[t_{min}+\delta, t_{max}+\delta] \qquad \frac{F_x}{F_y} = \frac{\sum_{i=1}^{n} x^2(t_{min}+\delta+i\cdot\Delta t)}{\sum_{i=1}^{n} y^2(t_{min}+i\cdot\Delta t)}$$

Equation A.G.5

$$G = \begin{cases} \left(\dfrac{F_x}{F_y} \right)^{k_G} & \text{if} \quad F_y > F_x \\ & \text{with} \quad k_G \in N_{>0} \\ \left(\dfrac{F_y}{F_x} \right)^{k_G} & \end{cases}$$

Equation A.G.6

The K_G parameter determines the rate of decline similar to the other two methods, and it was set to be 1, the same as the phase shit rate of decline metric.

The three scored methods (V, G, and P) representing progression, phase, and magnitude ratings are then combined to determine an overall cross correlation score. The metrics g_{V}, g_{P}, and g_{G} are weighting factors assigned to each correspondingly scored method. The sum of these weighting factors must be equal to 1, in order to enforce C_2 (the cross correlation score) to be between the values of 0 and 1 (where 1 is a perfect fit).

$$C_2 = g_V \cdot V + g_P \cdot P + g_G \cdot G$$ **Equation A.G.7**

APPENDIX H: EXTENDED CORA CROSS-CORRELATION SCORING RESULTS

Table 16. CORA cross-correlation scores for each of the individual components of the total rating: phase, size and shape. Average FE scores were within 1 SD of average experimental score and all p-values were greater than 0.05 except one data trace in the shape consideration.

PHASE SCORING					PHASE SCORING				
Average CORA Scores Anterior Acet Impact				**p-Value**	**Average CORA Scores Posterior Acet Impact**				**p-Value**
avg exp	0.526	**sd**	0.300	0.15	**avg exp**	0.497	**sd**	0.342	0.84
avg FE	0.745	**sd**	0.253		**avg FE**	0.538	**sd**	0.391	
PHASE SCORING					**PHASE SCORING**				
Average CORA Scores Anterior Iliac Impact				**p-Value**	**Average CORA Scores Posterior Iliac Impact**				**p-Value**
avg exp	0.537	**sd**	0.371	0.15	**avg exp**	0.644	**sd**	0.265	0.80
avg FE	0.784	**sd**	0.277		**avg FE**	0.384	**sd**	0.250	
SIZE SCORING					**SIZE SCORING**				
Average CORA Scores Anterior Acet Impact				**p-Value**	**Average CORA Scores Posterior Acet Impact**				**p-Value**
avg exp	0.556	**sd**	0.284	0.42	**avg exp**	0.662	**sd**	0.154	0.25
avg FE	0.460	**sd**	0.194		**avg FE**	0.766	**sd**	0.161	
SIZE SCORING					**SIZE SCORING**				
Average CORA Scores Anterior Iliac Impact				**p-Value**	**Average CORA Scores Posterior Iliac Impact**				**p-Value**
avg exp	0.555	**sd**	0.247	0.60	**avg exp**	0.512	**sd**	0.280	0.96
avg FE	0.490	**sd**	0.227		**avg FE**	0.506	**sd**	0.162	
SHAPE SCORING					**SHAPE SCORING**				
Average CORA Scores Anterior Acet Impact				**p-Value**	**Average CORA Scores Posterior Acet Impact**				**p-Value**
avg exp	0.537	**sd**	0.131	0.11	**avg exp**	0.549	**sd**	0.152	0.03
avg FE	0.424	**sd**	0.122		**avg FE**	0.417	**sd**	0.082	
SHAPE SCORING					**SHAPE SCORING**				
Average CORA Scores Anterior Iliac Impact				**p-Value**	**Average CORA Scores Posterior Iliac Impact**				**p-Value**
avg exp	0.409	**sd**	0.140	0.59	**avg exp**	0.828	**sd**	0.066	0.25
avg FE	0.467	**sd**	0.217		**avg FE**	0.781	**sd**	0.076	